TECHNISCHE UNIVERSITÄT MÜNCHEN

Fakultät für Elektrotechnik und Informationstechnik

Lehrstuhl für Biologische Bildgebung

Sparsity-based reconstruction methods for optoacoustic tomography

Yiyong Han

Vollständiger Abdruck der von der Fakultät für Elektrotechnik und Informationstechnik der Technischen Universität München zur Erlangung des akademischen Grades eines

Doktors der Naturwissenschaften (Dr. rer. nat.)

genehmigten Dissertation.

Vorsitzende(r): Univ.-Prof. Dr. Gerhard Rigoll

Prüfer der Dissertation:

1. Univ.-Prof. Dr. Vasilis Ntziachristos
2. Univ.-Prof. Dr. Bjoern Menze
3. Univ.-Prof. Dr. Klaus Diepold

Die Dissertation wurde am 31.05.2017 bei der Technischen Universität München eingereicht und durch die Fakultät für Elektrotechnik und Informationstechnik am 03.07.2018 angenommen.

In memory of my beloved mother

Abstract

Optoacoustic tomography can generate high-resolution optical images of biological samples in vivo at depths of several millimeters to centimeters. The technique is based on illuminating the sample with nanosecond laser pulses, detecting the resulting acoustic signals and converting these signals into an image using reconstruction algorithms. A good reconstruction algorithm can allow accurate visualization of complex anatomical features, and also facilitate further multispectral analysis. This dissertation describes various model-based reconstruction algorithms for optoacoustic tomography.

Model-based reconstruction is generally more accurate than reconstruction based on analytical inversion, but it requires more computational and memory resources. Here, a much faster optoacoustic reconstruction method is proposed, in which the model matrix and the optoacoustic signal are transformed into the wavelet domain. Pseudoinverse of model matrices can be calculated on a much smaller scale, and then multiplied with the corresponding signals to form the final optoacoustic image. Using this methodology over an order of magnitude reduction in inversion time is demonstrated for simulated and experimental data.

Second, sparsity-based reconstruction is developed for a two-dimensional optoacoustic imaging system. Specifically, a cost function is used that includes the L1 norm of the image in sparse representation along with a total variation term. The minimization process is implemented using gradient descent with backtracking line search. This algorithm was evaluated with simulated and experimental datasets, and found that proposed scheme leads to sharper reconstructed images with weaker streak artifacts than both conventional L2-norm regularized reconstruction and back-projection reconstruction.

Next, the sparsity-based reconstruction is adapted to three-dimensional geometries, thereby exploiting more of the potential of tomography because the ultrasound waves generated after

sample illumination propagate in all directions. To accelerate the reconstruction, Barzilai-Borwein line search is used to analytically determine the step size during gradient descent optimization. The proposed method offers 4-fold faster reconstruction than the previously reported L1-norm regularized reconstruction based on gradient descent with backtracking line search. The new algorithm also provides higher-quality images with fewer artifacts than L2-norm regularized reconstruction or back-projection reconstruction.

Finally, this dissertation develops frequency domain methods for reconstructing optoacoustic images when the sample is illuminated with an amplitude-modulated continuous-wave laser. Formulas are found to guide the minimum demand of the projections and frequencies. The numerical method can be used to guide the design of experimental set-ups for optoacoustic tomography in the frequency domain, as well as the selection of measurement parameters.

The methods developed in this dissertation enable robust processing and inversion during optoacoustic reconstructions, which may enhance the performance of optoacoustic imaging and tomography in preclinical and clinical environments, as well as open up avenues for further theoretical and experimental developments.

Acknowledgments

This dissertation would not have been possible without the guidance and support of several individuals who accompanied me during the last years and in one way or another contributed their valuable assistance in the preparation and completion of this research.

First and foremost I would like to thank my advisor Professor Vasilis Ntziachristos who accepted me as his PhD student and always gave me enough freedom and encouragement to carry out new approaches. In particular, I'd like to thank him for many helpful discussions about research, for continually encouraging me to improve my work, and for giving me the opportunities to share my work with the scientific community.

I would like to express my deepest appreciation to my previous group leader Dr. Amir Rosenthal. It was his persistence in the optoacoustic imaging work that influenced me as a researcher. The discussions with him deepened my understanding and motivated me to find new solutions. Working with him opened up new perspectives and insights on optoacoustic reconstruction algorithms for me. I am also indebted to my current group leader, Dr. Jaya Prakash. He has provided wise advice and encouragement through the second half of these years, and discussing with him has been both enlightening and stimulating. His knowledge and intuition on the subjects related to the present work have very positively influenced its outcome. I really appreciate his scientific and personal advice for me.

I wish to thank all the people at the IBMI who contributed in valuable discussions, technical support, theoretical feedback and scientific advice for this dissertation. I would like to thank prof Daniel Razansky for his advice on optoacoustic imaging, Dr. Xose Luis Dean Ben for his continuous help in optoacoustic theory and reconstruction, Lu Ding for her collaboration on the 3D reconstruction project and for sharing her GPU reconstruction code, Dr. Daniel Queiros for discussions on wavelet packet reconstruction, Dr. Stratis Tzoumas for his expertise in MSOT

animal experiments and later saturation analysis, Ludwig Prade for helpful discussions on frequency domain optoacoustic tomography, Dr. Antonio Nunes for his participation in MSOT imaging, Dr. Juan Salichs for his suggestion to perform optoacoustic imaging with a single-element transducer, Dr. Miguel Angel Araque Caballero for sharing his impulse response correction algorithm, Ali Özbek for sharing his 3D back projection GPU code, Dr. Juan Aguirre for discussions on model-based reconstruction with raster scanning geometry, and Dr. Andreas B ühler for discussions on general optoacoustic imaging questions.

I would like to acknowledge Dr. Korbinian Paul-Yuan, Ivan Olefir, Yuan Gao, Dr. Andre Stiel, Dr. Evangelos Liapis, Hong Yang, Marwan Muhammad, Dr Gael Diot, Qutaiba Mustafa and the rest of the biology group for their suggestions and feedback to help create and refine the MSOT analysis GUI. I am grateful to Dr. Jiao Li, Dr. Andrei Chekkoury, Paul Vetschera, Benno Koberstein-Schwarz, Dr. Ara Ghazaryan and Amy Lin for their assistance when I initially started with multispectral optoacoustic mesoscopy imaging. Furthermore, I would like to thank Dr. Tobias Wiedemann for his inputs on adrenal and pituitary tumor optoacoustic imaging, Dr. Christoph Hinzen, Dr. Josefine Reber, Dr. Annette Feuchtinger, Maximilian Koch and Ben McLarney for their inputs on ex-vivo rat heart imaging project with Boehringer Ingelheim.

Further thanks and acknowledgements go to Georg Wissmeyer and Roman Shnaiderman for being my roommates over three years and sharing a lot of joyous time inside and out of the office, to Panagiotis Symvoulidis for being my roommate when I first joined IBMI, to Dr. Chapin Rodriguez for his help on editing and improving my writing work, and to all of them for giving me useful advice. Dr. Andriy Chmyrov, Dr. Zhenyue Chen, Dr. Xiaopeng Ma, Dr. Yuanyuan Jiang, Hailong He, Yuanhui Huang, Subhamoy Mandal, Dmitry Bozhko, Andrei Berezhnoi, Bingwen Wang, Jingye Zhang and the rest of IBMI colleges, with whom I shared a discussion, a chat, a lunch, a beer or a bus ride, have to be thanked for their easy-going, hospitable nature. All of them influenced me in one way or another and enriched me as a person.

My special thanks go to Susanne Stern, Dr. Andreas Brandstaetter, Martina Riedl, Zsuzsanna Oszi, Silvia Weinzierl, Prof. Dr. Karl-Hans Englmeier, Dr. Roland Boha, Dr. Julia Thomas, Dr. Barbara Schroeder, Dr. Doris Bengel and Ines Baumgartner in various aspects of administration and organization. As well I would like to thank Sarah Glasl, Uwe Klemm and Florian Jurgeleit who assisted me in optoacoustic experiments whenever mice were involved.

I would also like to thank the Chinese Scholarship Council (CSC) to fund my work in the dissertation.

Finally, I would like to express my deep thanks to my parents, my wife, my daughter and my friends who have encouraged and supported me throughout all my academic years. Thank you all for your never-ending patience, support and love.

Acknowledgments

Contents

List of Figures

List of Tables

List of Tables

List of abbreviations

CW	Continuous-wave
OAT	Optoacoustic tomography
2D	Two-dimensional
3D	Three-dimensional
TSVD	Transacted singular value decomposition
MSOT	Multispectral optoacoustic tomography
ROI	Region of interest
SIR	Spatial impulse response
LSQR	Least squares QR
SVD	Singular value decomposition
BP	Back-projection
IMMI	Interpolated-model-matrix-inversion
WP	Wavelet-packet
WP-IMMI	Wavelet-packet domain based interpolated-model-matrix-inversion
FAD	Finite-aperture detectors
IMMI-FAD	Interpolated-model-matrix-inversion with finite-aperture detectors
GWP-IMMI-FAD	Generalized wavelet-packet based interpolated-model-matrix-inversion
RAM	Random access memory
STD	Standard deviation

RMSD	Root-mean-square-deviation
SSIM	Structural similarity
TV	Total variation
TV-L1	Total variation and L1 norm based inversion
Tik-Lap	Tikhonov regularization with a Laplacian penalty
OPO	Optical parametric oscillator
SNR	Signal-to-noise ratio
CNR	Contrast-to-noise ratio
L1-GDBB	Sparsity-based inversion using gradient descent & Barzilai-Borwein line search
L1-GDBT	Sparsity-based inversion using gradient descent & backtracking line search
L2-LSQR	LSQR algorithm with L2-norm regularization
UTA	Ultrasound transducer array
GPU	Graphics processing unit
FD-OAT	Frequency domain optoacoustic tomography
TD-OAT	Time domain optoacoustic tomography
ES	Even sampling
Tik	Tikhonov

1 Introduction

1.1 Optoacoustic imaging

Optoacoustic imaging, also termed photoacoustic imaging, is a noninvasive imaging technique that holds great promise for clinical or preclinical applications [1]–[5]. Optoacoustic imaging is a hybrid imaging modality that is capable of visualizing optical contrast at imaging depths and resolutions often found in medical ultrasonography [6]. Optoacoustic imaging can be regarded as an ultrasound modality that exploits optical-absorption image contrast, which can give deeper information than pure optical imaging [1]. With this advantage, numerous fundamental studies of optoacoustic imaging on theory, instruments and applications have been investigated in recent years [1]–[5].

A typical optoacoustic imaging system employs a laser to illuminate the object, and the acoustic signals generated by the optoacoustic effect then propagate from the inside of the object and can be measured by ultrasonic transducers outside of the object [7]–[9]. The optoacoustic image of the object corresponds to the optical energy deposition (light absorption) in the object [10].

Optoacoustic imaging can also be classified into two categories: optoacoustic microscopy/mesoscopy [11], [12] and optoacoustic tomography [13], [14]. Optoacoustic microscopy usually employs mechanical raster scanning of a high-frequency focused transducer (in the case of acoustic resolution optoacoustic microscopy) or a focused laser beam (in the case of optical resolution optoacoustic microscopy) in order to acquire the acoustic signals. In these cases, the optoacoustic image is obtained from the set of A-lines and requires no reconstruction algorithms. Optoacoustic mesoscopic imaging also is performed in similar lines, just that the ultrasound will be operating at frequency range of tens of MHz. Optoacoustic tomography, in contrast, generally illuminates the object over a broad range, and the acoustic signals are

acquired by mechanically scanning with a low-frequency transducer or an array of detectors. Then this acoustic data is provided to a reconstruction algorithm to generate the optoacoustic image. There are three commonly used detection geometries in optoacoustic tomography: spherical, cylindrical and planar. The cylindrical and spherical detection geometries require collecting all the measurements around the target, while the planar detection geometry allows more flexibility about where measurements can be acquired.

Optoacoustic imaging can be presented using the time domain methodology [15] or frequency domain methodology [16], [17] depending on the laser employed. The classic time domain optoacoustic imaging methodology employs a short-pulse (nanosecond range), high peak-power laser for illumination, while frequency domain optoacoustic imaging uses a periodic, intensity-modulated, continuous-wave (CW) laser.

1.2 Reconstructions in optoacoustic imaging

Most optoacoustic tomography reconstruction algorithms are based only on the acoustic wave equation, modeling the propagation of optoacoustically generated acoustic waves [10], [18]. The "forward problem" in optoacoustic tomography refers to the process in which light energy deposited at optical absorbers is converted to ultrasonic pressure waves. Image reconstruction in optoacoustic tomography can then be considered the "inverse" of the forward problem: calculating the optoacoustic images from the recorded pressure signals [19]–[25].

For an optoacoustic tomography system with specific transducer and detection trajectory, image reconstruction can be performed either analytically or numerically. Various analytic optoacoustic tomography reconstruction algorithms such as back-projection methods and time reversal methods have been developed for optoacoustic tomography under the assumption of point-like ultrasound transducers [19]–[21], [23]. This may lead to reconstruction inaccuracies and artifacts, e.g. in systems with large-area acoustic detectors [26]–[29]. In addition, analytic optoacoustic tomography reconstruction algorithms have a closed-form solution and are numerically stable only when the measurement aperture encloses the entire object, which is not feasible in many clinical or pre-clinical optoacoustic tomography applications with limited-view geometries [30], [31]. Numerical model-based optoacoustic tomography reconstruction algorithms represent a

potent alternative to the analytic approaches because they can more generally account for system- and geometry-related parameters [20], [24], [26] , [29]–[35]. Optoacoustic tomography reconstructions based on models in the time domain [24], [27], [32]–[35] or frequency domain [36], [37] can model any additional physical effects, such as acoustic heterogeneities and attenuation, light propagation or geometric detector properties. Despite the accurate performance achieved by model-based reconstructions algorithms, one of the main disadvantages is their computational complexity and need for computer memory, especially in the case of finite-size detectors or with more pixels [26]. Normally a more complex model leads to a more accurate reconstruction, but a large optoacoustic tomography model matrix will lead to excessive reconstruction times.

1.3 Goals and objectives

The goals of this dissertation are to develop and implement various fast and accurate model-based reconstruction methods for different optoacoustic tomography (OAT) systems: a 2D OAT system with a finite-size single element transducer; a 2D OAT system with cylindrically focused curved arrays; and a 3D OAT system with spherically focused, curved arrays. Accurate image reconstruction improves not only the visualization of anatomical results, but it also facilitates subsequent multispectral analysis for oxygen saturation, molecular targeting, and other applications. A key consideration in developing these reconstruction methods is the way to build the optoacoustic forward model matrix, and the manner to achieve fast and accurate results with acoustic inversion. This dissertation also examines the relationship among spatial resolution, frequency and projection number in order to guide the set-up of a frequency domain OAT; this approach can also be applied to time domain OAT.

1.4 Outline of the Thesis

The dissertation is structured as follows. Chapter 2 provides the reader with theoretical background on optoacoustic imaging in the time and frequency domains; key concepts include optoacoustic signal generation, the optoacoustic wave equation, the forward solution of the optoacoustic wave equation and the forward matrix. Common inversion methods such as transacted singular value decomposition and Tikhonov regularization are also introduced. In

chapter 3, a framework of model-based reconstruction in the wavelet packet domain is demonstrated for a 2D OAT system with a single-element, finite-size detector. The wavelet packet reconstruction method is evaluated with simulations and experiments and provides a significant reduction in reconstruction time compared to a least-squares-based inversion method. Chapter 4 introduces a sparsity-based acoustic inversion for cross-sectional optoacoustic imaging on a multispectral optoacoustic tomography (MSOT) system with an ultrasound detector array. The proposed sparsity-based reconstruction method shows good performance in both the full- and limited-view geometries. Chapter 5 further develops the sparsity-based reconstruction for adaptation to a 3D OAT system. Chapter 6 shows how the frequency affects reconstructions in the time and frequency domains, which can help for measurements selection without compromising the image quality. The thesis ends with chapter 7, in which the results of the entire thesis are summarized and synthesized, leading into an outlook on open questions and next research steps in the field of optoacoustic image reconstruction.

2 Theoretical Background

This chapter first presents a short introduction to the fundamental principles of optoacoustic imaging. Furthermore, key concepts about optoacoustic signal generation, the forward solution and modeling the optoacoustic effect are given in the time domain (section 2.2) and frequency domain (section 2.3). The concepts in this chapter provide a theoretical background for understanding the technical details, simulations, experiments and discussions in subsequent chapters.

2.1 Optoacoustic principles

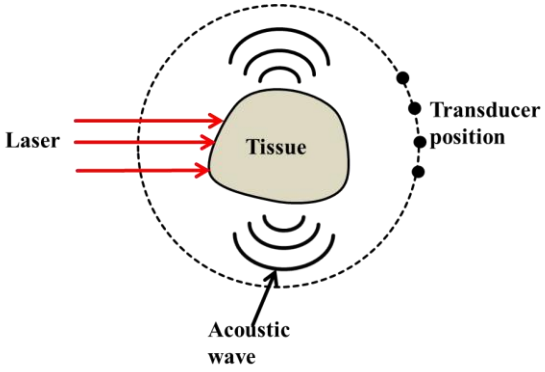

Figure 2.1 A sketch of an optoacoustic imaging geometry.

A schematic of an optoacoustic imaging setup is shown in Figure 2.1. The object to be imaged is irradiated with a laser at visible to near-infrared wavelengths (650-1000 nm is the near-infrared window for biological tissue), and the thermoacoustic effect results in transient localized heating followed by a pressure wavefield. The pressure wavefield propagates out of the object and is measured by ultrasonic transducers located at different positions outside the object. Afterwards,

image reconstruction algorithms can recover the initial distribution of optical energy deposited within the object, which is dependent on the illumination and the optical properties of the object. Two types of laser illumination can be used to generate optoacoustic signals: short (nanosecond) optical pulses with high peak power, or modulated CW lasers with relatively low mean power and high modulation frequency. These two categories will be described in detail in the next two sections.

2.2 Time domain optoacoustic imaging

2.2.1 Optoacoustic signal generation and wave equation in time domain

In order to achieve good spatial resolution for time domain optoacoustic imaging, two confinements should be fulfilled [3], [5]. One confinement is thermal confinement, which means the laser pulse width τ_p needs to be much shorter than thermal confinement τ_{th} in order to avoid thermal diffusion:

$$\tau_p < \tau_{th} = \frac{d_c^2}{4D_T} \ , \tag{2.1}$$

where d_c is the characteristic dimension (targeted spatial resolution) and D_T is the thermal diffusivity (a typical value for most soft tissues is $\approx 1.4\times10^{-5} mm^2/s$) [39]. With a 10-nanosecond pulse laser, the best spatial resolution guided by thermal confinement is ~0.06 μm, which is much less than the spatial resolution of optoacoustic imaging. Another confinement is acoustic stress confinement, which means that optoacoustic propagation of the absorber during laser illumination is negligible:

$$\tau_p < \tau_s = \frac{d_c}{c} \ , \tag{2.2}$$

where c is the speed of sound. With a 10-nanosecond pulse laser and c of 1500 m/s (typical for biological tissue) [40], the best spatial resolution guided by acoustic stress confinement is ~15 μm.

Under these two confinements, the initially induced in optoacoustic wave pressure $p_0(\mathbf{r})$ within the tissue is [5]

$$p_0(\mathbf{r}) = \left(\beta c^2 / C_p\right) \mu_a(\mathbf{r}) \Phi(\mathbf{r}) = \Gamma H(\mathbf{r}) \tag{2.3}$$

where β is the thermal expansion coefficient (K^{-1}), C_p is the heat capacity ($J/(\mathrm{kg}\bullet\mathrm{K})$), $\mathbf{r}$ is the position, $\mu_a(\mathbf{r})$ is the optical absorption coefficient (cm^{-1}), $\Phi(\mathbf{r})$ is the optical fluence (J/cm^2), Γ is the Grueneisen parameter, which equals $\beta c^2 / C_p$ and represents the amount of temperature converted to optoacoustic pressure and $H(\mathbf{r})$ is the absorbed optical energy, which equals $\mu_a(\mathbf{r})\Phi(\mathbf{r})$.

Optoacoustic wave generation and propagation in an acoustically homogeneous medium is described by the following optoacoustic equation [41]

$$\frac{\partial^2 p(\mathbf{r},t)}{\partial t^2} - c^2 \nabla^2 p(\mathbf{r},t) = \Gamma \frac{\partial H(\mathbf{r},t)}{\partial t} \tag{2.4}$$

where t is time, $\mathbf{r}$ is the position in 3D space, $p(\mathbf{r},t)$ is the generated pressure, Γ is the Grueneisen parameter, and $H(\mathbf{r},t)$ is the amount of energy absorbed in the tissue per unit volume and per unit time. If $H(\mathbf{r},t)$ can be separated into spatial and temporal components, then Eq. (2.4) can be simplified as:

$$\frac{\partial^2 p(\mathbf{r},t)}{\partial t^2} - c^2 \nabla^2 p(\mathbf{r},t) = \Gamma H_r(\mathbf{r}) \frac{\partial H_t(t)}{\partial t} \tag{2.5}$$

where $H_r(\mathbf{r})$ and $H_t(t)$ are, respectively, the energy per unit volume and energy per unit time. When the laser pulse is short enough to satisfy the acoustic stress confinement, $H_t(t)$ can be approximated by a delta function.

2.2.2 Forward solution of optoacoustic wave equation in time domain

The optoacoustic equation in Eq. (2.5) can be solved using Green's function [42], which describes the profile of generated optoacoustic signal, when spatial and temporal impulse source is used:

$$\left(\nabla^2 - \frac{1}{c^2}\frac{\partial^2}{\partial t^2}\right) G(\mathbf{r},t;\mathbf{r}',t') = -\delta(\mathbf{r}-\mathbf{r}')\delta(t-t'), \tag{2.6}$$

where r' is the source location and t' is the time. Green's function can be solved as

$$G(\mathbf{r},t;\mathbf{r}',t') = \frac{\delta\left(t-t'-|\mathbf{r}-\mathbf{r}'|/c\right)}{4\pi|\mathbf{r}-\mathbf{r}'|}. \tag{2.7}$$

With the Green's function in Eq. (2.7) and the optoacoustic wave equation in Eq. (2.4), we can obtain the pressure due to an arbitrary source in an infinite medium:

$$p(\mathbf{r},t) = \frac{\Gamma}{4\pi c^2}\frac{\partial}{\partial t}\int \frac{H_r(\mathbf{r}')}{|\mathbf{r}-\mathbf{r}'|} H_t(t)\, d\mathbf{r}'\Big|_{t=|\mathbf{r}-\mathbf{r}'|/c} \tag{2.8}$$

A widely used optoacoustic time domain inversion formula is the universal back-projection (BP) algorithm [19], which has been analytically inverted from Eq. (2.8) for different detection geometries. The approximate analytical solution is given by [19]

$$H_r(r) = \int \left[2p(\mathbf{r}',t) - 2t\frac{\partial p(\mathbf{r}',t)}{\partial t}\right] dr'\Big|_{t=|\mathbf{r}-\mathbf{r}'|/c} \tag{2.9}$$

The back-projection algorithm is successful in detecting the position and shape of absorbing objects, even though Eq. (2.9) is not the exact solution [24]. However, this algorithm has several drawbacks. First, $t\partial p(\mathbf{r}',t)/\partial t$ □ $p(\mathbf{r}',t)$ exists in most cases (far-field acoustic detection) and the derivative part implies a ramp filter, which will enhance the boundaries and impair the low-frequency information in back-projection reconstruction. Second, negative values without physical meaning often appear in the reconstruction. Third, the algorithm cannot take detector

response into account. This highlights the need for model-based reconstructions for quantitative image reconstruction, which will be discussed in the following sections.

2.2.3 Time domain 2D forward modeling

The 2D time domain forward modeling used in this dissertation is based on discretization of Eq. (2.8) as described previously [35]. First, Eq. (2.8) is approximated as

$$p(\mathbf{r},t) \approx \frac{I(t+\Delta t) - I(t-\Delta t)}{2\Delta t} \tag{2.10}$$

where

$$I(t) = \int_l \frac{H_r(\mathbf{r}')}{|\mathbf{r}-\mathbf{r}'|} dl \Big|_{t=|\mathbf{r}-\mathbf{r}'|/c} \tag{2.11}$$

Eq. (2.11) is discretized by approximating the curve at a distance of $l = ct$ from the transducer's position and with N straight lines (Figure 2.2(a)). This set of straight lines covers an angle of $\alpha = 2\arcsin\left(\left(\sqrt{2}(n+1)\Delta xy\right)/2R\right)$, where n is the pixel number in the x and y directions, Δxy is the pixel size and R is the distance from the transducer to the center of the region of interest (ROI).

The integral $I(t)$ is then calculated from N discrete points of the curve l with positions $\mathbf{r}_l'$ (solid dots in Figure 2.2(a)) as

$$I(t) \approx \frac{1}{2}\sum_{l=1}^{N} \frac{H(\mathbf{r}_l')}{|\mathbf{r}-\mathbf{r}_l'|}\left(d_{l-1,l} + d_{l,l+1}\right) \tag{2.12}$$

where $d_{0,1} = d_{N,N+1} = 0$. $H(\mathbf{r}_l')$ is estimated by interpolating $H(\mathbf{r}')$ at pixel positions in the ROI. Combining Eq. (2.10) and Eq. (2.12), the pressure $p(\mathbf{r}_i, t_j)$ measured at position $\mathbf{r}_i$ and time t_j can be expressed as a linear combination of the absorbed energy at pixel position $\mathbf{r}_k'$ in the ROI:

$$p(r_i, t_j) = \sum_{k=1}^{nn} a_k^{i,j} H\left(r_k'\right) \tag{2.13}$$

where nn is the total number of pixels in the ROI. The coefficients $a_k^{i,j}$ can be calculated by interpolation methods in Figure 2.2(b). One typical method is bilinear interpolation, in which $H(r')$ is given by

$$H(x', y') = (1-\Delta x_a')(1-\Delta y_a')H_a + \Delta x_a'(1-\Delta y_a')H_b + \Delta x_a'\Delta y_a' H_c + (1-\Delta x_a')\Delta y_a' H_d. \tag{2.14}$$

where $\Delta x_a' = (x' - x_a')/\Delta xy$, $\Delta y_a' = (y_a' - y_a')/\Delta xy$ and $H_k = H(x_k', y_k')$.

Another typical method is right-angle triangles, in which $H(r')$ is given by

$$H(x', y') = \begin{cases} (1-\Delta x_a')H_a + \Delta y_a' H_c + (\Delta x_a' - \Delta y_a')H_b & if\ \Delta x_a' \geq \Delta y_a' \\ (1-\Delta y_a')H_a + \Delta x_a' H_c + (\Delta y_a' - \Delta x_a')H_d & if\ \Delta x_a' < \Delta y_a' \end{cases} \tag{2.15}$$

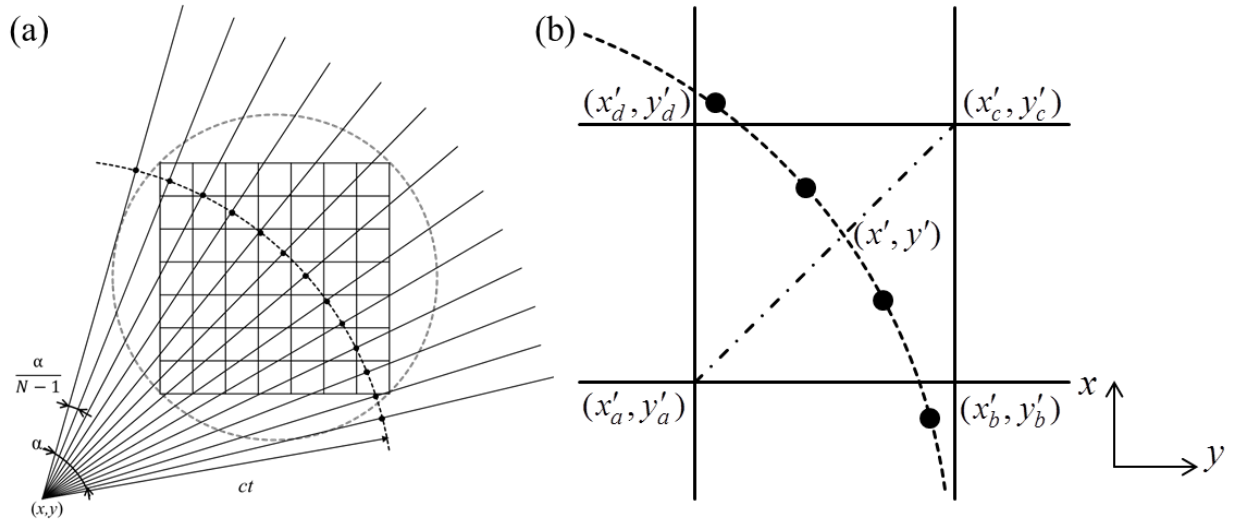

Figure 2.2 Discretization of the 2D forward model. (a) 2D discretization of the Poisson type integral. The curve l' is approximated by N points, indicated as solid dot points. (b) Interpolation of points along the discretized curve based on neighboring points on the grid.

When the pressure in Eq. (2.13) is computed for P transducer positions and for I time points, a linear equation can be formulated to express the transform from the image $\mathbf{z}$ (optical absorption) to the acoustic signals $\mathbf{p}$ by a model matrix $\mathbf{M}_{2D}$, which represents a 2D OAT system

$$\mathbf{p} = \mathbf{M}_{2D}\mathbf{z} \tag{2.16}$$

2.2.4 Time domain 3D forward modeling

The 3D time domain forward modeling used in this dissertation is based on discretization of Eq. (2.8) as described previously [34]. Similar to the 2D modeling in section 2.2.3, Eq. (2.8) is also approximated as

$$p(\mathbf{r},t) \approx \frac{I(\mathbf{r},t+\Delta t) - I(\mathbf{r},t-\Delta t)}{2\Delta t} \tag{2.17}$$

where

$$I(\mathbf{r},t) = \int \frac{H_r(\mathbf{r}')}{|\mathbf{r}-\mathbf{r}'|} dS'\Big|_{t=|\mathbf{r}-\mathbf{r}'|/c} \ . \tag{2.18}$$

Considering a spherical coordinate system centered at the transducer position $\mathbf{r}$, the surface element dS' at a distance ct from the transducer can be defined as

$$dS' = |\mathbf{r}-\mathbf{r}'|^2 \sin\theta d\varphi d\theta \tag{2.19}$$

where θ is the polar angle, and φ is the azimuthal angle. By combining Eq. (2.19) and Eq. (2.18), we get

$$I(\mathbf{r},t) = \int_{\phi}\int_{\theta} H_r(\mathbf{r}')|\mathbf{r}-\mathbf{r}'|\sin\theta d\varphi d\theta \ . \tag{2.20}$$

Eq. (2.20) can then be discretized with equal spacing of φ and θ on the surface S' at a distance of $\mathbf{r}_l'$:

$$I(\mathbf{r},t) \approx \Delta\varphi\Delta\theta\sum_l H(\mathbf{r}_l')|\mathbf{r}-\mathbf{r}_l'|\sin\theta_l \tag{2.21}$$

$\Delta\phi\Delta\theta$ can be discarded since it is a constant.

The solid spheres mesh in Figure 2.3(a) show a discrete reconstruction ROI located at positions $\mathbf{r}'_k$, covered by a grid of $n_{xy} \times n_{xy} \times n_z$ with pixel size $\Delta xy \times \Delta xy \times \Delta z$. $H(\mathbf{r}'_l)$ in Eq. (2.21) is discretized as a mesh of hollow spheres in Figure 2.3(a), and the value of $H(\mathbf{r}'_l)$ can be expressed as a function of the values at the eight neighboring points in the ROI mesh with trilinear interpolation as shown in Figure 2.3(b):

$$\begin{aligned} H(\mathbf{r}'_l) \approx\ & (1-\Delta x'_a)(1-\Delta y'_a)(1-\Delta z'_a)H_a + \Delta x'_a(1-\Delta y'_a)(1-\Delta z'_a)H_b \\ & + (1-\Delta x'_a)\Delta y'_a(1-\Delta z'_a)H_c + (1-\Delta x'_a)(1-\Delta y'_a)\Delta z'_a H_e \\ & + \Delta x'_a(1-\Delta y'_a)\Delta z'_a H_f + (1-\Delta x'_a)\Delta y'_a \Delta z'_a H_g \\ & + \Delta x'_a \Delta y'_a(1-\Delta z'_a)H_d + \Delta x'_a \Delta y'_a \Delta z'_a H_h \end{aligned} \tag{2.22}$$

where $\Delta x'_a = (x' - x'_a)/\Delta xy$, $\Delta y'_a = (y' - y'_a)/\Delta xy$, $\Delta z'_a = (z' - z'_a)/\Delta z$ and $H_k = H(x'_k, y'_k, z'_k)$. Combining Eq. (2.17), Eq. (2.21) and Eq. (2.22), the pressure at the position $\mathbf{r}_i$ and the time point t_j can be expressed as a linear combination of the value at the points of the grid, i.e.

$$p(\mathbf{r}_i, t_j) = \sum_{k=1}^{N} a_k^{i,j} H\left(\mathbf{r}'_k\right) . \tag{2.23}$$

This corresponds to the discrete forward model that establishes the pressure as a function of the absorbed energy in the 3D discrete ROI. The acoustic signal $\mathbf{p}$ for different transducer positions and time points can be computed by multiplying a 3D OAT system model matrix $\mathbf{M}_{3D}$ with a vector $\mathbf{z}$ representing the optical absorption grid, which is expressed in a matrix form similar to Eq. (2.16)

$$\mathbf{p} = \mathbf{M}_{3D}\mathbf{z} \tag{2.24}$$

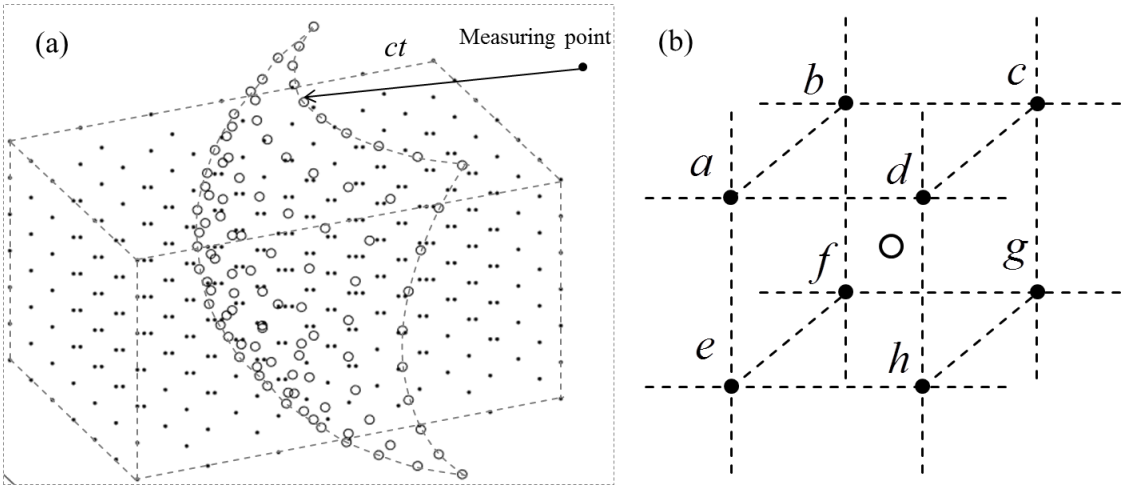

Figure 2.3 Discretization of the 3D forward model. (a) 3D discretization of the Poisson type integral. The ROI mesh is shown as solid spheres; the discretized integral mesh, as hollow spheres. (b) Trilinear interpolation with the eight neighboring points.

2.2.5 Finite-aperture detector modeling/Spatial impulse response

The signal detected by a finite-aperture detector with center position x_c is obtained by integrating the acoustic signal of a point detector $p(\mathbf{r},t)$ over the surface of the detector [43]

$$p_{\text{det}}(x_c,t) = \int p(\mathbf{r},t) D(x_c,\mathbf{r}) dr \tag{2.25}$$

where

$$D(x_c,\mathbf{r}) = \begin{cases} 1 & \mathbf{r} \in \textit{detector} \quad \textit{area} \\ 0 & \textit{else} \end{cases} \tag{2.26}$$

There are two ways to model the shape of the transducer. The first approach approximates the surface of the transducer by a set of points $x_S \in S$, so that the integral in Eq. (2.25) can be expressed as the summation of x_S

$$p_{\text{det}}(x_c,t) \approx \sum_{x_S \in S} p(x_S,t) \tag{2.27}$$

The pressure $p(x_S,t)$ for a point detector has been studied in Eq. (2.16), and assuming linearity, the model matrix $\mathbf{M}_{sum}$, which takes into account the effects of the finite-size transducer, can also be summed with the model matrices of individual points $x_S \in S$:

$$\mathbf{M}_{sum} = \sum_{x_S \in S} \mathbf{M}_{x_S} \tag{2.28}$$

such that the signal acquired by the transducer for a set of time points and transducer locations can be expressed as

$$\mathbf{p}_{\text{det}} = \mathbf{M}_{sum}\mathbf{z} \tag{2.29}$$

The accuracy of this procedure depends on the number of points used to discretize the detector shape, and this method has the flexibility to model any detector shape. Its only drawback is that it is slow for large detectors.

An alternative way to calculate $p_{\text{det}}(x_c,t)$ is the convolution the spatial impulse response (SIR) of a finite length line transducer with the optoacoustic wave $p(\mathbf{r},t)$ in Eq. (2.8) [27]:

$$p_{\text{det}}(x_c,t) = \frac{\Gamma}{4\pi c^2}\frac{\partial}{\partial t}\int \frac{D(x_c,\mathbf{r}) * H_r(\mathbf{r}')}{|\mathbf{r}-\mathbf{r}'|} dr' \Big|_{t=|\mathbf{r}-\mathbf{r}'|/c} \tag{2.30}$$

where c is the speed of sound in the medium, Γ is the Grueneisen parameter, $H_r(\mathbf{r})$ is the amount of energy absorbed in the tissue per unit volume, and * denotes the spatial convolution operator. The discretization of Eq. (2.30) can be expressed as the following linear relation:

$$\mathbf{p}_{\text{det}} = \mathbf{M}_{\text{det}}\mathbf{z} \tag{2.31}$$

In the case of a long line transducer where a lot of points would be needed to approximate the line for calculating the $\mathbf{M}_{sum}$, then model matrix $\mathbf{M}_{\text{det}}$ is preferable since it can be calculated much quicker.

2.3 Frequency domain optoacoustic imaging

2.3.1 Optoacoustic signal generation and wave equation in frequency domain

Analogous to the situation in time domain optoacoustic imaging, thermal and acoustic stress confinement in frequency domain optoacoustic imaging are governed by two characteristic frequencies, ω_{th} and ω_s, which are the inverses of the corresponding characteristic times τ_{th} and τ_s in Eqs. (2.1) and (2.2):

$$\omega > \omega_t = \frac{1}{\tau_{th}} = \frac{4D_T}{d_c^2} \tag{2.32}$$

$$\omega > \omega_s = \frac{1}{\tau_s} = \frac{c}{d_c} \tag{2.33}$$

where d_c is the characteristic dimension (targeted spatial resolution) and D_T is the thermal diffusivity and c is the speed of sound.

Under conditions of heat and acoustic stress confinement, the generation and propagation of frequency domain acoustic waves can be described by the following Helmholtz equation [37]

$$\nabla^2 p(\mathbf{r},\omega) + k^2 p(\mathbf{r},\omega) = -\frac{i\omega\beta}{C_p} H(\mathbf{r},\omega) \tag{2.34}$$

where $\mathbf{r}$ is the position, ω is the angular frequency, $p(\mathbf{r},\omega)$ is the Fourier transform of the acoustic pressure wave, $k = \omega / c$ is the acoustic wave number, $i = \sqrt{-1}$, β is the thermal expansion coefficient, C_p is the specific heat capacity, and $H(\mathbf{r},\omega)$ is the Fourier transform of the absorbing source.

2.3.2 Forward solution of optoacoustic wave equation in frequency domain

Green's function for a source in an unbounded medium has the solution [16]

$$p(\mathbf{r},\omega) = -\frac{i\omega\beta}{4\pi C_p} \int \frac{e^{ik|\mathbf{r}-\mathbf{r}'|}}{|\mathbf{r}-\mathbf{r}'|} H(\mathbf{r}',\omega)\, dr' \tag{2.35}$$

where r' is the source location.

2.3.3 Frequency domain 2D forward modeling

A schematic of frequency domain optoacoustic tomography is shown in Figure 2.4. The transducer scans 360° around the sample with P projections located at $\mathbf{r}_d$. The sample area is discretized as a square grid with pixel size d and N pixel nodes. Assuming an infinite and homogeneous medium, the pressure wave located at position r' is given by the Green's function solution in Eq. (2.35). Accordingly, the pressure $p(\mathbf{r}_d, \omega)$ at position $\mathbf{r}_d$ and modulation frequency ω can be given by the linear expression

$$\mathbf{p}(\omega) = \mathbf{M}(\omega)\mathbf{z} \tag{2.36}$$

where $\mathbf{p}(\omega)$ is a complex column vector denoting the measured complex signals (amplitude and phase of the pressure wave) at P projection positions, and $\mathbf{z}$ is a real vector representing the unknown absorption. $\mathbf{M}(\omega)$ is a complex matrix of dimensions $P \times N$:

$$\mathbf{M}(\omega) = -iAe^{i\theta_a}\begin{pmatrix} m_{11} & \cdots & m_{1n} \\ \vdots & \ddots & \vdots \\ m_{P1} & \cdots & m_{PN} \end{pmatrix} \tag{2.37}$$

where

$$m_{pn} = \omega \frac{e^{i(\omega(|\mathbf{r}(n)-\mathbf{r}_d(p)|/c))}}{|\mathbf{r}(n)-\mathbf{r}_d(p)|} \tag{2.38}$$

and where $\mathbf{r}_d(p)$ denotes the p th detector position, $\mathbf{r}(n)$ is the position of voxel n and A is a constant.

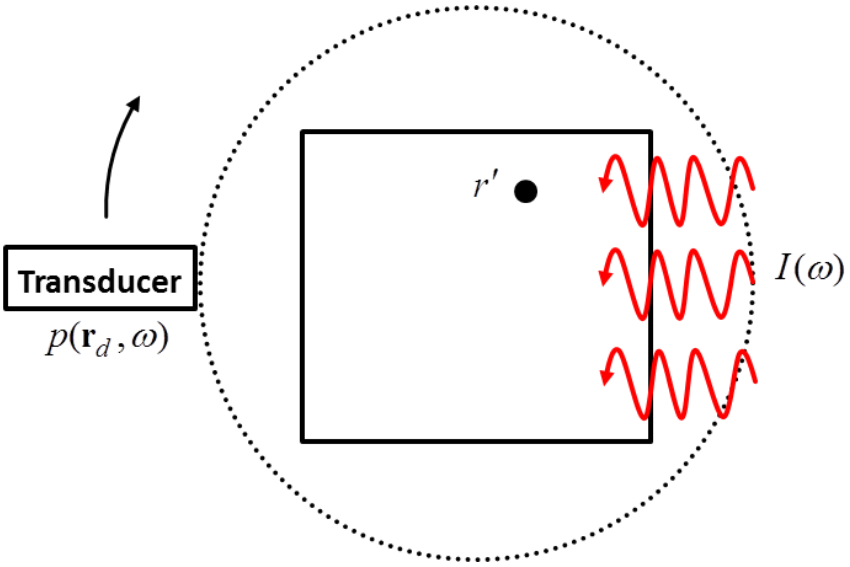

Figure 2.4 Schematic diagram of frequency domain optoacoustic tomography. The object is illuminated using an amplitude-modulated CW laser at a set of frequencies ω. The absorbing object located at $\mathbf{r}'$ emits acoustic waves, which are detected by the transducer at $\mathbf{r}_d$. The detected acoustic signal is then converted to phase and amplitude information using narrowband detection.

2.4 Traditional inversion methods

2.4.1 Least-squares inversion

The inversion of Eq. (2.16), Eq. (2.24), Eq. (2.31) and Eq. (2.36) can be seen as a least-squares minimization problem. Here $\mathbf{M}$ ($P \times N$) is used as a general model matrix to represent the optoacoustic system and the optoacoustic images can be generated by solving the least-squares problem as follows:

$$\arg\min_{\mathbf{z}} \left\| \mathbf{p} - \mathbf{M}\mathbf{z} \right\|_2^2 . \tag{2.39}$$

A common iterative algorithm to solve the least-squares minimization problem is Least squares QR (LSQR), which is described in Algorithm 2.1.

Algorithm 2.1 LSQR implementation

Inputs: $\mathbf{p}$, $\mathbf{M}$, η, max*Iter*

Output: $\mathbf{z}$

Step 1: Initialize a starting point $\mathbf{z}_0 = 0$, $\beta_1 = norm(\mathbf{p})$, $\mathbf{u}_1 = \mathbf{p}/\beta_1$, $\alpha_1 = norm(\mathbf{M}^{\mathrm{T}}\mathbf{u}_1)$, $\mathbf{v}_1 = (\mathbf{M}^{\mathrm{T}}\mathbf{u}_1)/\alpha_1$, $\mathbf{w}_1 = \mathbf{v}_1$ $\bar{\phi}_1 = \beta_1$, $\bar{\rho}_1 = \alpha_1$, $i = 1$.

Step 2: Continue the bidiagonalization: $\beta_{i+1} = norm(\mathbf{M}\mathbf{v}_i - \alpha_i\mathbf{u}_i)$, $\mathbf{u}_{i+1} = (\mathbf{M}\mathbf{v}_i - \alpha_i\mathbf{u}_i)/\beta_{i+1}$, $\alpha_{i+1} = norm(\mathbf{M}^{\mathrm{T}}\mathbf{u}_i - \beta_i\mathbf{v}_i)$, $\mathbf{v}_{i+1} = (\mathbf{M}^{\mathrm{T}}\mathbf{u}_i - \beta_i\mathbf{v}_i)/\alpha_{i+1}$.

Step 3: Construct and apply the next orthogonal transformation: $\rho_i = \sqrt{\bar{\rho}_i^2 + \beta_{i+1}^2}$, $c_i = \bar{\rho}_i/\rho_i$, $s_i = \beta_{i+1}/\rho_i$, $\theta_i = s_i\alpha_{i+1}$, $\bar{\rho}_{i+1} = -c_i\alpha_{i+1}$, $\phi_i = c_i\bar{\phi}_i$, $\bar{\phi}_{i+1} = s_i\bar{\phi}_i$.

Step 4: Update $\mathbf{z}$ and $\mathbf{w}$. $\mathbf{z}_i = \mathbf{z}_{i-1} + (\phi_i/\rho_i)\mathbf{w}_i$, $\mathbf{w}_{i+1} = \mathbf{v}_{i+1} - (\theta_i/\rho_i)\mathbf{w}_i$.

Step 5: Check the stopping criterion. If $\left(\left\|\mathbf{p} - \mathbf{M}\mathbf{z}_{i+1}\right\|_2 - \left\|\mathbf{p} - \mathbf{M}\mathbf{z}_i\right\|_2\right)/\left\|p\right\|_2 < \eta$ or $i > \max Iter$, finish; otherwise, $i = i+1$ and go to Step 2.

2.4.2 L2-norm/Tikhonov regularized least-squares inversion

A L2-norm/Tikhonov regularization term can be included in the least-squares minimization in Eq. (2.39) in order to solve the ill-posed problems [44]

$$\arg\min_{\mathbf{z}} \left(\left\|\mathbf{p} - \mathbf{M}\mathbf{z}\right\|_2^2 + \lambda \left\|\mathbf{L}\mathbf{z}\right\|_2^2 \right) \tag{2.40}$$

where $\lambda \geq 0$ is the regularization parameter and $\mathbf{L}$ is the Tikhonov regularization matrix. $\mathbf{L}$ can be an identity matrix or other operators. Eq. (2.40) can be turned into a least-squares minimization problem and solved by the LSQR algorithm in Algorithm 2.1:

$$\arg\min_{\mathbf{z}} \left\| \begin{bmatrix} \mathbf{M} \\ \lambda\mathbf{L} \end{bmatrix} \mathbf{z} - \begin{bmatrix} \mathbf{p} \\ \mathbf{0} \end{bmatrix} \right\|_2^2 \tag{2.41}$$

2.4.3 Moore-Penrose pseudo-inversion with truncated singular value decomposition

Singular value decomposition (SVD) is a factorization of a real or complex matrix. SVD of a matrix $\mathbf{M}$ can be formed as

$$\mathbf{M} = \mathbf{U}\Sigma\mathbf{V}^{\mathrm{T}} \tag{2.42}$$

where $\mathbf{U}$ is a $m \times m$ unitary matrix, Σ is a diagonal $m \times n$ matrix with non-negative real numbers on the diagonal representing singular values, $^{\mathrm{T}}$ denotes the transpose operation, and $\mathbf{V}^{\mathrm{T}}$ is an $n \times n$ unitary matrix.

$$\Sigma = diag(\sigma_1, \sigma_2, ..., \sigma_n) \tag{2.43}$$

where $\sigma_1 \geq \sigma_2 \geq ... \geq \sigma_r > \sigma_{r+1} = ... = \sigma_n = 0$ and $r = rank(\mathbf{M})$.

The goal of truncated singular value decomposition (TSVD) and Tikhonov regularization is to dampen the contributions from errors in measurement $\mathbf{p}$ (noise). TSVD is achieved by neglecting the components of the solution corresponding to the partial smallest singular values, since these are likely to contribute heavily to the solution. Thus, the TSVD of $\mathbf{M}$ is defined as the rank-k matrix.

$$\mathbf{M}_k = \mathbf{U}\mathbf{\Sigma}_k\mathbf{V}^{\mathrm{T}} = \sum_{i=1}^{k} u_i \sigma_i v_i^{\mathrm{T}}, \mathbf{\Sigma}_k = diag\left(\sigma_1, ..., \sigma_k, 0, ..., 0\right) \in R^{m \times n} \tag{2.44}$$

where $k \leq r$, u_i and v_i are the columns of the matrices $\mathbf{U}$ and $\mathbf{V}$, respectively. When k is chosen properly, the condition number of $\mathbf{M}_k$ (σ_1 / σ_k) will be small. The TSVD solution to Eq. (2.39) is defined by:

$$\mathbf{z} = \mathbf{M}_k^{+}\mathbf{p} \ . \tag{2.45}$$

The pseudo-inverse matrix $\mathbf{M}_k^{+}$ is:

$$\mathbf{M}_k^{+} = \mathbf{V}\mathbf{\Sigma}_k^{+}\mathbf{U}^{\mathrm{T}}, \mathbf{\Sigma}_k^{+} = diag\left(\sigma_1^{-1}, ..., \sigma_k^{-1}, 0, ..., 0\right) \in R^{n \times m} \ . \tag{2.46}$$

The advantage of this approach is that the pseudo-inverse matrix may be pre-calculated for a given system and then simply reapplied to each new dataset, thus reducing the image reconstruction problem to a matrix-vector multiplication operation. The drawback of this approach is that it is impartial to apply SVD decomposition when the matrix is too big.

2.4.4 L-curve method for selection of the regularization parameter

The L-curve is a log-log plot of the norm of a regularized component versus the norm of the corresponding residual norm, since the regularization parameter varies [44]. The L-curve can give insight into the regularizing properties of the underlying regularization method, and it is an aid to choose an appropriate regularization parameter for the given data and regularization method.

If too much regularization is imposed on the solution, it will not fit the given data $\mathbf{p}$ properly and the residual norm $\|\mathbf{M}\mathbf{z}_\lambda - \mathbf{p}\|_2$ will be too large (where $\mathbf{z}_\lambda$ is the regularized solution with regularization parameter λ). On the other hand, if too little regularization is imposed, then $\|\mathbf{M}\mathbf{z}_\lambda - \mathbf{p}\|_2$ will be good but the regularization part will be too large. Here we use Tikhonov regularization as an example to explain the L-curve.

The 'best' regularization parameter λ lies in a more or less distinct corner of the L-curve $\left(\log\|\mathbf{M}\mathbf{z}_\lambda - \mathbf{p}\|_2, \log\|\mathbf{L}\mathbf{z}_\lambda\|_2\right)$. This corner separates the flat part of the curve where regularization errors dominate, from the vertical part of the curve where noise dominates. At this corner the curvature κ of the L-curve is maximal.

3 System analysis and fast reconstruction for finite-aperture detectors with wavelet packet

Optoacoustic tomography employs relatively large detectors to achieve high detection sensitivity. Spatial-averaging effects over large detector areas may lead to attenuation of high acoustic frequencies and, subsequently, loss of fine features in the reconstructed image. Model-based reconstruction algorithms improve image resolution in such cases by correcting for the effect of the detector's aperture on the detected signals. However, the incorporation of the detector's geometry in the optoacoustic model significantly increases the amount of memory needed for model matrix, which hinders the application of inversion and analysis tools such as singular value decomposition. In this chapter we demonstrate the use of the wavelet-packet framework for optoacoustic systems with finite-aperture detectors. The decomposition of the model matrix in the wavelet-packet domain leads to model matrices sufficiently small to apply SVD. This methodology is demonstrated to reduce inversion time more than 10-fold for simulated and experimental data. In addition, the proposed framework for assessing inversion stability is demonstrated, which reveals a non-monotonic dependency of the system condition number on detector size, which has not been reported before. Thus, the proposed framework may assist in choosing the optimal detector size in future optoacoustic systems.

Some of the material in this chapter has been presented in the following publication in a very similar or identical form to the text in this chapter:

"Optoacoustic imaging reconstruction and system analysis method for finite-aperture detectors under the wavelet-packet framework" by Yiyong Han, Vasilis Ntziachristos and Amir Rosenthal, *Journal of Biomedical Optics*, 21(1), 016002, 2016.

3.1 Introduction

One of the commonly used classes of algorithms for optoacoustic image formation is the back-projection (BP) reconstruction [19]. Despite their ubiquity, BP algorithms reflect an ideal representation of the optoacoustic problem and are exact only in a few imaging geometries that involve point-like detectors, which will generate reconstruction inaccuracies and artifacts in systems with finite-aperture detectors. Model-based reconstruction algorithms represent a potent alternative to the BP approaches owing to their generality in accounting for system- and geometry-related parameters [24], [29], [45]–[47]. For instance, model-based algorithms have succeeded in accounting for the effects of a detectors' aperture and limited projection geometry [27], [30], [38]. In the model-based approach implemented in this dissertation, termed interpolated-model-matrix-inversion (IMMI), the model matrix that describes the optoacoustic imaging system can be pre-calculated in advance for analysis and can easily undergo algebraic inversion to accelerate the reconstruction [27], [46].

The main disadvantage of model-based reconstruction algorithms is their high computational cost in terms of complexity and memory; this cost scales nonlinearly with the number of reconstructed image pixels. The use of computationally expensive inversion algorithms such as SVD therefore often limits the reconstruction grid to low resolution. Although IMMI is now commonly employed in 2D OAT inversions [48], [49], the lengthy computational times have restricted the widespread use of model-based approaches and make them unsuitable, for example, in real-time MSOT applications [50] or 3D problems [38], [51].

Recently, a wavelet-packet (WP) framework was introduced to reduce the computational demands of model-based reconstruction algorithms [52]. The use of wavelet packets enables the decomposition of the model matrix into significantly smaller matrices, each corresponding to a different spatial frequency band in the image. Inversion is thus performed on a set of reduced matrices rather than on a single large matrix. This approach (WP-IMMI) substantially reduces

the memory requirement for image reconstruction. However, WP-IMMI assumes ideal point detectors and so does not consider the distortion in detected signal in the case of finite-aperture detectors. Currently, the WP framework has been validated only for optoacoustic designs that employ point detectors.

In this chapter we adapt the WP framework for imaging scenarios in which finite-aperture detectors are used, namely detectors that are flat along one of their lateral axes and that can be modeled in 2D using line segments. The proposed generalized WP-IMMI for finite-aperture detectors (GWP-IMMI-FAD) method is demonstrated as a tool for both image reconstruction and analysis of how detector characteristics influence reconstruction quality. For example, we analyze the reconstruction stability of the different spatial frequency bands for several detector lengths using SVD. This analysis allows comparison of reconstructions characteristics obtained with detectors of varying lengths, and it identifies which patterns in the image are most difficult to reconstruct. Image reconstruction by GWP-IMMI-FAD involves inversion of the reduced model matrices using TSVD with global thresholding, which contrasts with the local thresholding used elsewhere [52]. Global thresholding means that the algorithm can be applied even in cases where some spatial frequency bands in the imaged object are impossible to reconstruct.

In the examples presented below, we demonstrate GWP-IMMI-FAD for image reconstruction for a detector length of 13 mm for simulated and experimental data in both full- and limited-view imaging scenarios. We discuss the potential of GWP-IMMI-FAD as a design tool for optoacoustic systems and as an acceleration that can complete reconstructions faster than IMMI with finite-aperture detector (IMMI-FAD) and generate higher-quality images than BP approaches.

The rest of the chapter is organized as follows. In section 3.2, we introduce 2D optoacoustic imaging system with single element transducer used for this chapter. In section 3.3, we state the motivation of the work. Section 3.4 presents 2D wavelet packet decomposition framework. Section 3.5 describes the details of the proposed GWP-IMMI-FAD method. The results of simulations and experiments are presented in section 3.6 and 3.7, and the discussion and conclusions are given in section 3.8.

3.2 2D optoacoustic imaging system with single element transducer

The experimental optoacoustic results in this chapter were imaged with the 2D optoacoustic tomography system previously described [53] in Figure 3.1. Briefly, a tunable optical parametric oscillator (OPO) (MOPO-700 series, Newport Corp., Mountain View, CA) pumped by a Q-switched Nd:YAG laser (Quanta-Ray Lab-Series 190-30 Newport), provided 650-nm pulses lasting <10 ns at a 30 Hz repetition frequency. The laser beam was expanded to about 2 cm and split into two beams, allowing uniform illumination around the imaged object. The laser pulse fluence on the surface of imaged objects was kept under 20 mJ/cm^2 in order to meet laser safety standards [13]. A 15-MHz cylindrically focused transducer (V319, Panametrics-NDT, Waltham, MA) was used to image a microspheres phantom with a detection radius of 19.05 mm and an element diameter of 13 mm, while a 7.5-MHz cylindrically focused transducer (V320, Panametrics-NDT, Waltham, MA) with a detection radius of 25.9 mm and an element diameter of 13 mm was used to image mouse brain. Figure 3.1(b) is a photography of the above mentioned cylindrically focused transducer. In order to improve the signal-to-noise ratio of the signals, each projection was obtained by averaging 32 independent measurements. The microspheres phantom was transparent agar containing a thin layer with numerous dark polymer microspheres (Cospheric LLC, Santa Barbara, CA) with a diameter of ~100. For small-animal imaging, the *ex vivo* brain of a six-day-old mouse was measured using the experimental setup described above.

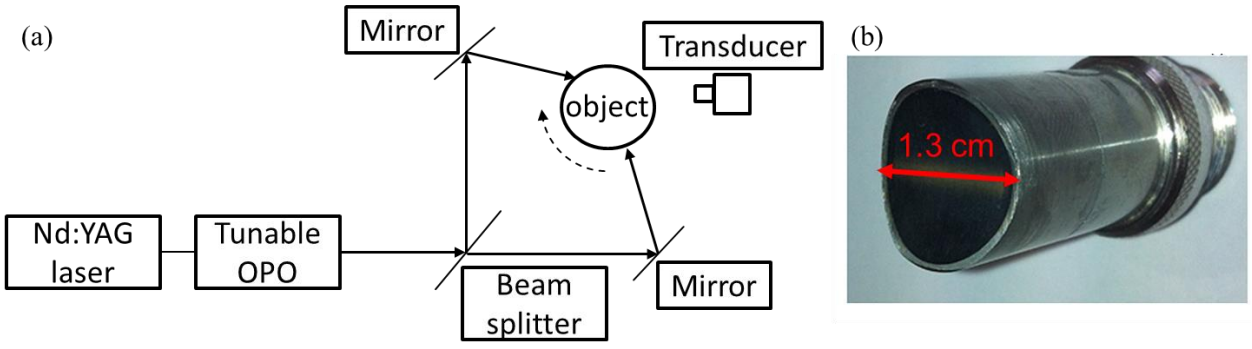

Figure 3.1 Diagram of the optoacoustic tomography setup (a) Diagram of the optoacoustic tomography setup. (b) Photograph of a single element transducer.

3.3 Problem statement

The model-based reconstruction for a finite-aperture size transducer is described in section 2.2.5 and involves the following matrix relation:

$$\mathbf{p}_{\mathbf{det}} = \mathbf{M}_{\mathbf{det}}\mathbf{z} \tag{3.1}$$

where $\mathbf{p}_{\text{det}}$ is a column vector representing the measured acoustic waves at various detector positions and times; $\mathbf{z}$ is a column vector representing the object values; and $\mathbf{M}_{\text{det}}$ is the forward model matrix.

The following discussion assumes a 360º projection circular-detection geometry with a radius of 4 cm and line-segment detectors of various lengths up to 20 mm. The image grid is 150×150 (2 cm $\times$ 2 cm). A total of 360 projections/measurements are taken at uniform intervals over 360º; each projection has 489 time points. The size of the model matrix $\mathbf{M}_{\text{det}}$ is 176040×22500. To store all the elements of the model matrix $\mathbf{M}_{\text{det}}$ as double class, 39 GB of memory are needed. However, when only nonzero matrix elements are saved (matrix sparsity), the memory required to store the matrix falls to 0.7-2.7 GB, depending on the length of the detector (Figure 3.2). Thus, the high memory requirements make pseudo-inversion unsuitable for calculating $\mathbf{M}_{\text{det}}^{\dagger}$ in high-resolution imaging.

Tikhonov regularization-based inversion (section 2.4.2) may be applied to matrices that are significantly larger than those on which TSVD may be practically applied, facilitating the reconstruction of high-resolution images. For example, in limited-view scenarios [30], [38], [54], the tomographic data may not be sufficient to accurately reconstruct all the features in the images. In such cases, the model matrix $\mathbf{M}_{\text{det}}$ is ill-conditioned and its inversion requires regularization, which can suppress the effects of noise and artifacts in the image, e.g. stripe artifacts that appear with limited tomographic views [30].

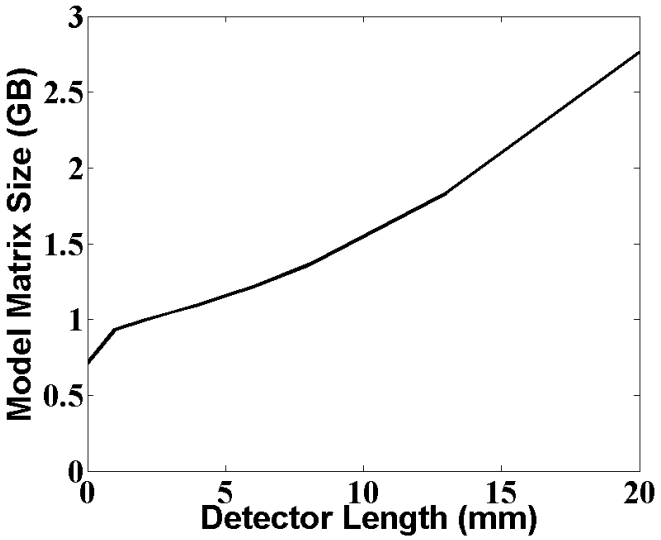

Figure 3.2 Amount of memory required to store the model matrix described in Sec. 2.2.5 when sparsity is exploited (only non-zero entries are saved). The longer the detector is, the more memory is required. Without sparsity, the matrix occupies 39 GB of memory. (taken from [26])

3.4 2D Wavelet packets

All wavelet packets/wavelet in this thesis are presented in the discrete form as conjugate mirror filter banks [55], so only orthogonal wavelets, such as the Daubechies wavelets, are considered. The Daubechies wavelets are not defined in terms of the resulting scaling and wavelet functions; instead they are generated numerically using the cascade algorithm [55]. Both the scaling sequence $h[n]$ (Low-pass filter) and the wavelet sequence $g[n]$ (high-pass Filter) will here be normalized to have sum equal $\sqrt{2}$, and both sequences (Assume have a length of $2L$) and all shifts of them by an even number of coefficients are orthonormal to each other.

$$g[n] = \begin{cases} h[2L+1-n] & n \to odd \\ -h[2L+1-n] & n \to even \end{cases} \tag{3.2}$$

A first level discrete wavelet decomposition of a 2D signal $U[x, y]$ ($x = 1...X; y = 1...Y$) is shown in Figure 3.3 and defined as

$$a[x, y] = \mathbf{A}U[i, j] = \sum_{i,j=-\infty}^{\infty} h[i-2x]h[j-2y]U[i, j] \tag{3.3}$$

$$d_1[x,y] = \mathbf{D_1}U[i,j] = \sum_{i,j=-\infty}^{\infty} h[i-2x]g[j-2y]U[i,j] \tag{3.4}$$

$$d_2[x,y] = \mathbf{D}_2U[i,j] = \sum_{i,j=-\infty}^{\infty} \mathrm{g}[i-2x]\mathrm{h}[j-2y]U[i,j] \tag{3.5}$$

$$d_3[x,y] = \mathbf{D}_3U[i,j] = \sum_{i,j=-\infty}^{\infty} \mathrm{g}[i-2x]g[j-2y]U[i,j] \tag{3.6}$$

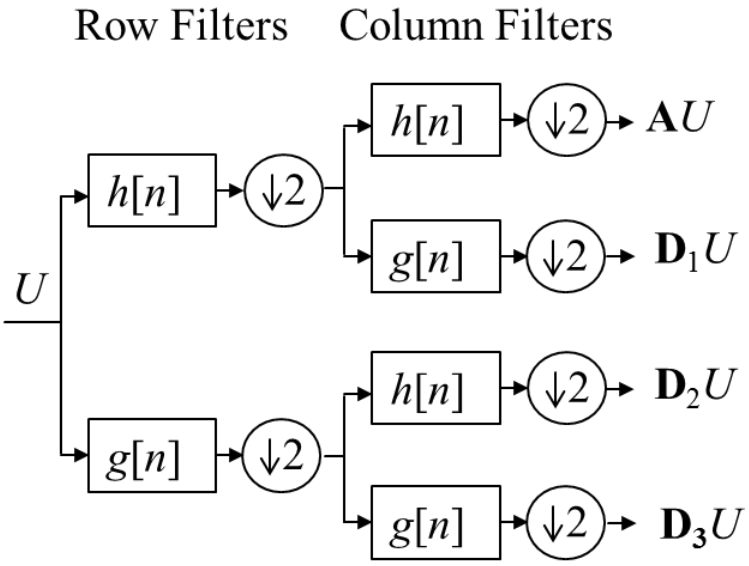

Figure 3.3 First level of 2D wavelet packet decomposition with scaling sequence and wavelet sequence.

The wavelet reconstruction formula is given as

$$\begin{aligned} U[x,y] = & \sum_{i,j=-\infty}^{\infty} h[x-2i]h[y-2j]a[i,j] \\ & + \sum_{i,j=-\infty}^{\infty} h[x-2i]g[y-2j]d_1[i,j] \\ & + \sum_{i,j=-\infty}^{\infty} g[x-2i]h[y-2j]d_2[i,j] \\ & + \sum_{i,j=-\infty}^{\infty} g[x-2i]g[y-2j]d_3[i,j] \end{aligned} \tag{3.7}$$

$\mathbf{A}$ represents the low-passing operation to get the approximation coefficients $a[x, y]$, whereas $\mathbf{D}_1$, $\mathbf{D}_2$ and $\mathbf{D}_3$ represent high-passing operation to get the three detail coefficients $d_1[x, y]$, $d_2[x, y]$,and $d_3[x, y]$ over horizontal, vertical and diagonal axes [55]. Only the approximation coefficients are further decomposed in wavelet decomposition, whereas both approximation and detail coefficients will be further decomposed wavelet-packet decomposition. A full-tree decomposition of level/depth I is defined as decomposition where all coefficients were decomposed I time. A schematic description of a decomposition of level 2 is shown in Figure 3.4. Each leaf corresponds to a distinct spectral band, where all the spectral bands have approximately the same bandwidth.

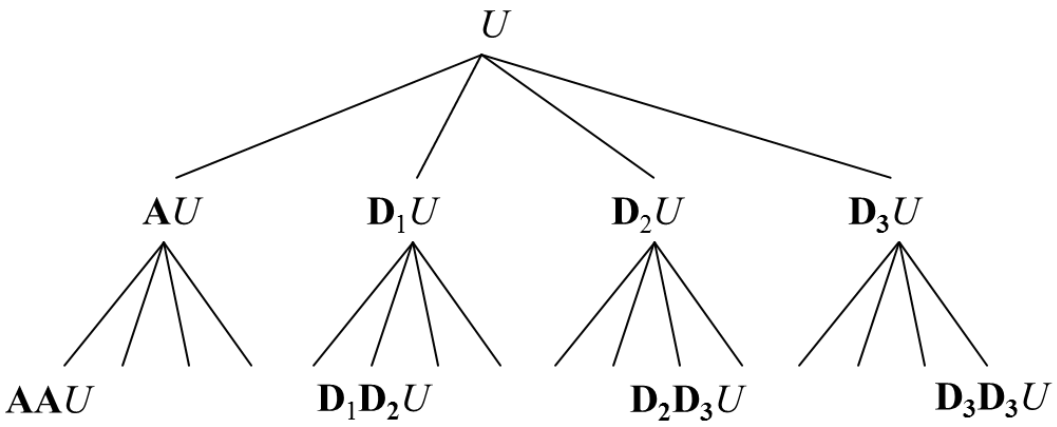

Figure 3.4 Full-tree 2D wavelet packet decomposition of level 2.

3.5 Methods

The proposed reconstruction method, GWP-IMMI-FAD, is described as follows. First, we define $\mathbf{z}_w$ as the WP-coefficient vector of the object, where the reconstruction of $\mathbf{z}$ from $\mathbf{z}_w$ is given by

$$\mathbf{z} = \mathbf{R}\mathbf{z}_w \tag{3.8}$$

where $\mathbf{R}$ is the reconstruction matrix of the WP transform [52]. Similarly, we define $\mathbf{p}_w$ as the WP-coefficient vector of the projection data by using the decomposition matrix $\mathbf{D}$ of the WP transform [52]:

$$\mathbf{p}_w = \mathbf{D}\mathbf{p} \ . \tag{3.9}$$

Substituting Eq. (2.31) and Eq. (3.8) in Eq. (3.9) , we obtain

$$\mathbf{p}_w = \mathbf{D}\mathbf{M}_{\text{det}}\mathbf{R}\mathbf{z}_w \tag{3.10}$$

For a given leaf i or spatial frequency band in object decomposition space, the corresponding model matrix is

$$\mathbf{M}_w^i = \mathbf{D}\mathbf{M}_{\text{det}}\mathbf{R}^i \tag{3.11}$$

The approximate matrix $\bar{\mathbf{M}}_w^i$ and the approximate vector $\bar{\mathbf{p}}_w^i$ are calculated out of $\mathbf{M}_w^i$ and $\mathbf{p}_w^i$ for each leaf by keeping only the significant rows [52], yielding the following relation:

$$\mathbf{M}_w^i = \mathbf{D}\mathbf{M}_{\text{det}}\mathbf{R}^i \tag{3.12}$$

Eq. (3.12) may be inverted separately for each i , e.g. by using TSVD. For each frequency band, SVD is performed on the corresponding approximate matrix $\bar{\mathbf{M}}_w^i$:

$$\bar{\mathbf{M}}_w^i = \mathbf{U}^i\mathbf{\Sigma}^i\mathbf{V}^{i,\mathrm{T}} \tag{3.13}$$

where $^{\mathrm{T}}$ denotes the transpose operation; $\mathbf{U}^i$ and $\mathbf{V}^i$ are unitary matrices; and $\mathbf{\Sigma}^i$ is a diagonal matrix containing the singular values of the decomposition: $\left\{\sigma_j^i\right\}_{j=1\ldots J}$.

The condition number of each approximate matrix $\bar{\mathbf{M}}_w^i$ is calculated *locally* [52], based on its corresponding singular values [56]:

$$\kappa_{\text{loc}}^i\left(\bar{\mathbf{M}}_w^i\right) = \frac{\mathbf{max}_j\left(\left|\sigma_j^i\right|\right)}{\mathbf{min}_j\left(\left|\sigma_j^i\right|\right)} \tag{3.14}$$

Based on this definition, $\kappa_{\mathrm{loc}}^{i}\left(\bar{\mathbf{M}}_{w}^{i}\right)$ can reveal only whether in a specific spatial frequency band some components' reconstruction is more unstable than others. $\kappa_{\mathrm{loc}}^{i}\left(\bar{\mathbf{M}}_{w}^{i}\right)$ does not, however, enable a comparison between different spatial frequency bands in terms of reconstruction robustness. We therefore introduce for each approximate matrix $\bar{\mathbf{M}}_{w}^{i}$ a condition number that is calculated *globally*:

$$\kappa_{\mathrm{glob}}^{i}\left(\bar{\mathbf{M}}_{w}^{i}\right)=\frac{\mathbf{max}_{i,j}\left(\left|\sigma_{j}^{i}\right|\right)}{\mathbf{min}_{j}\left(\left|\sigma_{j}^{i}\right|\right)} \tag{3.15}$$

The use of $\kappa_{\mathrm{glob}}^{i}\left(\bar{\mathbf{M}}_{w}^{i}\right)$ enables classifying the different spatial frequency bands based on their reconstruction robustness. The maximum of $\kappa_{\mathrm{glob}}^{i}\left(\bar{\mathbf{M}}_{w}^{i}\right)$, i.e. $\max_{i}\kappa_{\mathrm{glob}}^{i}\left(\bar{\mathbf{M}}_{w}^{i}\right)$, is therefore an approximation to the condition number of the model matrix $\mathbf{M}_{\mathrm{det}}$ used in Eq. (2.31).

The inversion of $\bar{\mathbf{M}}_{w}^{i}$ using TSVD requires excluding all the singular values below a certain threshold. An individual threshold is determined *locally* for each matrix $\bar{\mathbf{M}}_{w}^{i}$ [52] and is proportional to its corresponding maximum singular value:

$$\mathrm{th}_{\mathrm{loc}}^{i}=\alpha\mathbf{max}_{j}\left(\left|\sigma_{j}^{i}\right|\right) \tag{3.16}$$

This choice of local thresholds enables regularization only when the image component that corresponds to the maximum singular value in each frequency band can be stably reconstructed. In other words, local thresholds cannot be used when one or more image components in a certain image band cannot be reconstructed. In this case, the algorithm would fail to reject the entire frequency band. Therefore, we introduce a single *global* threshold in this work, defined as

$$\mathrm{th}_{\mathrm{glob}}=\alpha\mathbf{max}_{i,j}\left(\left|\sigma_{j}^{i}\right|\right) \tag{3.17}$$

Once the TSVD has been performed for all i in Eq. (3.13), the recovered image coefficients in the WP domain $\mathbf{z}_w^i$ may be used to calculate the image via Eq. (3.8). Mathematically, the entire reconstruction procedure may be described by the equation:

$$\mathbf{z}_0 = \bar{\mathbf{M}}^{\dagger}\mathbf{p} \ , \tag{3.18}$$

where $\bar{\mathbf{M}}^{\dagger}$ is the approximated inverse matrix of $\bar{\mathbf{M}}$, which can be determined by TSVD, and $\mathbf{z}_0$ is the approximate solution. The initial approximation may be improved recursively by using [52]

$$\mathbf{z}_n = \mathbf{z}_{n-1} + \beta\bar{\mathbf{M}}^{\dagger}(\mathbf{p} - \mathbf{M}_{\text{det}}\mathbf{z}_{n-1}) \tag{3.19}$$

where $\mathbf{z}_n$ is the solution at the nth iteration and β is a constant.

3.6 Simulation results

3.6.1 Analysis of image reconstruction stability

The ability to perform SVD on the reduced approximate matrices $\bar{\mathbf{M}}_w^i$ enables us to analyze the reconstruction stability for the different spatial frequency bands in the image. In the following discussion, we analyze the reconstruction stability of a 2D image based on data collected with a 360º projection circular-detection geometry with a radius of 4 cm and line detectors of various lengths. We consider an image grid with 150×150 pixels (2 cm $\times$ 2 cm). The size of the model matrix $\mathbf{M}_{\text{det}}$ is 176040×22500. Two-level WP decomposition is performed with the Daubechie 6 wavelet, leading to 16 distinct spatial frequency bands [Figure 3.5(a)]. Figure 3.5(b-d) show the value of $\kappa_{\text{glob}}^i\left(\bar{\mathbf{M}}_w^i\right)$ for the various frequency bands for a point detector, line detector 6 mm long, or line detector 13 mm long. As expected, the effect of spatial averaging reduces the reconstruction stability in the higher spatial frequencies. Figure 3.5(e) shows the value of the maximum global condition number of the reduced modal matrices $\mathbf{max}_i\left[\kappa_{\text{glob}}^i\left(\bar{\mathbf{M}}_w^i\right)\right]$ for various detector lengths. Interestingly, $\mathbf{max}_i\left[\kappa_{\text{glob}}^i\left(\bar{\mathbf{M}}_w^i\right)\right]$ does not monotonically increase with detector length, but rather reaches a maximum value at a length of 6 mm.

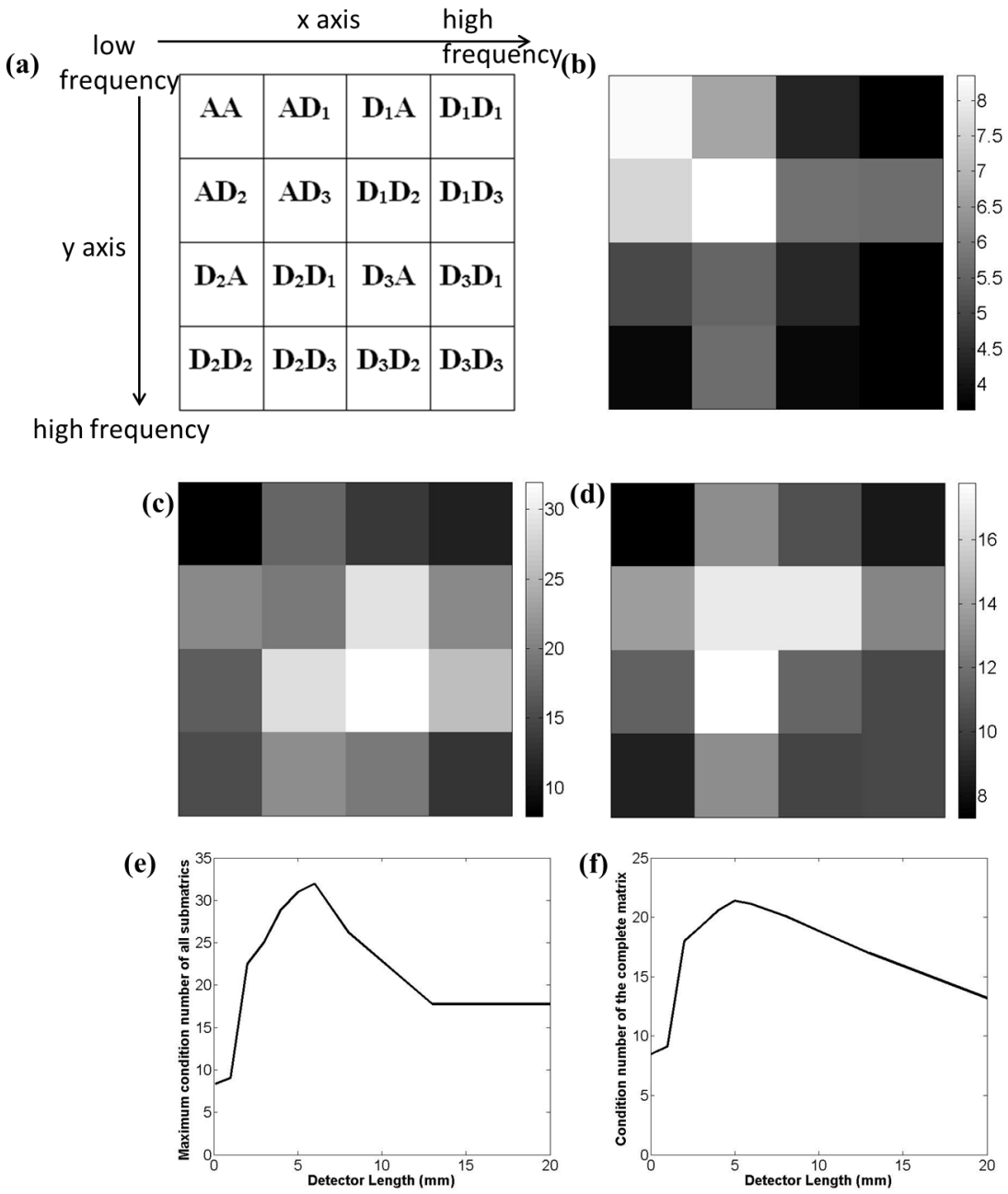

Figure 3.5 Condition Number of the Model Matrix. (a) Map of decomposition components with two-level wavelet packets. (b-d) Condition number map of the decomposed model matrix for a point detector, line detector 6 mm long, and line detector 13 mm long. (e) Maximum condition number of all decomposition matrices with different detector lengths. (f) Condition number of the model matrix with different detector lengths. (taken from [26])

To verify the non-monotonic dependency of the condition number on detector length, the condition number of the model matrix $\mathbf{M}_{det}$ was calculated directly for various detector lengths. The result [Figure 3.5(f)] reveals the same behavior as that observed in WP-based analysis. For calculation of the condition number, the function 'condest' in Matlab was used, which is based on the 1-norm condition estimator of Hager [57]. This algorithm gives an estimate for the condition number without performing SVD, enabling easy implementation despite the size of the model matrix. Nevertheless, the condition-number calculations in Figure 3.5(f) required the use of a PC workstation with 160 GB of RAM, whereas the SVD performed on the reduced matrices $\bar{\mathbf{M}}_w^i$ for Figure 3.5(b-e) were executed on a standard desktop computer with only 16 GB of Random access memory (RAM).

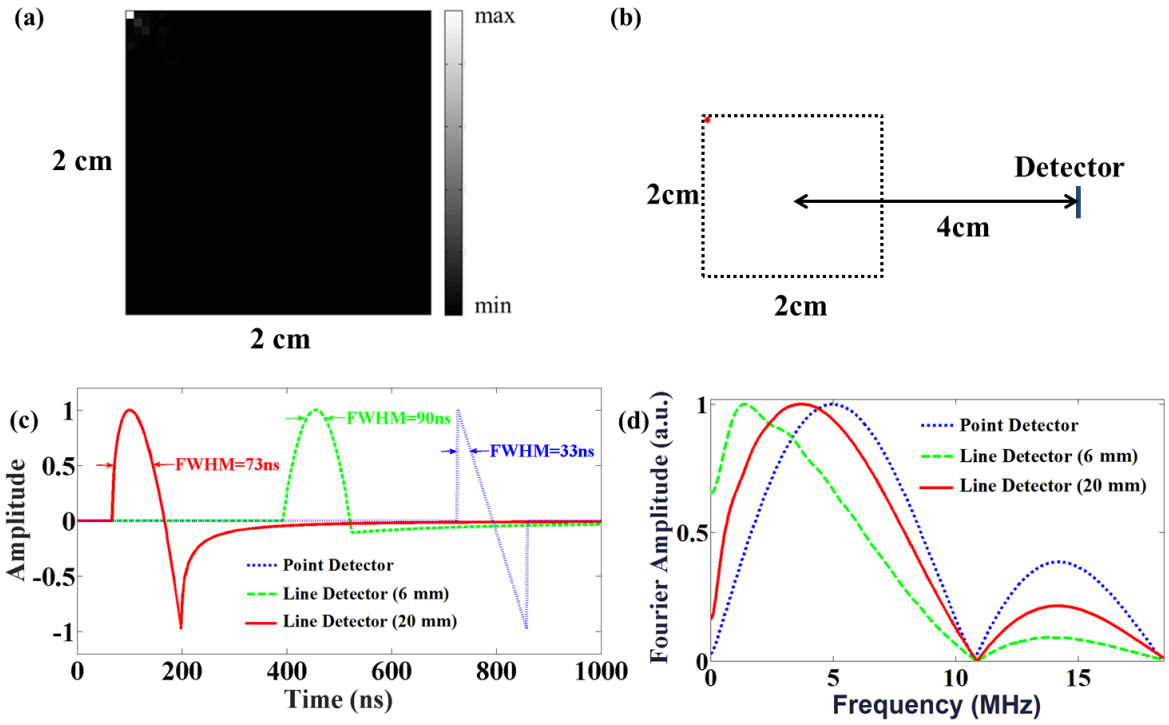

Figure 3.6 Optoacoustic signals detected from the sphere by detectors of various lengths. (a) The image generated by the row in $\mathbf{v}^i$, which corresponds to the minimum singular value in all the matrices $\bar{\mathbf{M}}_w^i$ calculated with a detector length of 6 mm. The result corresponds to the image for which reconstruction is expected to show the greatest instability. (b) An illustration of a spherical source with a radius of 200 μm positioned at the location identified in panel (a). (c) The signals detected from the sphere by detectors of various lengths and (d) their corresponding frequency content. (taken from [26])

Table 3.1 Parameters of 9 spheres to generate 100 random numerical phantoms. (taken from [26])

Index	$(\underline{x}_i, \underline{y}_i)$		$\underline{R}_i$		$\underline{A}_i$	
	mean [mm]	STD [mm]	mean [mm]	STD [mm]	Mean [a.u.]	STD [a.u.]
1	(0.001,-0.001)	(0.028,0.028)	0.915	0.031	0.301	0.113
2	(0.002,-0.005)	(0.028,0.029)	0.752	0.028	0.134	0.115
3	(-0.243,-0.396)	(0.028,0.031)	0.119	0.028	0.472	0.117
4	(0.152,-0.499)	(0.029,0.031)	0.121	0.029	0.478	0.114
5	(-0.395,-0.005)	(0.029,0.028)	0.251	0.026	0.252	0.111
6	(0.197,0.055)	(0.029,0.030)	0.247	0.032	0.269	0.116
7	(-0.892, -0.898)	(0.026,0.033)	0.097	0.034	0.962	0.113
8	(-0.858,0.902)	(0.031,0.028)	0.079	0.022	0.971	0.105
9	(0.817,0.807)	(0.023,0.028)	0.079	0.024	0.980	0.123

The advantage of GWP-IMMI-FAD is that it enables not only the identification of frequency bands most susceptible to noise in the reconstruction, but also the identification of their spatial patterns. This may be achieved by visualizing the rows in $\mathbf{V}^i$ corresponding to the minimum singular values in each frequency band. Figure 3.6(a) shows the image generated from the row of $\mathbf{V}^i$ that corresponds to the smallest singular value in the frequency band for which the highest condition number was obtained in the case of a 6 mm detector. The figure shows that the highest susceptibility to noise occurs at the periphery of the image. To verify this result, we simulated the signal of a spherical source with a diameter of 200 μm at the top-left corner of the image [(Figure 3.6(b)]. Figure 3.6(c) shows the signals detected by a point detector, a line detector 6 mm long and a line detector 20 mm long; Figure 3.6(d) shows their frequency content. The

signals presented in Figure 3.6(c) were calculated using previously described analytical solutions [43], not based on the model matrices. The figures reveal more substantial loss of high-frequency data using the 6-mm detector than the 20-mm detector.

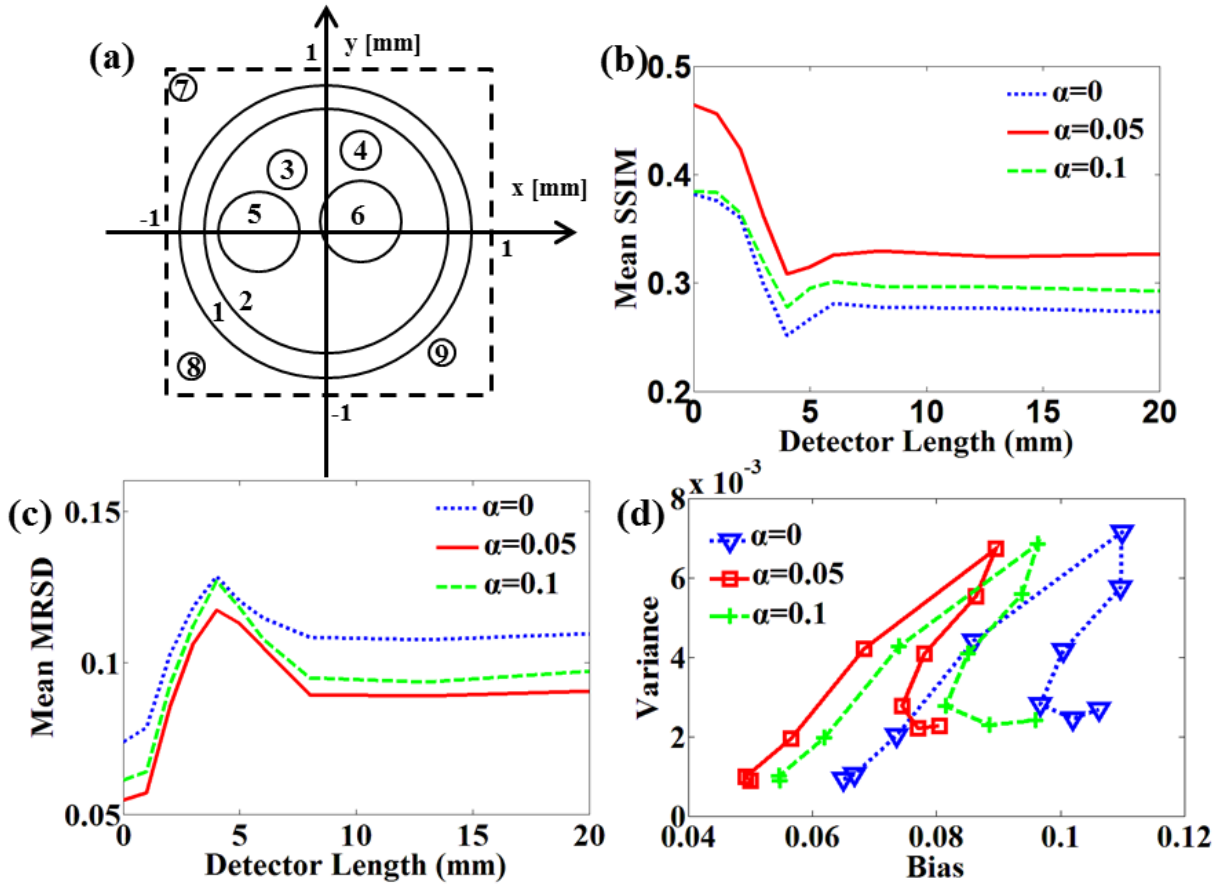

Figure 3.7 Evaluation of the reconstructions for numerical spheres phantoms in Table 3.1. (a) Schematic illustration of a random object function. (b) Mean SSIM of random objects with different detector lengths and regularization parameters. (c) Mean RMSD of random objects with different detector lengths and regularization parameters. (d) Bias-variance curve of the reconstructions for a point detector and for flat detectors with lengths of 1, 2, 3, 4, 5, 6, 8, 13, and 20 mm. Three values of α were considered (0, 0.05, and 0.1). For all detector lengths, bias and variance were higher at α = 0 (no regularization) than at the other α values. The worst bias and variance were obtained with a flat detector 4 mm long. (taken from [26])

In order to further demonstrate the validity of the results obtained by GWP-IMMI-FAD, object images were generated by a random process similar to one previously described [45]. The images were reconstructed via TSVD with GWP-IMMI-FAD and several values of α in Eq. (3.17). Each image consisted of nine smooth spheres (indexed by i for $i = 1,...,9$) with random

origins [denoted by ($\underline{x}_i, \underline{y}_i$)], radii ($\underline{R}_i$), and absorbed optical energy densities ($\underline{A}_i$). A representative image is provided in Figure 3.7(a). We generated 100 random images, whose statistics are listed in Table 3.1. The model matrix was built using IMMI-FAD [27], then this matrix was used to generate all synthetic projection data. The mean of the Gaussian white noise set in the projection data was 0, while the standard deviation (STD) was 2% of the maximum magnitude of the projection data. Statistical assessment of reconstruction performance with different regularization parameters is shown in Figure 3.7(b-d). The quality of the reconstructed images was quantified by calculating the structural similarity (SSIM) and root-mean-square-deviation (RMSD) between the reconstructed and original images, as well as by performing bias-variance analysis [58]:

$$\mathrm{SSIM}(x, y) = \frac{(2\mu_x\mu_y + C_1)(2\sigma_{xy} + C_2)}{(\mu_x^2 + \mu_y^2 + C_1)(\sigma_x^2 + \sigma_y^2 + C_2)}, \tag{3.20}$$

where x and y represent the original and reconstructed image; μ_x and μ_y are the corresponding means; σ_x^2 and σ_y^2 are the corresponding variances; C_1 and C_2 are small positive constants; and σ_{xy} is the covariance between the images. SSIM can range from 0 to 1, with higher values corresponding to greater similarity between the images. RMSD is expressed by

$$\mathrm{RMSD}=\sqrt{\frac{1}{N}\sum_{i=1}^{N}(x_i - y_i)^2}, \tag{3.21}$$

where x_i and y_i are the pixel values of the original and reconstructed images, and N is the number of pixels.

To calculate variance and bias for each of the random phantoms, reconstruction was performed for $M = 100$ different additive noise signals generated from a Gaussian distribution with a zero mean and STD of 2% of the maximum projection data. For each pixel, the variance and bias were calculated using the equations

$$\mathrm{Var}_i = \frac{1}{M}\sum_{j=1}^{M}\left(y_i - \frac{1}{M}\sum_{j=1}^{M} y_i \right)^2, \tag{3.22}$$

$$\mathrm{Bias}_i = \frac{1}{M}\sum_{j=1}^{M} y_i - x_i, \tag{3.23}$$

where x_i and y_i represent the values of the i^{th} pixel in the original and reconstructed images, respectively; i is the pixel index; and j=1…M is the index of the added noise signal. The results for the variance and bias were averaged over all pixels and are presented in Figure 3.4(d) for a point detector and for flat detectors with lengths of 1, 2, 3, 4, 5, 6, 8, 13 and 20 mm. Three values of α were considered (0, 0.05 and 0.1).

3.6.2 Image reconstruction for simulated data

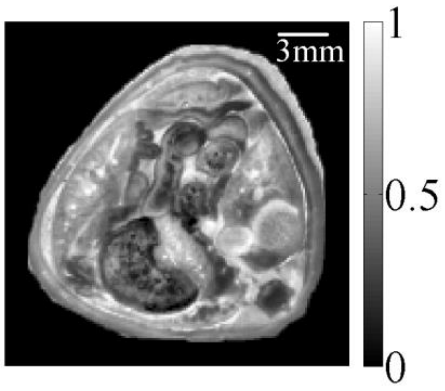

Figure 3.8 The numerical phantom used in the simulations. (taken from [26])

A numerical study was performed for full- and limited-view scenarios in order to analyze imaging performance based on the following reconstruction schemes: BP (section 2.2.2), IMMI (section 2.2.3) with 20 L2-LSQR iterations, IMMI-FAD (section 2.2.5) with 20 L2-LSQR iterations and the proposed GWP-IMMI-FAD. All reconstructed images were normalized. A mouse cross-section (Figure 3.8) was used as the original image (150 × 150 pixels, 2 cm × 2 cm), and detection was performed over a circle surrounding the image using a line-segment detector 13 mm long located 4 cm from the origin. The model matrix was built by IMMI-FAD and used to generate all the synthetic projection data, and all reconstructions were performed in the presence of added noise, which was generated from a Gaussian distribution with a zero mean and

STD of 2% of the maximum projection data. In all cases, the detector was moved in 1° increments. Reconstructions were performed in Matlab on a personal computer with an Intel Core i7 2.1 GHz processor and 16 GB of RAM.

In the reconstructions performed with IMMI and IMMI-FAD, the model matrix was invertedd using Tikhonov regularization. The L-curve method in section 2.4.4 was used to find the Tikhonov regularization parameter λ [59]. In the case of GWP-IMMI-FAD, the WP decomposition was performed using the Daubechies 6 mother wavelet with two-level full-tree decomposition for both the model matrix and projection data, and inversion was performed using TSVD. The L-curve method in section 2.4.4 was also used to find the regularization parameter α [59]. Figure 3.9 shows the simulation reconstruction results in a full-view scenario. Figure 3.9(a-d) show the reconstructions using BP, IMMI, IMMI-FAD and GWP-IMMI-FAD. Figure 3.9(e) shows a 1D slice of the reconstructed image taken along the yellow dashed line in Figure 3.9(c). The IMMI reconstruction without accounting for the detector geometry gives a blurry reconstructed image, as predicted [43], while reconstructions with IMMI-FAD and GWP-IMMI-FAD are not blurry. The respective SSIMs between the original image and Figure 3.9(a-d) are 0.0753, 0.7023, 0.7748 and 0.7780; the corresponding RMSDs are 0.3860, 0.0961, 0.0357 and 0.0367. The total processingtime needed to build the wavelet-packet decomposition matrices in advance was approximately 1.2 hours. TSVD was used in GWP-IMMI-FAD, where truncation was performed by setting $\alpha = 0.02$ in Eq. (3.17). Nine iterations of Eq. (3.19) were performed in GWP-IMMI-FAD, with each iteration lasting 1 s. In this way, after pre-calculation of the matrices, GWP-IMMI-FAD required only 10 s, whereas Tikhonov regularized IMMI-FAD required 215 s.

Figure 3.10 shows the images reconstructed from the noisy simulation data for the limited-view scenario in which only the projections on the left side of the images were used (180-degree angular coverage). Figure 3.10(a-d) show the reconstructions made using BP, IMMI, IMMI-FAD and GWP-IMMI-FAD. For comparison, Figure 3.10(e) shows the reconstruction obtained via WP-IMMI-FAD involving local thresholding [Eq. (3.14)] and the same α value as the one used in Figure 3.10(d). Figure 3.10(f) compares the profiles of absorbed energy density at the same position in Figure 3.10(c) for the original image and reconstructions made using IMMI-FAD and GWP-IMMI-FAD. The respective SSIMs between the original image and Figure 3.10(a-e) are

0.0552, 0.4504, 0.6266, 0.6212 and 0.6090; the corresponding RMSDs are 0.4114, 0.1858, 0.0833, 0.0792 and 0.0890. In GWP-IMMI-FAD, TSVD was used in GWP-IMMI-FAD, where truncation was performed using $\alpha = 0.1$ in Eq. (3.17). The total processing time needed to build the WP decomposition matrices in advance was approximately 40 minutes. Six iterations of Eq. (3.19) were used for the proposed method, and each iteration required 1 s. As a result, the reconstruction time of GWP-IMMI-FAD was only 7 s, whereas IMMI-FAD required 104 s.

3.7 Experimental results

We applied GWP-IMMI-FAD to experimental optoacoustic data obtained from a microspheres phantom and a mouse brain. The microspheres reconstruction was set to a size of 2 cm $\times$ 2 cm and 200×200 pixels, while the mouse brain reconstruction was set to 1.3 cm $\times$ 1.3 cm and 130×130 pixels. All reconstructed images were normalized to their maximum, and negative values in the images were set to zero.

3.7.1 Microsphere phantom experiment

Figure 3.11(a-d) show the full-view microsphere reconstructions obtained with BP, IMMI, IMMI-FAD and GWP-IMMI-FAD. In GWP-IMMI-FAD, TSVD was used and truncation was performed using $\alpha = 0.16$ in Eq. (3.17). The reconstruction by GWP-IMMI-FAD is considerably sharper than those by BP and IMMI, and similar to the one by IMMI-FAD. After pre-calculation of all matrices, the GWP-IMMI-FAD reconstruction (10 iterations) took only 80 s, whereas the IMMI-FAD reconstruction required 1646 s.

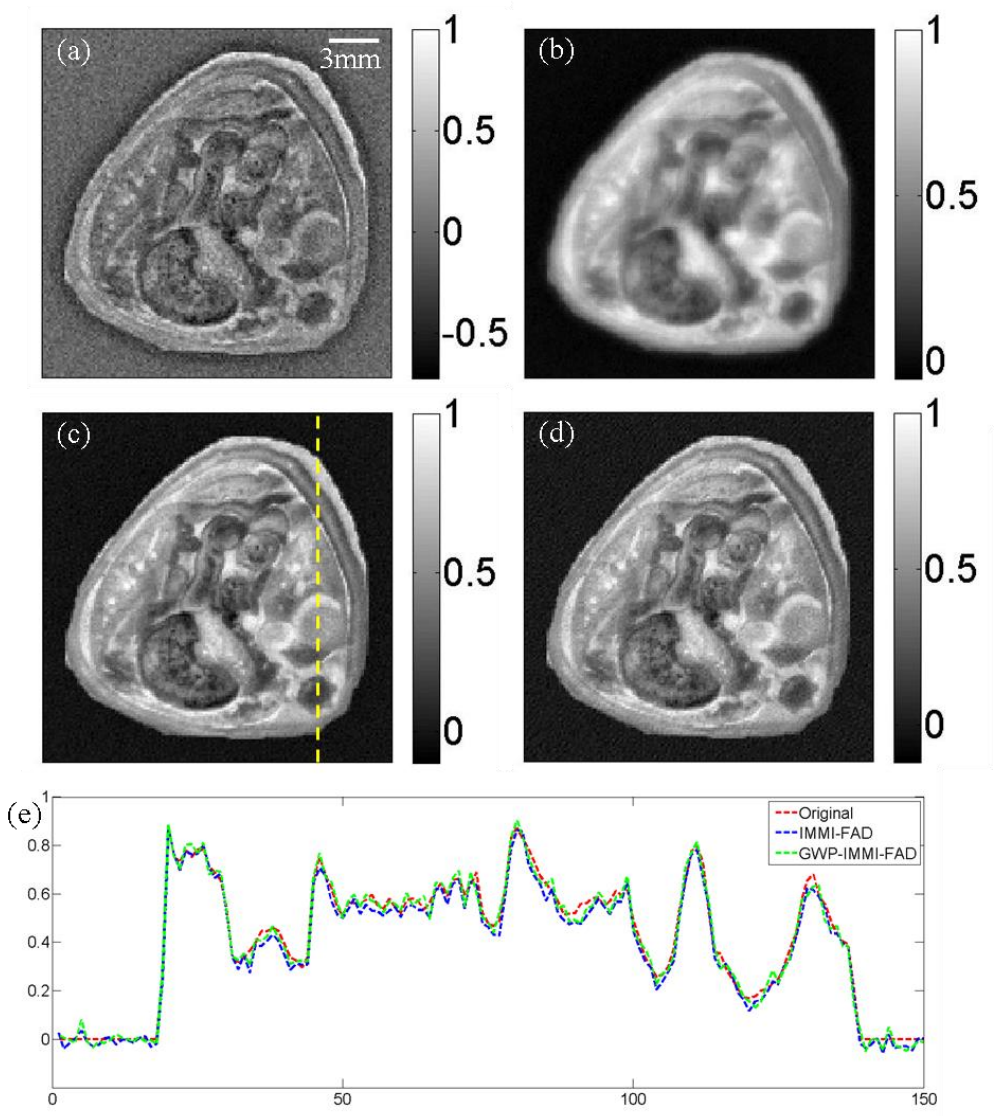

Figure 3.9 Reconstructions of the numerical mouse phantom for the case of full-view, noisy data using (a) BP, (b) IMMI, (c) IMMI-FAD, (d) GWP-IMMI-FAD. (e) Profiles of absorbed energy density along the yellow dashed line in panel (c) for the original image and for reconstructions prepared using IMMI-FAD or GWP-IMMI-FAD. (taken from [26])

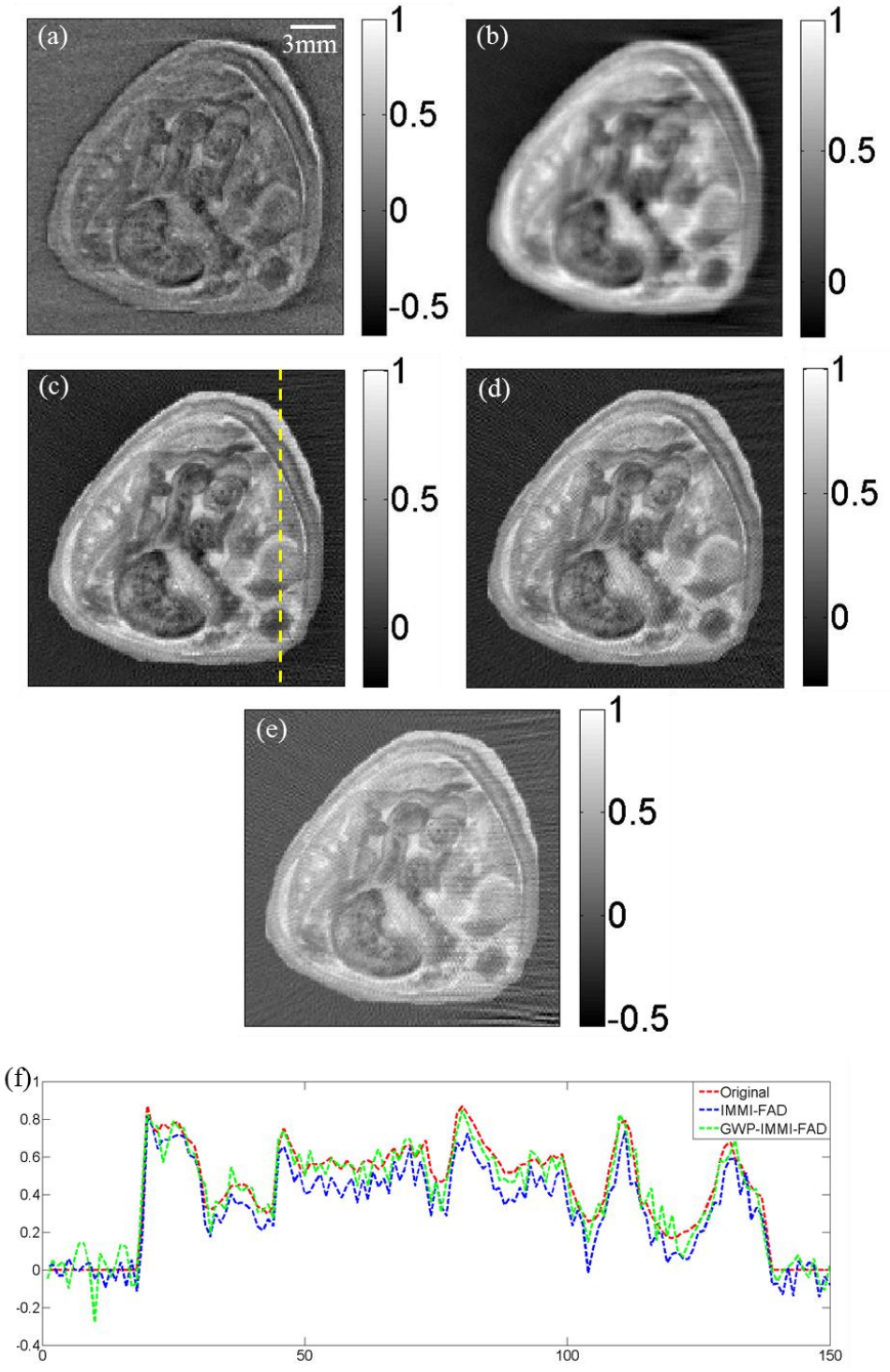

Figure 3.10 Reconstructions of the numerical mouse phantom for the case of noisy, limited-view data (projections spanning 180º on the left plane only) using (a) BP, (b) IMMI, (c) IMMI-FAD, (d) GWP-IMMI-FAD and (e) WP-IMMI-FAD. (f) Profiles of absorbed energy density along the yellow dashed line in panel (c) for the original image and for reconstructions using IMMI-FAD or GWP-IMMI-FAD. (taken from [26])

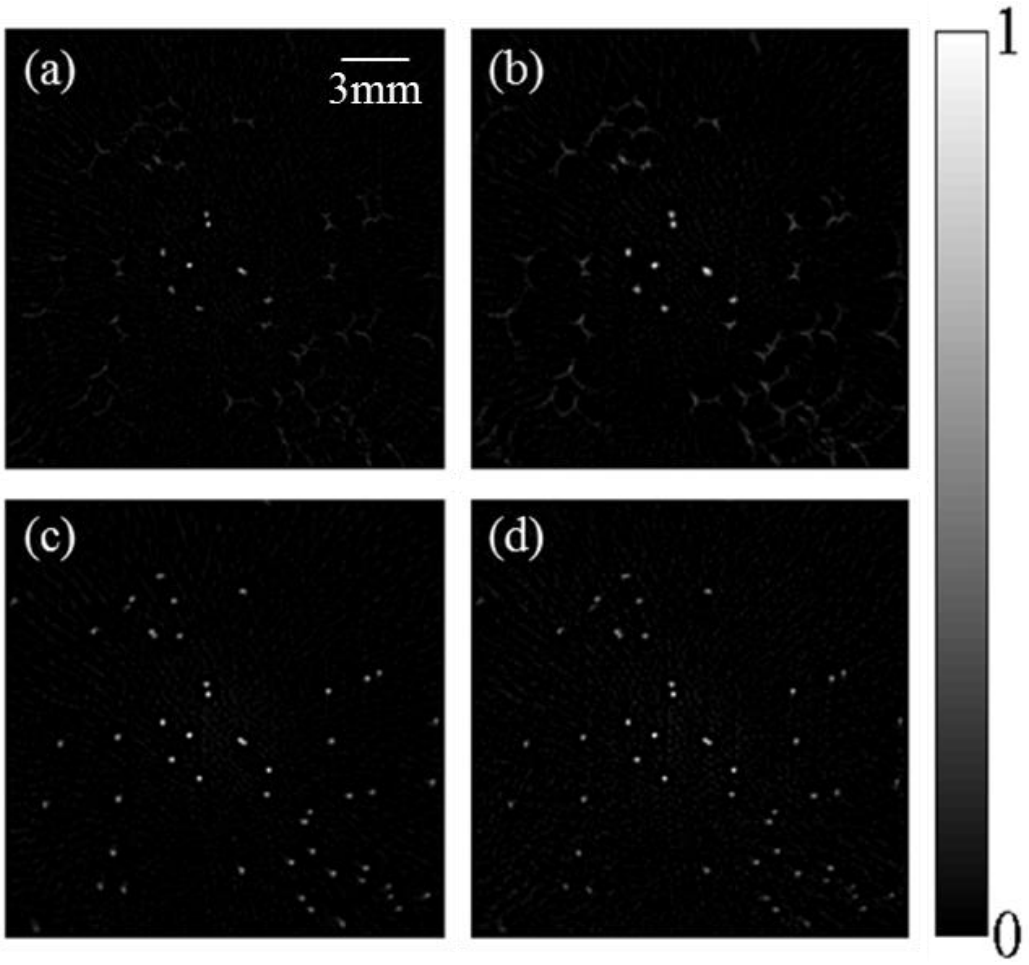

Figure 3.11 Optoacoustic reconstructions of microspheres from experimental data using (a) BP, (b) IMMI, (c) IMMI-FAD and (d) GWP-IMMI-FAD. (taken from [26])

3.7.2 Mouse brain experiment

Figure 3.12(a-d) show full-view reconstructions of mouse brain obtained by BP, IMMI, IMMI-FAD and GWP-IMMI-FAD. TSVD was used in GWP-IMMI-FAD and truncation was performed using $\alpha = 0.08$ in Eq. (3.17). The reconstruction based on model matrices that took into account the effects of line-segment detectors is sharper than the reconstruction based on a point detector. The differences between Figure 3.12(c) and Figure 3.12(d) are small and difficult to see by visual inspection. After pre-calculation of all matrices, the GWP-IMMI-FAD reconstruction (10 iterations) took only 11 s, whereas the IMMI-FAD reconstruction required 197 s.

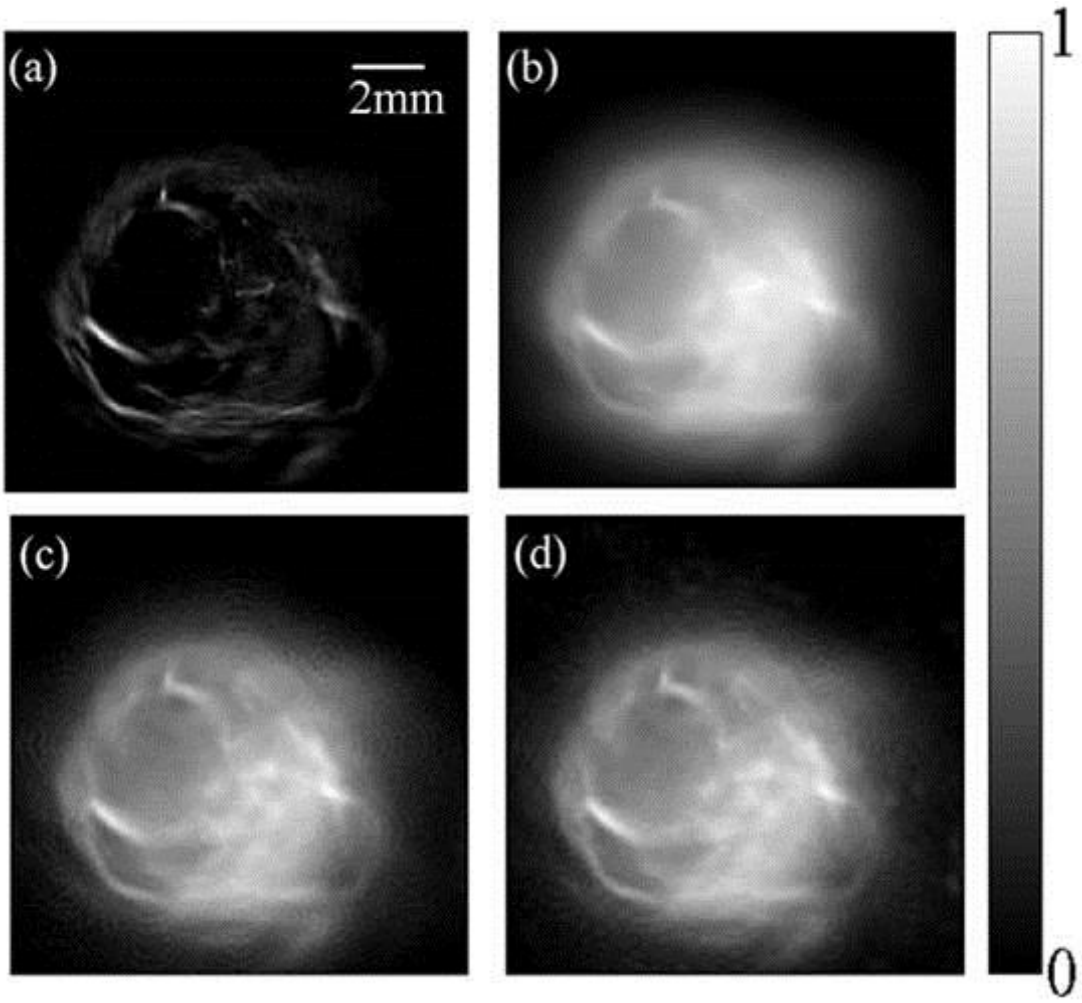

Figure 3.12 Optoacoustic reconstructions of a mouse brain from experimental data using (a) BP, (b) IMMI, (c) IMMI-FAD and (d) GWP-IMMI-FAD. (taken from [26])

GWP-IMMI-FAD was experimentally demonstrated for limited-view projection data of the mouse brain, in which the angular coverage of the projection data was reduced to 180 degrees. Figure 3.13(a-c) show the reconstructions using BP, IMMI and IMMI-FAD, and Figure 3.13(d) presents the reconstruction using GWP-IMMI-FAD with 7 iterations. For TSVD of each matrix, the truncation was performed using $\alpha = 0.1$ in Eq. (3.17). Use of GWP-IMMI-FAD with TSVD suppresses the stripe artifact better than IMMI-FAD (Figure 3.13). After pre-calculation of the model matrix and reduced matrices, GWP-IMMI-FAD reconstruction took only 8 s, whereas IMMI-FAD reconstruction required 90 s.

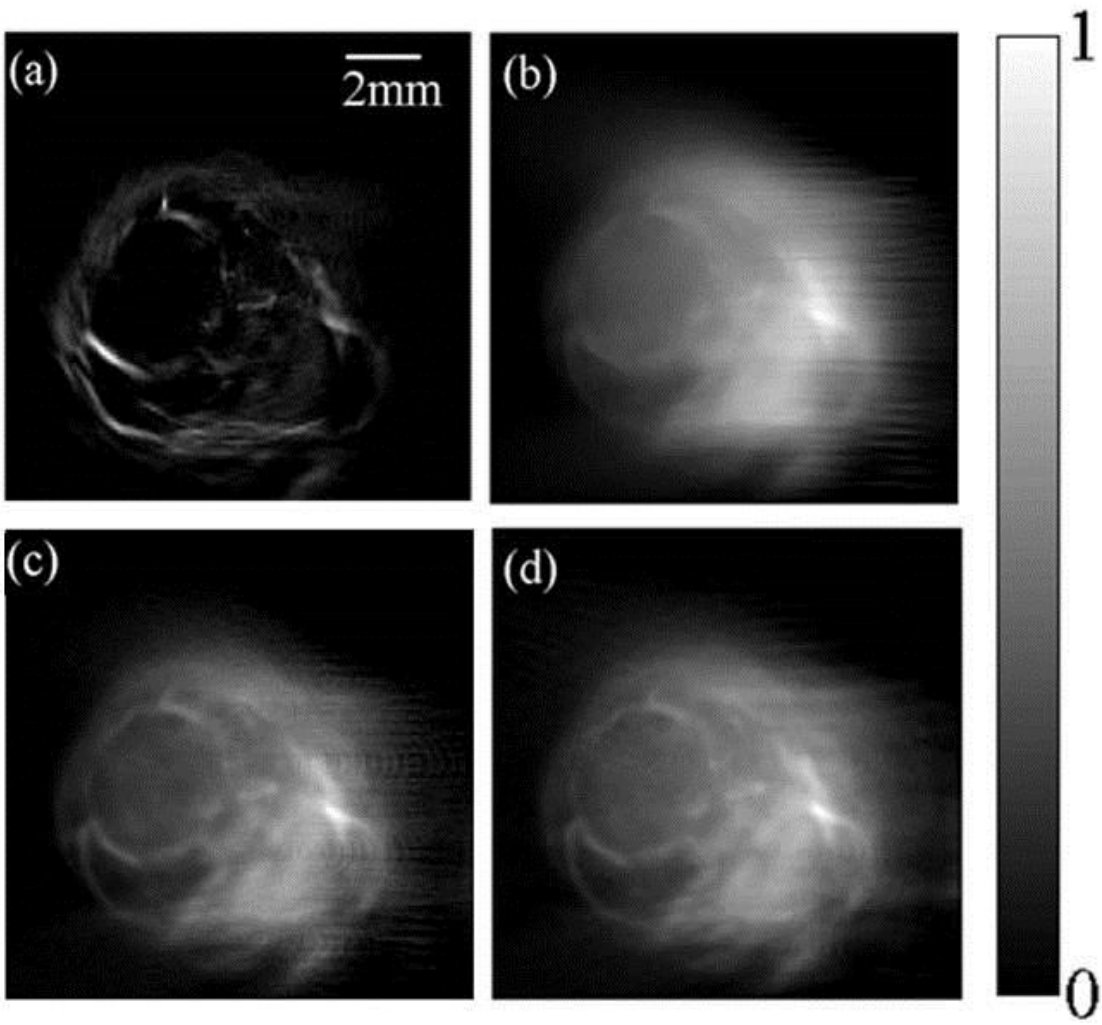

Figure 3.13 Optoacoustic reconstructions of a mouse brain from limited-view (180º) experimental data using (a) BP, (b) IMMI, (c) IMMI-FAD and (d) GWP-IMMI-FAD. (taken from [26])

3.8 Discussion

Model-based optoacoustic reconstruction algorithms offer a promising alternative to conventional back-projection formulae because they can be adapted to arbitrary tomographic geometries. In the case of large-area detectors that are flat along one of their lateral axes, accurate modeling of the detector geometry can improve image fidelity and resolution. However, this involves computationally costly model-based inversion, making it unsuitable for high-throughput imaging. This limitation is particularly severe when detector area is large because modeling such a detector requires a substantially larger matrix.

In this chapter we develop GWP-IMMI-FAD, which is the generalization of the WP framework to finite-aperture detectors. Under the WP framework, the image is divided into a set of spatial frequency bands that are individually reconstructed from only a fraction of the projection data, leading to a set of reduced model-matrices. This approach enables the use of TSVD to obtain a regularized inverse matrix to the tomographic problem. The original matrix, in the case of high-resolution images, is too large to be inverted using TSVD. Therefore, regularization requires iterative optimization algorithms, which significantly prolong processing time. One notable improvement in GWP-IMMI-FAD over the original WP framework is the introduction of a global threshold for TSVD, which allows GWP-IMMI-FAD to be applied to cases in which entire spatial frequency bands in the imaged object are difficult to reconstruct, such as in Figure 3.10(d-e).

We show that GWP-IMMI-FAD may be used not only for image reconstruction but also for system analysis. GWP-IMMI-FAD enables one to calculate the global condition number of each spatial frequency band, and thus determine the stability of its reconstruction. The use of WPs and SVD enables one to identify which spatial patterns are most difficult to reconstruct and to categorize them based on their spatial frequency. We used GWP-IMMI-FAD to analyze the dependence of reconstruction stability on detector length; we found a non-monotonic relationship in which the global condition number achieves its maximum with a detector 6 mm long. This relationship matches well with the variation in condition number of model matrix $\mathbf{M}_{\mathbf{det}}$ with detector length. We show that with SVD, reconstruction instability with a 6-mm detector is most severe at the periphery of the image (Figure 3.5). We also found that when a small spherical source is positioned at the corner of the image, the signal detected by a 6-mm detector is more low-passed than the one detected by a 20-mm detector.

Our results with GWP-IMMI-FAD show inconsistencies with previous work [60] in which the amount of smearing created by flat detectors was reported to be proportional to the aperture dimensions. The analysis in that work [60] suggests that longer detectors attenuate high frequencies in the projection data more strongly than shorter detectors, and that therefore the global condition number should scale with detector length. However, our analysis shows that a 6-mm detector attenuates high frequencies more strongly than a 20-mm detector [Figure 3.6(d)]. This apparent contradiction may be resolved by considering that the analysis in the previous

work [60] was performed for the filtered BP reconstruction algorithm, which assumes an ideal point detector. In this case, any discrepancy between the forward and inverse models leads to image distortion and possibly smearing. Indeed, although the signal generated by a 20-mm detector is sharper than the one generated by a 6-mm detector, it involves a significantly larger delay when compared to the signal detected by the point detector, as can be seen in Figure 3.6(c). Reconstruction formulae derived for the case of infinitely long line detectors [61] are also inconsistent with the previous work based on point detectors [60].

To further validate our conclusions, we compared the reconstructions of randomly generated images obtained with several detector lengths. The reconstruction results revealed a similar behavior to those obtained by the SVD analysis of GWP-IMMI-FAD. The highest reconstruction error was obtained for a 4-mm detector. This differs from the results obtained from SVD analysis, reflecting the fact that SVD considers all possible images, whereas the randomly generated images represent only a small portion of all possible images. The similar trends obtained in Figure 3.5(e-f) and Figure 3.7(b-c) suggest that the analysis described here is valid. Further validation comes from the bias-variance curves in Figure 3.7(d), which show that the variance associated with stability and noise amplification exhibits similar non-monotonic behavior as the condition number prediction in Figure 3.5(e-f) and the results in Figure 3.7(b-c). The condition numbers and reconstruction errors depend on the resolution specified by the grid on which the image is represented: increasing the grid resolution should strengthen the effect of detector length on the condition number of the matrices describing the system.

We showcased the potential of GWP-IMMI-FAD for image reconstruction using simulated and experimental optoacoustic data under conditions of full- and limited-view tomography. In all examples, the model matrix was too large for TSVD, so Tikhonov regularization was used instead. In contrast, the reduced matrices in the wavelet packet decomposition were small enough to perform TSVD. In the case of full-view simulated and experimental data, GWP-IMMI-FAD reconstruction quality was similar to the quality of Tikhonov regularization IMMI-FAD reconstruction. In the case of limited-view simulated data, GWP-IMMI-FAD performed slightly worse than Tikhonov regularization IMMI-FAD. However, in the case of limited-view experimental data, GWP-IMMI-FAD reconstruction suppressed stripe artifacts better. In all the

examples studied, GWP-IMMI-FAD completed the reconstruction more than 10-fold faster than IMMI-FAD.

The performance demonstrated in this chapter may prove useful for high-throughput optoacoustic imaging studies, which can require the reconstruction of thousands of cross-sectional images. Moreover, the results suggest that the WP framework is not restricted to ideal imaging scenarios, but that it can be generalized to manage the effects of finite-size aperture and limited-view tomography. Further generalization may be achieved by applying this framework to geometries employing focused detectors as well as to 3D reconstruction problems, where the need for faster model-based reconstructions is even greater. GWP-IMMI-FAD may be useful for designing optoacoustic systems; for example, it has already demonstrated, for the first time, that beyond a certain length of finite-aperture detector, further increases in length may lead not only to stronger optoacoustic signals, but also to stabler reconstructions.

4 Sparsity-based acoustic inversion in cross-sectional multi-scale optoacoustic imaging

With recent advancements in hardware of optoacoustic imaging systems, highly detailed cross-sectional images may be acquired with a single laser pulse, thus eliminating motion artifacts. Nonetheless, other sources of artifacts remain due to signal distortion or out-of-plane signals. The purpose of image reconstruction algorithms is to obtain the most accurate images from noisy, distorted projection data. In this chapter, we use the model-based approach for acoustic inversion, combined with a sparsity-based inversion procedure. Specifically, a cost function is used that includes the L1 norm of the image in sparse representation and a total variation (TV) term. The optimization problem is solved by a numerically efficient implementation of a non-linear gradient descent algorithm. TV-L1 model-based inversion is tested in the cross-sectional geometry for simulated data as well as for *in vivo* experimental data from an adult mouse. In all cases, model-based TV-L1 inversion showed better performance over the conventional Tikhonov regularization, TV and L1 inversion. In the numerical examples, the images reconstructed with TV-L1 inversion were quantitatively more similar to the original images. In the experimental examples, TV-L1 inversion yielded sharper images and weaker streak artifacts. The results herein show that TV-L1 inversion is capable of improving the quality of highly detailed, multi-scale optoacoustic images obtained *in vivo* using cross-sectional imaging systems. As a result of its high fidelity, model-based TV-L1 inversion may be considered the new standard for image reconstruction in cross-sectional imaging.

Some of the material in this chapter has been presented in the following publication in a very similar or identical form to the text in this chapter:

“Sparsity-based acoustic inversion in cross-sectional multi-scale optoacoustic imaging” by Yiyong Han, Stratis Tzoumas, Antonio Nunes, Vasilis Ntziachristos, Amir Rosenthal, *Medical Physics*, 42(9), 5444-5452, 2015.

4.1 Introduction

In OAT, excitation usually involves short, high-power laser pulses that lead to the generation of outward propagating acoustic waves, measured over a surface that encompasses the imaged object [10]. Ideally, the detection surface should completely surround the illuminated region. In practice, this requirement necessitates scanning an ultrasound array around the specimen, leading to long imaging durations [29], [62]. An alternative approach is the use of circular detection arrays cylindrically focused to the plane of interest. By simultaneously reading out all the detection channels, a 2D cross-sectional optoacoustic image may be formed from a single laser pulse. This characteristic enables video-rate imaging free of motion artifacts. Recent improvements in cross-sectional OAT hardware now enables the capture of highly detailed 2D images, which exhibit features at several scales.

Optoacoustic images are formed from the detected acoustic waves or projection data by using tomographic reconstruction algorithms [10]. Such algorithms are usually based on either closed-form solutions in the time or frequency domain or on a model-based approach in which the relation between the optoacoustic image and measured data is discretized in the form of a matrix relation. Model-based image reconstruction is performed by inverting the matrix relation. The advantage of the model-based approach is that it can incorporate arbitrary detection geometries for which no exact closed-form solution exists. In particular, model-based image reconstruction has been demonstrated for reducing image distortion and artifacts due to finite detector aperture or incomplete projection data.

Quite often, regularization is required in model-based inversion to suppress noise and artifacts in the reconstructed images by making assumptions on the nature of the expected optoacoustic image. Usually the regularization approaches used, e.g. Tikhonov regularization, penalize the energy of the reconstructed image. These approaches suppress noise and artifacts, but sometimes at the cost of image blurring. More recent regularization approaches are based on either

penalizing the TV term in the image or enforcing sparsity via an alternative representation, e.g. a wavelet basis. Both regularization approaches have been shown to produce sharper, cleaner images than energy-minimization regularization in several imaging scenarios, and their combination has been used in image denoising. Nonetheless, demonstration on experimental data has been limited to tissue-mimicking phantoms or experiments in mice that focused on imaging vascularization. In both cases, the structures visualized were relatively simple and were mostly dominated by a few small-scale features, which are inherently favored by sparsity and TV constraints. In many applications, cross-sectional optoacoustic images exhibit a rich structure that cannot be reconstructed so well under such constraints.

In this chapter, we study the performance of the combination of TV- and sparsity-based regularization strategies in cross-sectional multi-scale optoacoustic imaging. Image reconstruction is performed for both highly detailed numerical phantoms and cross-sectional images of an adult mouse obtained *in vivo*. In both cases, the reconstruction algorithm is tested in the full- and limited-view scenarios and compared to model-based reconstructions obtained using Tikhonov regularization, TV and L1 inversion.

The rest of the chapter is organized as follows. In section 4.2, we introduce the cross-sectional optoacoustic imaging system used in this chapter. Section 4.3 reviews the model-based reconstruction framework with the various regularization methods. Section 4.4 discusses the regularization strategies used in our work and the details of the experimental and simulation studies. The results of simulations and experiments are presented in section 4.5 and section 4.6, and are evaluated in section 4.7. Finally the discussion and conclusions are given in section 4.8.

4.2 2D optoacoustic imaging system with curved focused array

The 2D sparsity-based reconstruction in this chapter is proposed for the cross-sectional system previously described [63] (Figure 4.1). Briefly, a tunable OPO pumped by a ND:YAG laser (Opotek Inc., Carlsbad, CA) was employed with energy of up to 20 mJ/cm^2, wavelengths from 680 nm to 980 nm, pulse duration of 8 ns, and a pulse repetition rate of 10 Hz. All data were acquired after excitation at the single wavelength of 900 nm. A 10-arm fiber bundle was used to provide uniform light-sheet illumination in the imaged plane with a width of 8 mm. A custom-

made, 256-element, cylindrically focused array of immersion PZT transducers (Imasonic S.A., France) with a central frequency of 5 MHz and a focal length of 40.5 mm was employed to collect the optoacoustic signals, which were amplified and digitalized with a custom-made data-acquisition system at a sampling rate of 40 mega samples/s. The detector array offers a 270-degree angular coverage in a given slice of focus. The imaged object was submerged in a water tank in a horizontal position in a holder. The transducer ring was translated using a linear stage (IAI Industrieroboter, Schwalbach, Germany) to enable imaging of multiple transverse slices. Each of the signals was averaged 20 times and band-pass filtered with the cut-off frequencies of 0.05 MHz and 7 MHz, which cover the frequency band of the transducer.

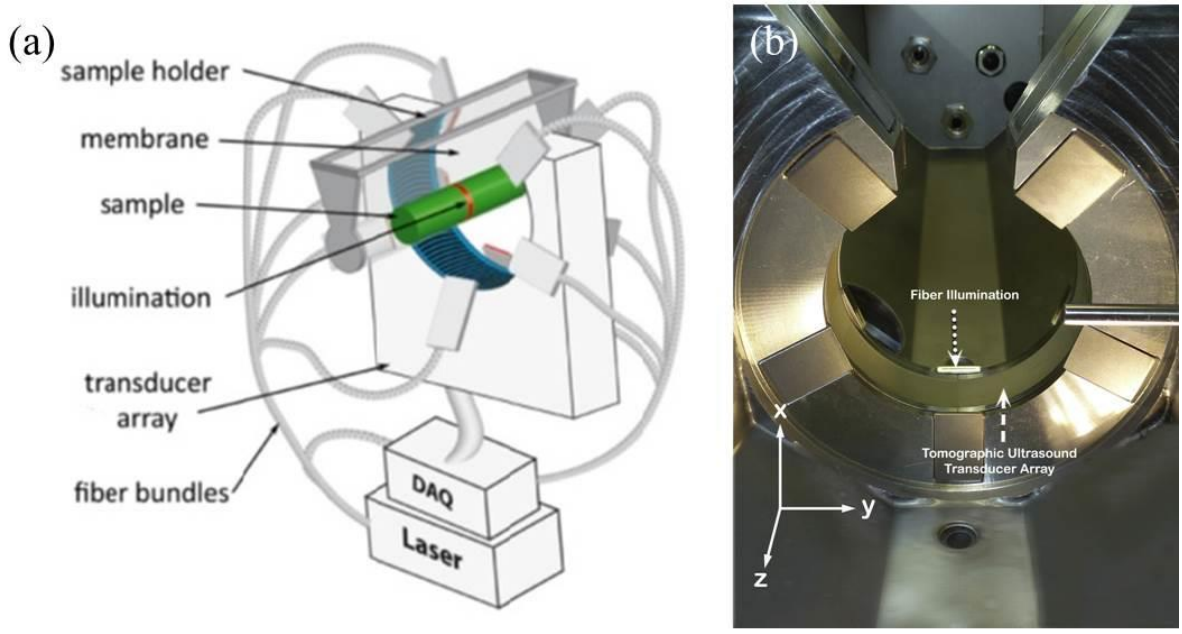

Figure 4.1 2D optoacoustic imaging system setup. (a) The schematic of the optoacoustic imaging system setup. (b) Illumination and detection geometry in the imaging chamber. The transducer can be translated along the z-axis in order to acquire multiple transverse cross sections in the x–y plane. (taken from [64])

4.3 Theoretical background

The 2D model-based algorithm in section 2.2.3 leads to the following matrix relation [24]:

$$\mathbf{p} = \mathbf{M}_{2D}\,\mathbf{z}, \tag{4.1}$$

where $\mathbf{p}$ is a column vector representing the measurement data, $\mathbf{z}$ is a column vector representing the unknown reconstruction image and $\mathbf{M}_{2D}$ is the forward model matrix. For a given optoacoustic imaging system, the model matrix $\mathbf{M}_{2D}$ depends solely on the image grid and the measurement geometry.

4.3.1 Tikhonov regularization with Laplacian operation

When regularization is required, e.g. in the case of insufficient projection data, Tikhonov regularization in section 2.4.2 is often used [59]:

$$\underset{\mathbf{z}}{\operatorname{argmin}} \left\{ \left\| \mathbf{p} - \mathbf{M}_{2D}\mathbf{z} \right\|_2^2 + \lambda \left\| \mathbf{L}\mathbf{z} \right\|_2^2 \right\} , \tag{4.2}$$

where $\lambda > 0$ is the regularization parameter and $\mathbf{L}$ is the regularization operator. In this chapter, a quadratic smoothness Laplacian penalty term is used [38]:

$$\left\| \mathbf{L}\mathbf{z} \right\|_2^2 = \sum_{n=1}^{N} (4\mathbf{z}_{(x,y)}^n - \mathbf{z}_{(x-1,y)}^n - \mathbf{z}_{(x,y+1)}^n - \mathbf{z}_{(x,y-1)}^n - \mathbf{z}_{(x+1,y)}^n)^2 . \tag{4.3}$$

where N is the total pixel number of the image $\mathbf{z}$ and $\mathbf{z}_{(x,y)}^n$ is the intensity of the nth pixel at the position of (x, y). Tikhonov regularization with a Laplacian penalty (Tik-Lap) may be efficiently performed using the LSQR algorithm.

4.3.2 L1 regularization

The application of L1 regularization for inverting Eq. (4.1) is based on the common assumption that the reconstructed image may be sparsely represented in an alternative basis [36], [65]–[68]. To perform the inversion, the following procedure is applied. First, the image to be recovered u is transferred into a basis in which it is expected to be sparse: $x = \mathbf{\Phi}\mathbf{z}$, where x is the representation of $\mathbf{z}$ in the new domain and $\mathbf{\Phi}$ is the transform matrix. Generally, a unitary $\mathbf{\Phi}$ would be preferable, which represents a transformation to an orthonormal basis. In this chapter, $\mathbf{\Phi}$ was chosen to represent a three-level Daubechies 4 wavelet transform. L1 regularization can then be described by solving the following problem:

$$\underset{\mathbf{z}}{\operatorname{argmin}}\left\{\left\|\mathbf{p}-\mathbf{M}_{2D}\mathbf{z}\right\|_2^2+\mu\left\|\mathbf{\Phi z}\right\|_1\right\}, \tag{4.4}$$

where $\mu>0$ is the regularization parameter.

We calculate the L1 norm and its derivative as following. The L1 norm is the sum of absolute values. Let $\mathbf{u}=\mathbf{\Phi z}$ and we can approximate the absolute value of $\mathbf{u}$ as $\sqrt{\mathbf{u}^{\mathrm{T}}\mathbf{u}+\sigma}$, where σ is a small positive constant. And we can get the derivative $\frac{d\left\|\mathbf{u}\right\|_1}{d\mathbf{u}}\approx\frac{\mathbf{u}}{\sqrt{\mathbf{u}^{\mathrm{T}}\mathbf{u}+\sigma}}$ [69].

4.3.3 TV regularization

TV regularization is used for the suppression of noise [70] as well as streak artifacts [71][38], [72]–[74]. The scheme has the following expression:

$$\underset{\mathbf{z}}{\operatorname{argmin}}\left\{\left\|\mathbf{p}-\mathbf{M}_{2D}\mathbf{z}\right\|_2^2+\alpha\left|\mathbf{z}\right|_{\mathrm{TV}}\right\}, \tag{4.5}$$

where $\alpha>0$ is the regularization parameter. And the TV norm is defined as

$$\left|\mathbf{z}\right|_{\mathrm{TV}}=\sum_{i,j}\sqrt{\left|\nabla_x\mathbf{z}(i,j)\right|^2+\left|\nabla_y\mathbf{z}(i,j)\right|^2}, \tag{4.6}$$

where ∇_x and ∇_y represent the finite differences of the image along x and y directions.

4.4 Combined TV-L1 sparsity-based reconstruction

Here we demonstrate the use of combined TV-L1 regularization for image reconstruction in cross-sectional optoacoustic imaging. Image reconstruction is performed by solving the following problem:

$$\underset{\mathbf{z}}{\operatorname{argmin}}\ \boldsymbol{f}(\mathbf{z})=\underset{\mathbf{z}}{\operatorname{argmin}}\left\{\left\|\mathbf{p}-\mathbf{M}_{2D}\mathbf{z}\right\|_2^2+\lambda_1\left|\mathbf{z}\right|_{\mathrm{TV}}+\lambda_2\left\|\mathbf{\Phi z}\right\|_1\right\}. \tag{4.7}$$

The two regularization parameters $\lambda_1 \geq 0$ and $\lambda_2 \geq 0$ determine the respective influence of the TV and L1 regularization terms. To solve the unconstrained convex minimization problem in Eq. (4.7), Algorithm 4.1 is used with a gradient descent algorithm via backtracking line search [75].

Algorithm 4.1 Model-based TV-L1 reconstruction using gradient descent

Inputs: $\mathbf{p}$, $\mathbf{M}_{2D}$, $\boldsymbol{\Phi}$, λ_1, λ_2, η, max*Iter*

Output: $\mathbf{z}$

Step 1: Initialize a starting point $\mathbf{z} = 0$, iteration variable $i = 1$.

Step 2: Calculate the gradient of the cost function $\nabla \boldsymbol{f}(\mathbf{z})$ and the update part of solution $\Delta \mathbf{z} = -\nabla \boldsymbol{f}(\mathbf{z})$.

Step 3: Choose step size t via backtracking line search.

Step 4: Update the solution with $\mathbf{z}_{i+1} = \mathbf{z}_i + t\Delta \mathbf{z}$.

Step 5: Check the stopping criterion. If $\left(\left(\left\| \mathbf{p} - \mathbf{M}_{2D}\mathbf{z}_{i+1} \right\|_2 - \left\| \mathbf{p} - \mathbf{M}_{2D}\mathbf{z}_i \right\|_2 \right) / \left\| \mathbf{p} \right\|_2 \right) < \eta$ or $i > \max Iter$, finish; otherwise, $i = i + 1$ and go to Step2.

4.5 Simulations

All inversions were implemented in Matlab (Mathworks, Natick, MA) and executed on a desktop computer with an Intel Core2 Quad Processor CPU operating at 2.67 GHz with 16 GB of RAM. The results of TV-L1 method were compared with reconstructions obtained using Tik-Lap method in section 4.3.1, L1 method in section 4.3.2 and TV method in section 4.3.3. Consistent with the experimental system, a circular detection geometry with a radius of 40.5 mm was assumed, for which 256 projections were calculated over a coverage angle of 270 degrees or 128 projections were calculated over 135 degrees (Figure 4.2). A numerical 2D phantom of a mouse cross-section (Figure 3.8) served as the original image with a size of 2.5 cm × 2.5 cm and 512 × 512 pixels. Projection data were calculated using a 600 × 600 mesh. In all reconstructions, white

Gaussian noise was added to the projection data with a signal-to-noise ratio (SNR) of 10 dB. In all reconstruction algorithms, the stopping criterion was $\eta = 1\times10^{-4}$ and $\max Iter = 200$.

Image reconstructions were performed based on the above simulation settings for the two detection geometries in Figure 4.2. Figure 4.3 shows the reconstruction results in the nearly full-view scenario. Four reconstructions in Figure 4.3(a-d) were obtained, respectively, using Tik-Lap, TV, L1 and TV-L1. All four reconstructions show good quality with marginal variation from the original image. Figure 4.4(a-d) shows the corresponding reconstructions in the limited-view scenario. Qualitative differences among the images are more readily observed; for example, TV-L1 produces weaker negative artifacts and less spurious noise-like texture than the other reconstruction approaches. The reconstructions are compared quantitatively in section 4.7.

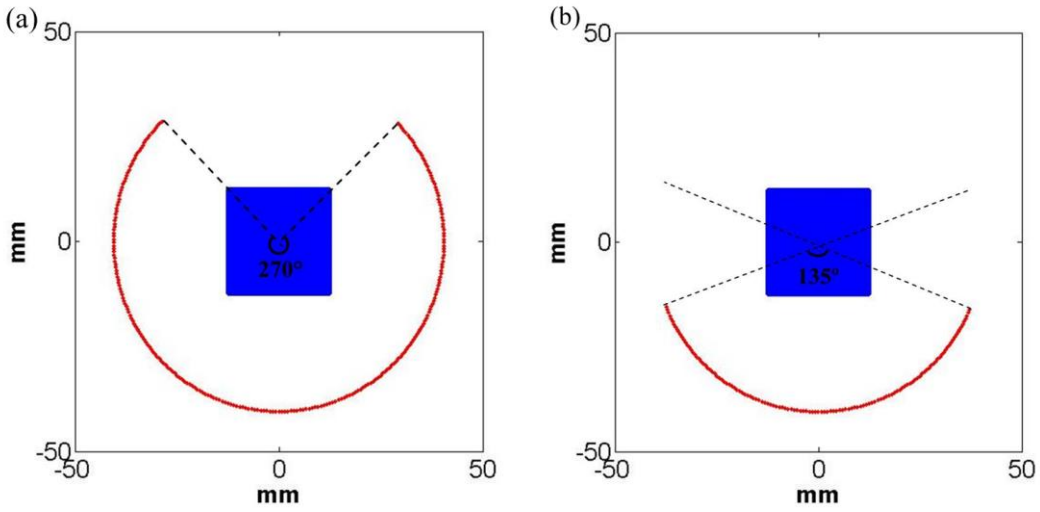

Figure 4.2 Detection geometries in the simulation and experiment in (a) nearly full-view and (b) limited-view. (taken from [64])

4.6 Experiments

An experimental dataset acquired from a mouse in the hind-limb area *in vivo* using the system described in section 4.2 was reconstructed using the various algorithms. The dimensions of all reconstruction images were 2.5 cm × 2.5 cm on a grid of 512 × 512 pixels.

In the first example, we present the results obtained for the nearly full-view imaging geometry (Figure 4.2(a)). Four reconstructions in Figure 4.5(a-d) were obtained using Tik-Lap, TV, L1 and TV-L1, respectively. Figure 4.5(e)-(h) show a magnification of the image in the yellow region of Figure 4.5(a)-(d). The reconstruction obtained using TV-L1 is sharper and has weaker streak artifacts and less noise than the other three reconstructions. Figure 4.5(i) shows the full-width-at-half-maximum (FWHM) of the blood vessel taken over the dashed lines in Figure 4.5(e)-(h): 361 µm for Tik-Lap, 300 µm for TV, 295 µm for L1 and 308 µm for TV-L1. Applying L1 sharpens the blood vessel, while the additional application of TV suppresses spurious noise-like texture.

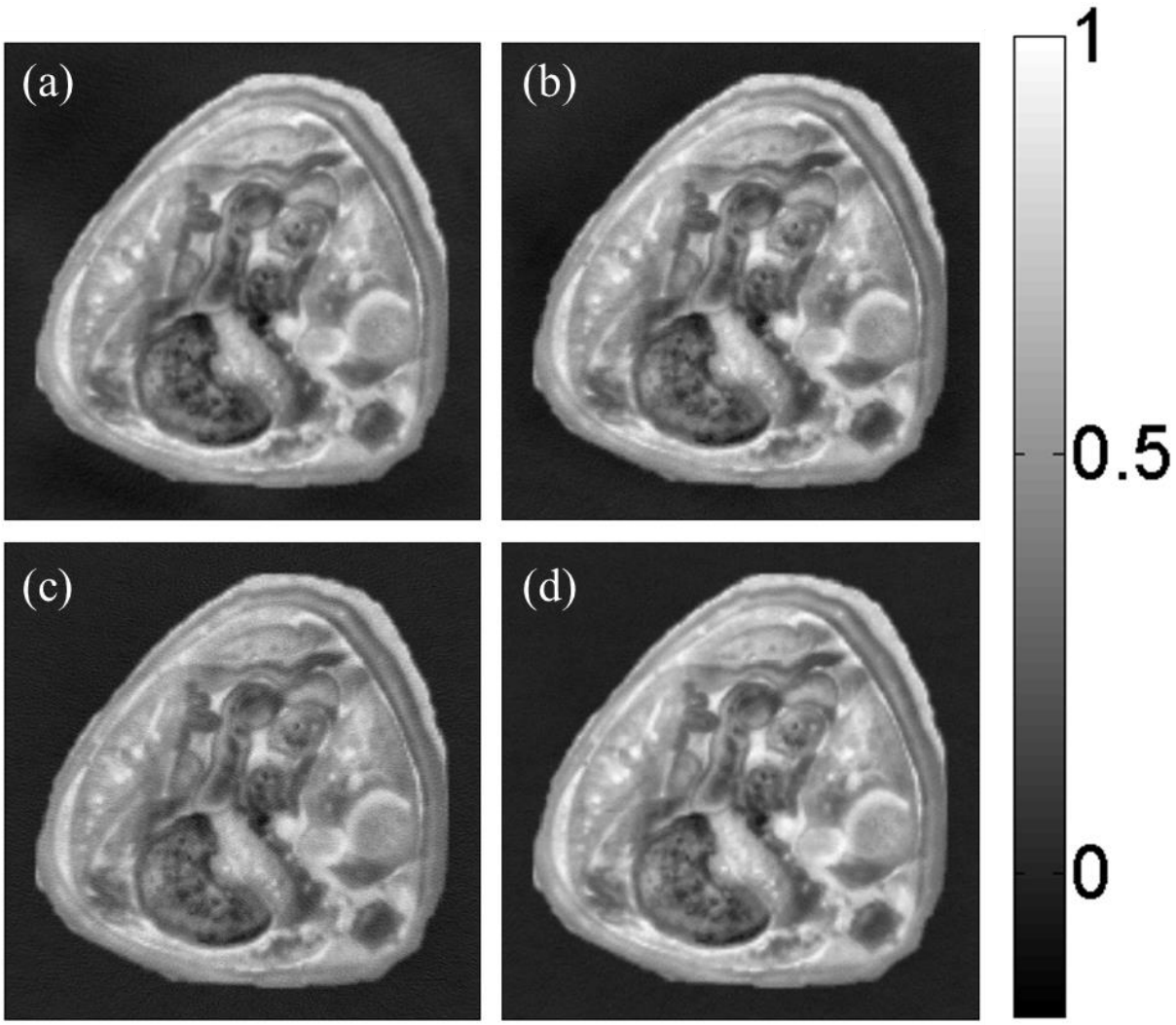

Figure 4.3 Simulation reconstructions in nearly full-view performed using (a) Tik-Lap, (b) TV, (c) L1 and (d) TV-L1. (taken from [64])

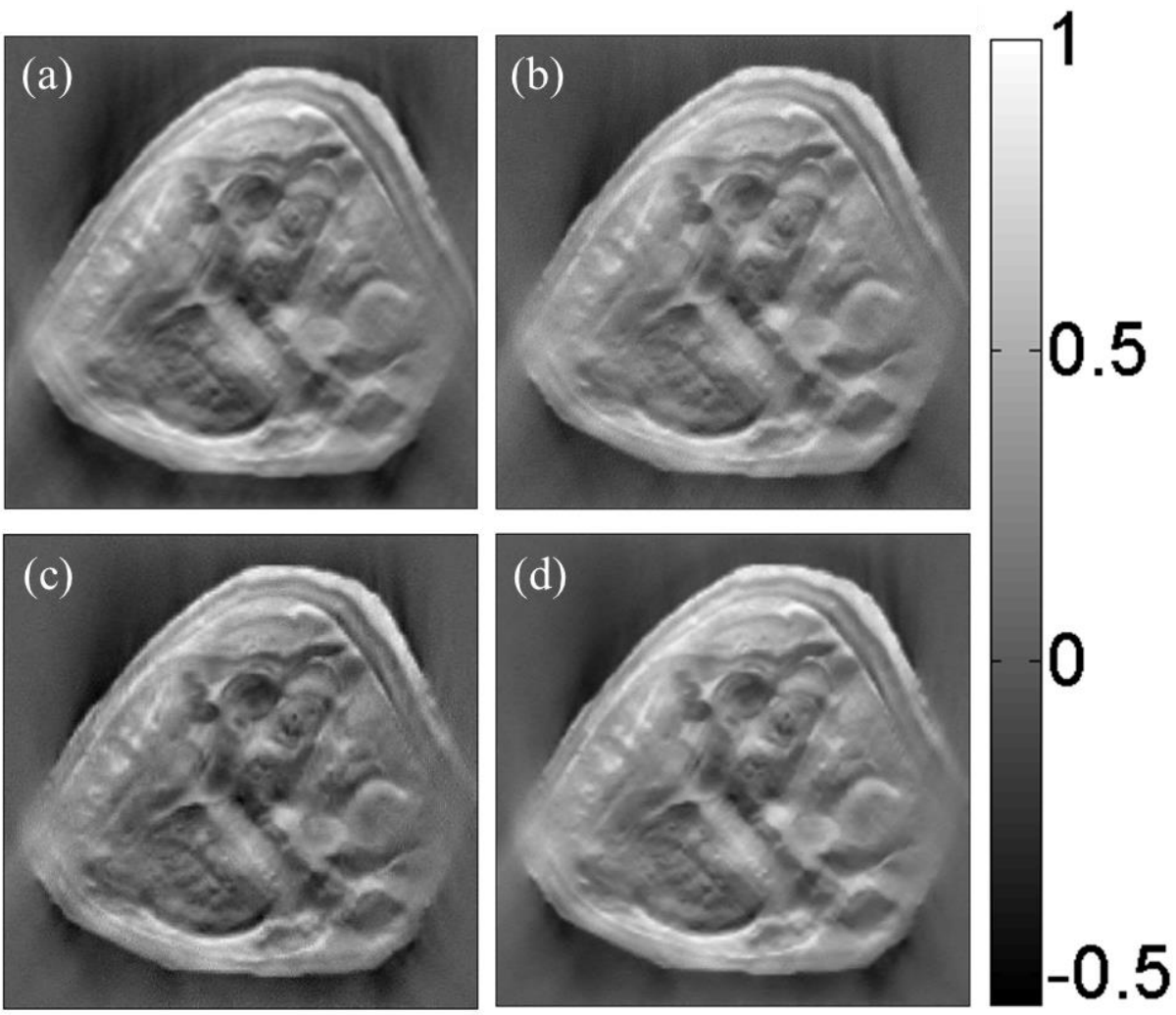

Figure 4.4 Simulation reconstructions in limited-view performed using (a) Tik-Lap, (b) TV, (c) L1 and (d) TV-L1. (taken from [64])

Next we analyzed the case of limited-view imaging geometry (Figure 4.2(b)), for which we generated the dataset by discarding half the projection data. Comparison of the four reconstructions [Figure 4.6(a-d)] shows that, as in the nearly full-view case, TV-L1 gives a sharper image with weaker streak artifacts. The reconstructions are compared quantitatively in section 4.7.

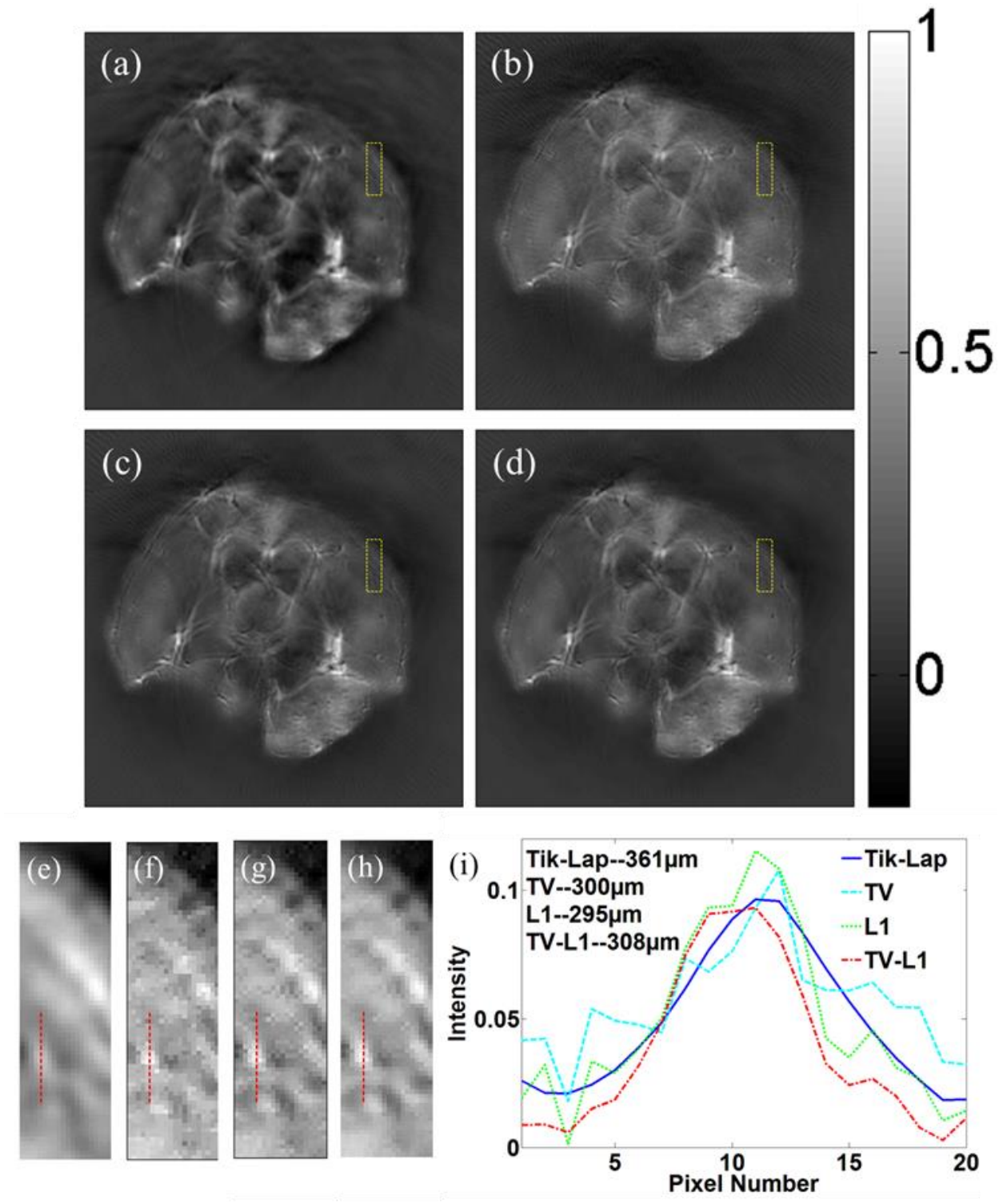

Figure 4.5 Reconstructed cross-sectional mouse images obtained from nearly full-view projection data using (a) Tik-Lap, (b) TV, (c) L1 and (d) TV-L1. Yellow regions in panels (a)-(d) are shown as zoomed images in panels (e)-(h). The FWHM values of the vessel along the dashed line in panels (e)-(h) are compared in panel (i). (taken from [64])

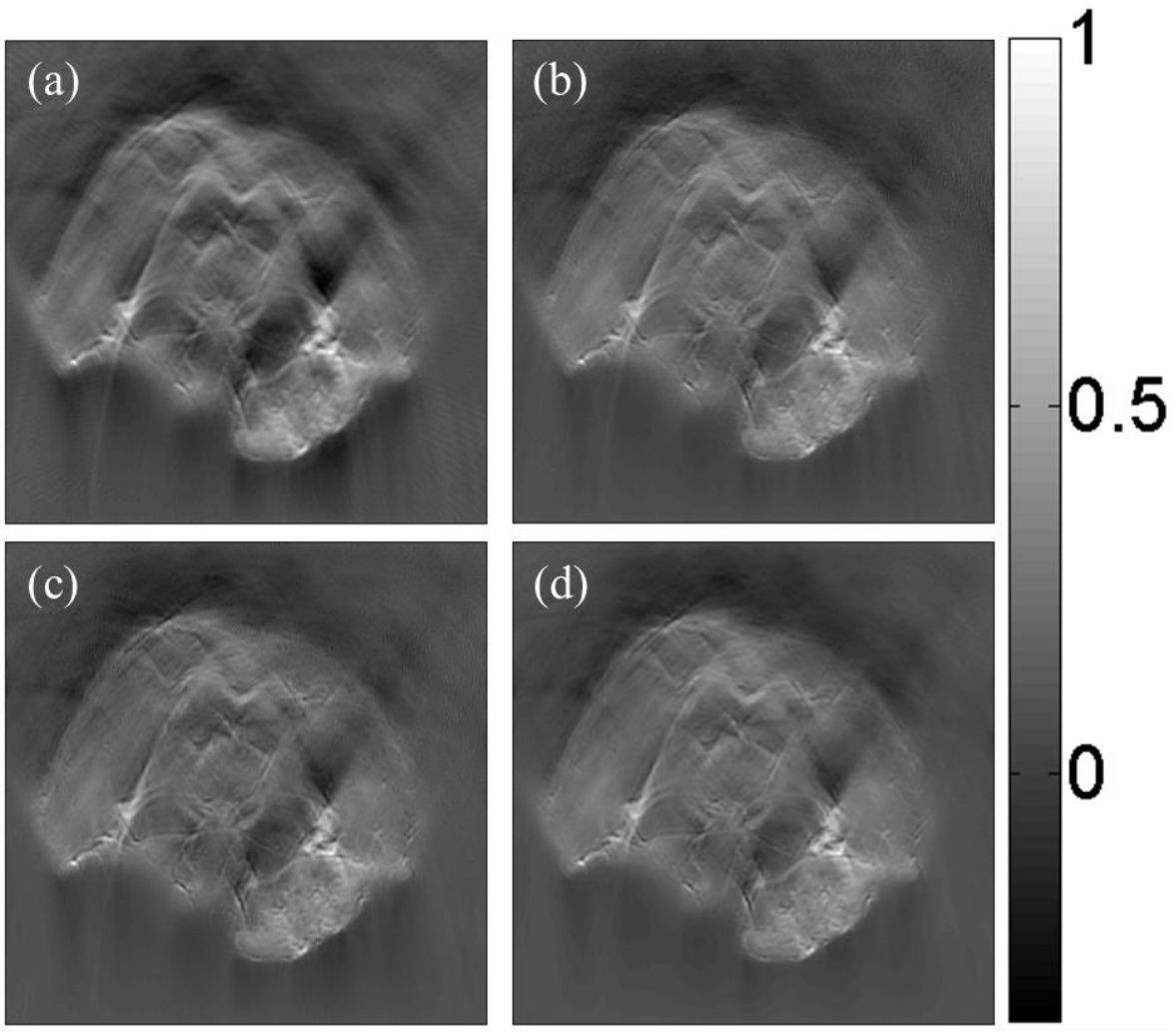

Figure 4.6 Reconstructed cross-sectional mouse images obtained from limited-view projection data using (a) Tik-Lap, (b) TV, (c) L1 and (d) TV-L1. (taken from [64])

4.7 Evaluation

The regularization parameters used for the simulations and experiments are listed in Table 4.1. To obtain a fair comparison, the same stopping criterion was used in all reconstructions, including Tik-Lap. The iteration number and the reconstruction time for each case are shown in Table 4.2.

Table 4.1 Regularization parameters used during reconstructions. (taken from [64])

		Tik-Lap	TV	L1	TV-L1	
		λ	μ	α	λ_1	λ_2
Simulation	Full view	1×10^6	4×10^5	2×10^5	4×10^5	2×10^5
	Limited view	3×10^6	6×10^5	1×10^6	6×10^5	1×10^6
Experimental	Full view	9×10^6	1×10^5	5×10^5	1×10^5	5×10^5
	Limited view	1×10^7	1×10^5	6×10^5	1×10^5	6×10^5

Table 4.2 Iteration number and processing time for reconstructions. (taken from [64])

Dataset	Geometry	Iteration number				Reconstruction time [s]			
		Tik-Lap	TV	L1	TV-L1	Tik-Lap	TV	L1	TV-L1
Simulation	Full view	51	98	101	100	130	467	479	487
	Limited view	80	132	129	131	100	398	401	406
Experimental	Full view	49	80	82	81	105	379	392	400
	Limited view	76	122	119	120	86	359	360	367

Table 4.3 Quantitative evaluation of reconstructions. (taken from [64])

Dataset	Geometry	Quality parameter	Tik-Lap	TV	L1	TV-L1
Simulation	Full view	RMSD	0.0528	0.0463	0.0672	0.0393
		SNR	23.46	24.40	23.52	26.41
		CNR	16.73	17.31	13.44	20.49
	Limited view	RMSD	0.2452	0.2281	0.2626	0.2218
		SNR	7.01	9.26	7.91	9.74
		CNR	2.90	3.31	2.66	3.80
Experiment	Full view	SNR	7.37	8.44	8.68	8.82
		CNR	2.94	4.55	4.36	4.89
	Limited view	SNR	5.30	5.20	5.34	5.77
		CNR	2.35	3.00	2.62	3.16

Quantitative analysis comparing the reconstructions involved three metrics (Table 4.3). RMSD calculates the difference between the reconstructed images and the original image in the simulations. The other two metrics, SNR and contrast-to-noise ratio (CNR), were analyzed because the original image in the experimental data was unknown. In all cases, the target region was the entire mouse body part, and the surrounding area was defined as background. RMSD is defined as

$$RMSD = \sqrt{\frac{1}{N}\sum_{n=1}^{N}\left\|u_1^n - u_2^n\right\|^2} \quad , \tag{4.8}$$

where u_1^n and u_2^n are the nth pixel value of the two images u_1 and u_2, and N is the total pixel number of the image. SNR is defined as

$$SNR_{dB} = 20\,\mathbf{log}_{10}\left(\frac{A^{(t)}}{A^{(b)}}\right), \tag{4.9}$$

where $A^{(t)}$ and $A^{(b)}$ are the root-mean-square amplitudes of the target and background regions. CNR is defined as

$$CNR = \frac{\left|\bar{u}^{(t)} - \bar{u}^{(b)}\right|}{\sigma^{(b)}}, \tag{4.10}$$

where $\bar{u}^{(t)}$ and $\bar{u}^{(b)}$ are the mean values for the target and background regions, and $\sigma^{(b)}$ is the variance in the background region.

4.8 Discussion and conclusion

In this chapter we show that a model-based approach combined with a sparsity-based inversion scheme can significantly enhance multi-scale cross-sectional optoacoustic images. The inversion algorithm combines TV and L1 cost functions, and relies on a sparse representation of the reconstructed images in an alternative basis (e.g wavelets). Previous work has shown that this approach can reduce projection density while preserving image quality in the case of vasculature imaging. Such images contain relatively simple structures on a single scale. The current work demonstrates the usefulness of sparsity-based inversion for highly detailed, multi-scale images.

Here, a few points are worth noticing during the reconstruction process to achieve good results. First, in the optimization process of the TV-L1 method with gradient descent, two regularization parameters $\lambda_1 \geq 0$ and $\lambda_2 \geq 0$—representing the weight of TV term and L1 term regularization item, respectively—need to be determined appropriately. Over-regularization in the TV term may lead to cartoon-like images lacking texture; over-regularization in the L1 term may lead to image distortions common in lossy image compression (compression artifacts). On the other hand, if their proportions to the objective function are too small, their support would become

weak. Unfortunately, until now, there is no general method to effectively compute the optimal values of two regularization parameters. In our simulations and experiments in this chapter, the regularization parameters of TV-L1 in Table 4.1 are determined by manually trying with different combinations and choosing the best one. The regularization parameters of TV method or L1 method are the same as the same as the corresponding term of TV-L1 method. This comparison way is only to show the advantage of TV-L1 framework can combine TV method and L1 method. Setting one of the regularization parameters in TV-L1 method as zero will turn TV-L1 method as TV method or L1 method. Secondly, several other issues may also affect the reconstructed image quality, including the line search method determining the step size to update the reconstruction in each iteration, the sparsity of the true reconstruction, and the choice of the sparse transform method.

TV-L1 inversion was tested for numerically simulated as well as experimental data in cross-sectional imaging geometries with 270º and 135º angular coverage. The results were compared to Tik-Lap inversion, TV inversion and L1 inversion with quantitative metrics shown in Table 4.3. In the numerical simulations, TV-L1 yielded images with lower RMSD and higher SNR and CNR with respect to the original image than did Tik-Lap methods. In the reconstructions from experimental data, TV-L1 led to sharper images with weaker streak artifacts than the other three methods. At the same time, TV-L1 took 3- to 4-fold longer than Tik-Lap with all simulated and experimental datasets as shown in Table 4.2.

In summary, the results obtained in this chapter indicate that TV-L1 is a useful tool for enhancing detailed, multi-scale cross-sectional images. TV-L1 does take longer than Tik-Lap, but the reconstruction time remains acceptable, especially in light of the high resolution of the reconstructed 2D images. Reconstruction times may be improved by relaxing the stopping criterion, or preferably by executing the algorithm on a graphics processing unit.

5 Three-dimensional optoacoustic reconstruction using fast sparse representation

Optoacoustic tomography based on insufficient spatial sampling of ultrasound waves leads to loss of contrast and artifacts on the reconstructed images. Compared to reconstructions based on L2-norm regularization, sparsity-based reconstructions may improve contrast and reduce image artifacts but at a high computational cost, which has so far limited their use to 2D optoacoustic tomography as shown in chapter 4. In this chapter, a fast sparsity-based reconstruction algorithm is proposed for 3D optoacoustic tomography, based on gradient descent with Barzilai-Borwein line search (L1-GDBB). Using simulations and experiments, we show that L1-GDBB offers 4-fold faster reconstruction than previously reported L1-norm regularized reconstruction based on gradient descent with backtracking line search. Moreover, the new algorithm provides higher-quality images with fewer artifacts than non-sparsity-based L2-norm regularized reconstruction and back-projection reconstruction.

Some of the material in this chapter has been presented in the following publication in a very similar or identical form to the text in this chapter:

"Three-dimensional Optoacoustic reconstruction using fast sparse representation" by Yiyong Han, Lu Ding, Xose Luis Dean Ben, Daniel Razansky, Jaya Prakash, Vasilis Ntziachristos, Optics letters, Vol. 42, Issue 5, pp. 979-982 (2017)

5.1 Motivation

Tomographic reconstruction is often hampered by incomplete or insufficient data, and the selection of reconstruction algorithm can make a substantial difference in final image quality. In optoacoustic tomography, ultrasound waves are generated in a three-dimensional (3D) region and further propagate in all directions [4]. Thereby, the optoacoustic detector(s) should ideally collect sufficient pressure signals to accurately map the entire ultrasound wavefront surrounding the imaged sample [10]. However, spatial constraints in currently available optoacoustic systems usually limit the range of accessible projection angles, consequently leading to artifacts and loss of resolution and contrast in the reconstructed images. For example, it has been shown that streak-type artefacts associated with sparse acquisition are clearly visible in the cross-sections of the reconstructed 3D images when using back-projection algorithms or iterative inversion methods based on L2-norm regularization [34], [74].

Sparsity-based iterative image reconstruction algorithms using L1-norm regularization are known to mitigate artifacts and hence enhance the CNR of images [76]. In 2D optoacoustic imaging, sparsity-based reconstruction generates better images with fewer artifacts [36], [77] than reconstruction based on the LSQR algorithm with L2-norm regularization (L2-LSQR) [64], [67]. Typically, 2D sparsity-based reconstruction with L1-norm regularization is carried out based on gradient descent with backtracking line search (L1-GDBT) [64], [67], [77], in which the sparsity transformation is carried out using the Rice wavelet toolbox [6, 8-10]. These approaches are inadequate for 3D optoacoustic imaging. The Rice wavelet toolbox restricts the reconstructed image in 2D with a size of $2^N \times 2^N$, where N is a positive integer. However, the backtracking line search algorithm employed in L1-GDBT involves several matrix-vector multiplications at each iteration, making the entire process computationally burdensome and therefore impractical for 3D optoacoustic imaging.

As optoacoustic systems collecting 3D information become available [78], it is necessary to develop fast and accurate sparsity-based algorithms for 3D optoacoustic reconstructions. Although we have achieved real-time BP reconstruction with GPU implementation [79], a more accurate 3D model-based iterative reconstruction is still needed for better visualization and subsequent multispectral analysis [80]. With the benefit of a multi-level wavelet decomposition (and reconstruction) for 2D and 3D images of any size, we propose a fast 3D sparsity-based optoacoustic reconstruction method based on gradient descent with Barzilai-Borwein line search and L1-norm regularization (L1-GDBB). Much like L2-LSQR, L1-GDBB

requires only two matrix-vector multiplications at each iteration [81]. We hypothesized that computing the gradient step size analytically at each iteration would make L1-GDBB faster than L1-GDBT [64], [67], [77]. Here we compare the performance of BP, L1-GDBB, L2-LSQR and L1-GDBT in simulations and experiments, and we provide evidence of the advantages of L1-GDBB over the other three methods.

5.2 3D optoacoustic imaging system with spherical focused array

The 3D sparsity-based reconstruction is proposed for the 3D optoacoustic imaging system shown in Figure 5.1, which utilizes a hand-held probe design with a custom-made two-dimensional array (Imasonic SaS, Voray, France) [78]. The detecting array consists of a 256-element ultrasound transducer array (UTA) having a spherical surface with a radius of 40 mm and covering a 90°-span of projection angles. The individual transducer elements have a size of ca. 3 mm$\times$3 mm, a central frequency of 4 MHz and a -6 dB bandwidth of 100%. A tunable (690–900 nm) OPO laser (Phocus, Opotek Inc., Carlsbad, CA) is used for illumination with short laser pulses (<10 ns) and a repetition rate of 10 Hz. The pulsed laser is delivered to the object through a fiber bundle (CeramOptics GmbH, Bonn, Germany) into a hole at the center of the detection array. A transparent polyethylene membrane is used to enclose the detection surface while the volume between the membrane and the transducer surface is filled with water for acoustic coupling. Raw optoacoustic data are simultaneously sampled at 40 MHz with a custom-made data acquisition system (Falkenstein Mikrosysteme GmbH, Taufkirchen, Germany).

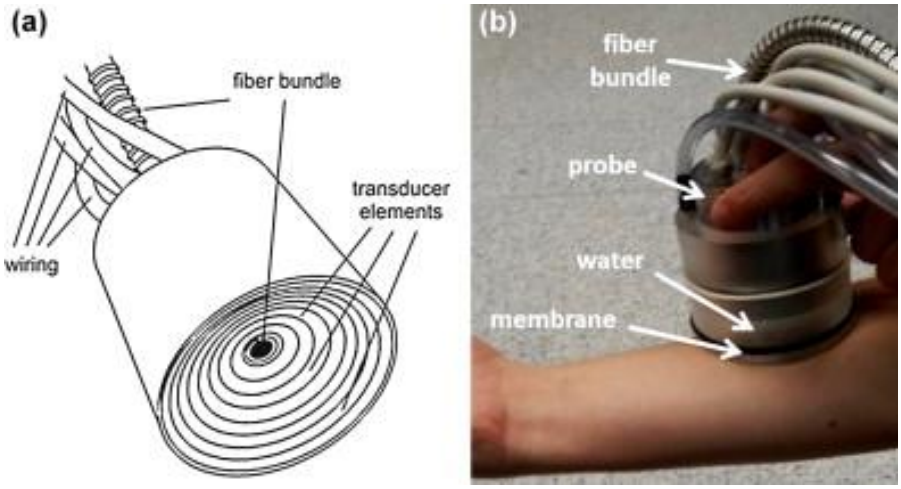

Figure 5.1 Layout and color photograph of the hand-held MSOT probe for 3D imaging. (taken from [78])

5.3 Method

In optoacoustic imaging, the simplified discretized BP implementation takes the form [79]

$$u(\mathbf{r}_j') = \sum_i [\, p(\mathbf{r}_i, t_{ij}) - t_{ij} \frac{\partial p(\mathbf{r}_i, t_{ij})}{\partial t}] \tag{5.1}$$

where $u(\mathbf{r}_j')$ is the image to be reconstructed (initial increase in pressure) at position $\mathbf{r}_j'$, $p(\mathbf{r}_i, t_{ij})$ is the optoacoustic pressure detected at point $\mathbf{r}_i$ and time $t_{ij} = |\mathbf{r}_i - \mathbf{r}_j'|/c$, and c is the speed of sound.

In 3D model-based iterative reconstruction, the forward model leads to a discrete-to-discrete linear transformation from reconstructed image $\mathbf{z}$ to the detected pressure signals $\mathbf{p}$ [34], defined by

$$\mathbf{p} = \mathbf{M}_{3D}\,\mathbf{z}\ , \tag{5.2}$$

where $\mathbf{p}$ is the optoacoustic pressure at a set of points and times, $\mathbf{M}_{3D}$ is the 3D forward model matrix and $\mathbf{z}$ is the image to be reconstructed (initial increase in pressure). The reconstructed image can be obtained by solving the following minimization problem with the L2-LSQR method [82]:

$$\underset{\mathbf{z}}{\operatorname{argmin}} \left\{ \left\| \mathbf{p} - \mathbf{M}_{3D}\mathbf{z} \right\|_2^2 + \alpha \left\| \mathbf{z} \right\|_2^2 \right\}, \mathbf{z} \geq 0, \tag{5.3}$$

where $\alpha \geq 0$ is the regularization parameter. An alternative approach to solve the inversion of Eq. (5.2) by sparse representation is [64], [67], [77]

$$\arg\min_{\mathbf{z}} f(\mathbf{z}) = \arg\min_{\mathbf{z}} \left\{ \frac{1}{2} \left\| \mathbf{p} - \mathbf{M}\mathbf{z} \right\|_2^2 + \lambda \left\| \mathbf{\Phi}\mathbf{z} \right\|_1 \right\}, \mathbf{z} \geq 0, \tag{5.4}$$

where $\lambda \geq 0$ is the regularization parameter and $\mathbf{\Phi}$ is the sparsity transform operator. If $v = \mathbf{\Phi}\mathbf{z}$ represents the solution in a sparsity domain, then Eq. (5.4) can be rewritten as

$$\arg\min_{\mathbf{z}} f(\mathbf{v}) = \arg\min_{\mathbf{z}} \left\{ \frac{1}{2} \left\| \mathbf{p} - \mathbf{H}\mathbf{v} \right\|_2^2 + \lambda \left\| \mathbf{v} \right\|_1 \right\}, \mathbf{\Phi}^{-1}\mathbf{v} \geq 0\ , \tag{5.5}$$

where $\mathbf{H} = \mathbf{M}\mathbf{\Phi}^{-1}$. Eq. (5.5) can be solved efficiently using L1-GDBB (Algorithm 5.1). In the present study, $\mathbf{\Phi}$ was defined to be the two-level Daubechies-4 wavelet transform [36], [64].

Algorithm 5.1. Sparsity-based reconstruction using gradient descent with Barzilai-Borwein line search

Step 1: Initialize iteration variables $i = 1$ and $\mathbf{v}_1 = 0$, set maximum iteration number max *Iter* and stopping criterion η.

Step 2: Calculate the gradient of the objective function $\nabla f(\mathbf{v}_i)$ and update part of the solution $\Delta(\mathbf{v}_i) = -\nabla f(\mathbf{v}_i)$.

Step 3: If $i = 1$, set $t_1 = 1$. Otherwise **c**hoose step size t_i via Barzilai-Borwein line search:

$$t_i = \left\|\mathbf{v}_i - \mathbf{v}_{i-1}\right\|_2^2 / \left(\left(\mathbf{v}_i - \mathbf{v}_{i-1}\right)^T \left(\Delta\mathbf{v}_i - \Delta\mathbf{v}_{i-1}\right)\right).$$

Step 4: Update the solution with $\mathbf{v}_{i+1} = \mathbf{\Phi}\left(\mathbf{max}\left(\mathbf{\Phi}^{-1}\left(\mathbf{v}_i + t_i\Delta\mathbf{v}_i\right), 0\right)\right)$.

Step 5: Check the stopping criterion. If $\left(\left(\left\|\mathbf{p} - \mathbf{H}\mathbf{v}_{i+1}\right\|_2 - \left\|\mathbf{p} - \mathbf{H}\mathbf{v}_i\right\|_2\right) / \left\|p\right\|_2\right) < \eta$ or $i >$ max *Iter*, go to next step; otherwise, $i = i + 1$ and go to Step 2.

Step 6: Transfer the final reconstruction back to the image domain. $\mathbf{z} = \mathbf{\Phi}^{-1}\mathbf{v}$.

L1-GDBT is similar to the L1-GDBB described in Algorithm 5.1, except that Step 3 is replaced with the following:

Set $t_i = 1$,

while ($f(\mathbf{v}_i + t_i\Delta\mathbf{v}_i) > f(\mathbf{v}_i) - \alpha t_i \Delta\mathbf{v}_i^T \Delta\mathbf{v}_i$),

$t_i = \beta t_i$,

end

where $\alpha \in (0, 0.5)$ and $\beta \in (0,1)$ are backtracking line search parameters [75]. In each L1-GDBT iteration, the backtracking line search stops only when the objective function decreases. As a

result, "$t_i = \beta t_i$" operation in backtracking line search might execute several times, at the cost of several time-consuming matrix-vector multiplications. Indeed, the step size in L1-GDBB is approximated by a formula reflecting the solutions from the previous and current iterations as well as the gradient of the objective function (Step 3 in Algorithm 5.1). Only two matrix-vector multiplications are needed for each L1-GDBB iteration or each L2-LSQR iteration, which should make them much faster than L1-GDBT.

5.4 Simulation

The numerical and experimental performance of L1-GDBB was compared with BP, L1-GDBT and L2-LSQR. In the simulations, synthetic signals were analytically generated for five spherical absorbers with an absorption distribution given by a truncated parabolic function [28] in a region of interest (ROI) measuring $8\times8\times8$ mm^3 ($81\times81\times81$ voxels), as shown in Figure 5.2(a-b). The radius of the absorbers was set to 300 μm, and they were positioned at the following coordinates (in mm): (0, 0, 0), (0, -1, 0), (0, 1, 0), (0, 0, -1) and (0, 0, 1) (Figure 5.2(b)). The simulated pressure signals were sampled at 281 time points, and supplemented with white Gaussian noise at SNR levels (in dB) of 20, 10 and 0. The simulated data were then reconstructed in Matlab on a 2x Intel Xeon DP X5650 (6x 2.67 GHz) workstation with 144 GB of RAM. Regularization parameters were determined using the L-curve method [44], and a stopping criterion of $\eta = 1\times10^{-5}$ served as the criterion of convergence for all three reconstruction methods. All reconstructions were normalized to the maximum value.

Figure 5.2(c) shows the maximum intensity projection (MIP) of the original data as well as reconstructions using BP, L2-LSQR, L1-GDBT and L1-GDBB in the x-y plane (top view) and y-z plane (side view) at a noise level of 0 dB. Figure 5.2(c) clearly shows that the CNR of the images is enhanced with sparsity-based reconstruction methods. RMSDs between the theoretical image and reconstructions at a noise level of SNR = 0 dB were calculated as 0.0414, 0.0203, 0.0175 and 0.0174 for the BP, L2-LSQR, L1-GBDT and L1-GDBB, respectively. These RMSDs varied negligibly for different noise levels and for the noiseless case. Reconstruction times (in seconds) were 2.5, 27, 224, and 50 for BP, L2-LSQR, L1-GBDT and L1-GDBB, respectively.

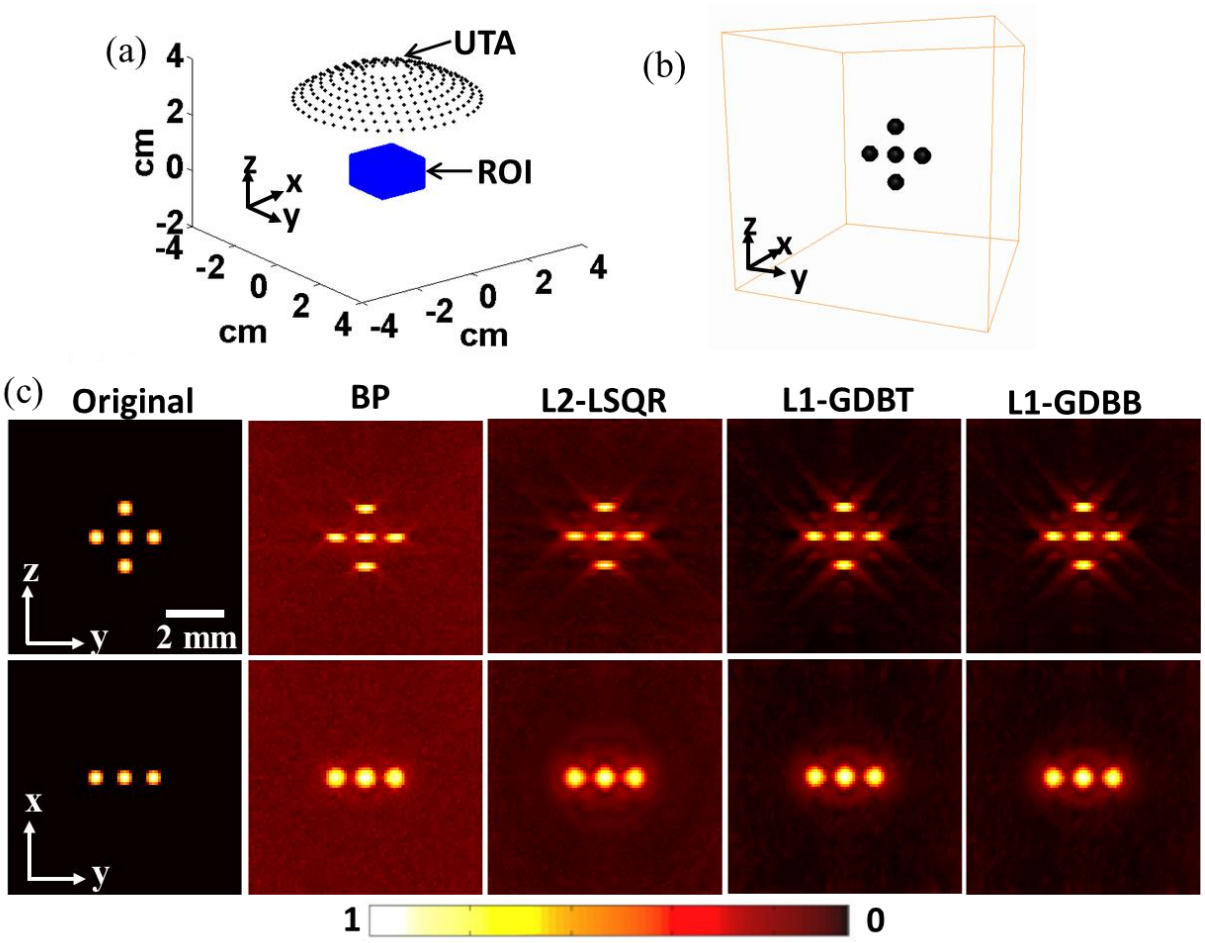

Figure 5.2 Simulation results of the 3D optoacoustic imaging system. (a) 3D optoacoustic tomography geometry tested in simulations and experiments. (b) Sketch of five spherical absorbers with truncated parabolic absorption. (c) MIP results from the original data, and reconstructions using BP, L2-LSQR, L1-GDBT or L1-GDBB at a noise level of 0 dB. Reconstructions are shown in the x-y and y-z planes. (taken from [83])

Figure 5.3 illustrates the convergence performance of L2-LSQR, L1-GDBT and L1-GDBB in the simulation (at a noise level of 0 dB). Figure 5.3(a) and (b) show the variations in the RMSD and objective function $f(v)$ over 20 iterations, while Figure 5.3(c) and (d) show the corresponding CPU times. The L2-LSQR method converged in 4 iterations over 27 s. The non-monotonic behavior of RMSD in the case of L2-LSQR illustrates the inability of this algorithm to deal with incomplete data. The L1-GDBB method converged in 10 iterations over 50 s, while the L1-GDBT method converged in 20 iterations over 224 s. As expected, L1-GDBB converged much faster than L1-GDBT.

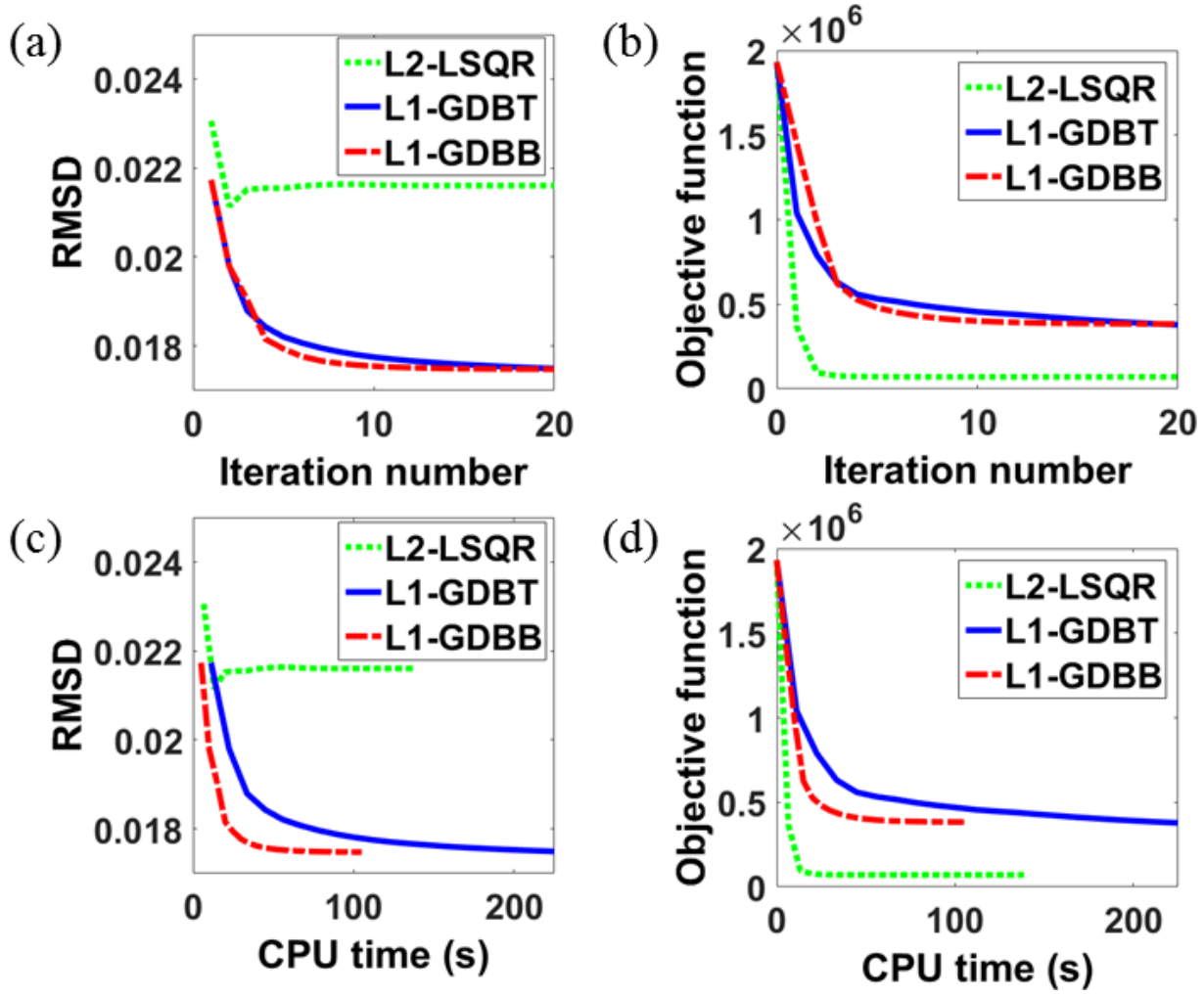

Figure 5.3 Comparison of convergence performance of simulated reconstructions at a noise level of 0 dB using L2-LSQR, L1-GDBT or L1-GDBB. Variations in RMSD and objective function are depicted as a function of (a-b) iteration number and (c-d) CPU time. (taken from [83])

Figure 5.4(a) shows two sets of slices (single plane) of the original data in planes of z=0 (top row) and y=0 (bottom row), as well as the corresponding reconstructions obtained using BP, L2-LSQR, L1-GDBT or L1-GDBB. Comparison of the two trapezoidal regions within dashed lines in the reconstructions generated using L2-LSQR, L1-GDBT or L1-GDBB shows that L1-norm based regularization methods give far fewer artifacts than L2-LSQR. This corroborated the MIP results in Figure 5.2(c). Figure 5.4(b) shows the line profiles of the original data and three reconstructions along Lines 1 indicated in Figure 5.4(a). Comparison of the line profiles of Line

1 in Figure 5.4(b) indicates that L1-GDBT and L1-GDBB generate more accurate reconstructions than BP and L2-LSQR.

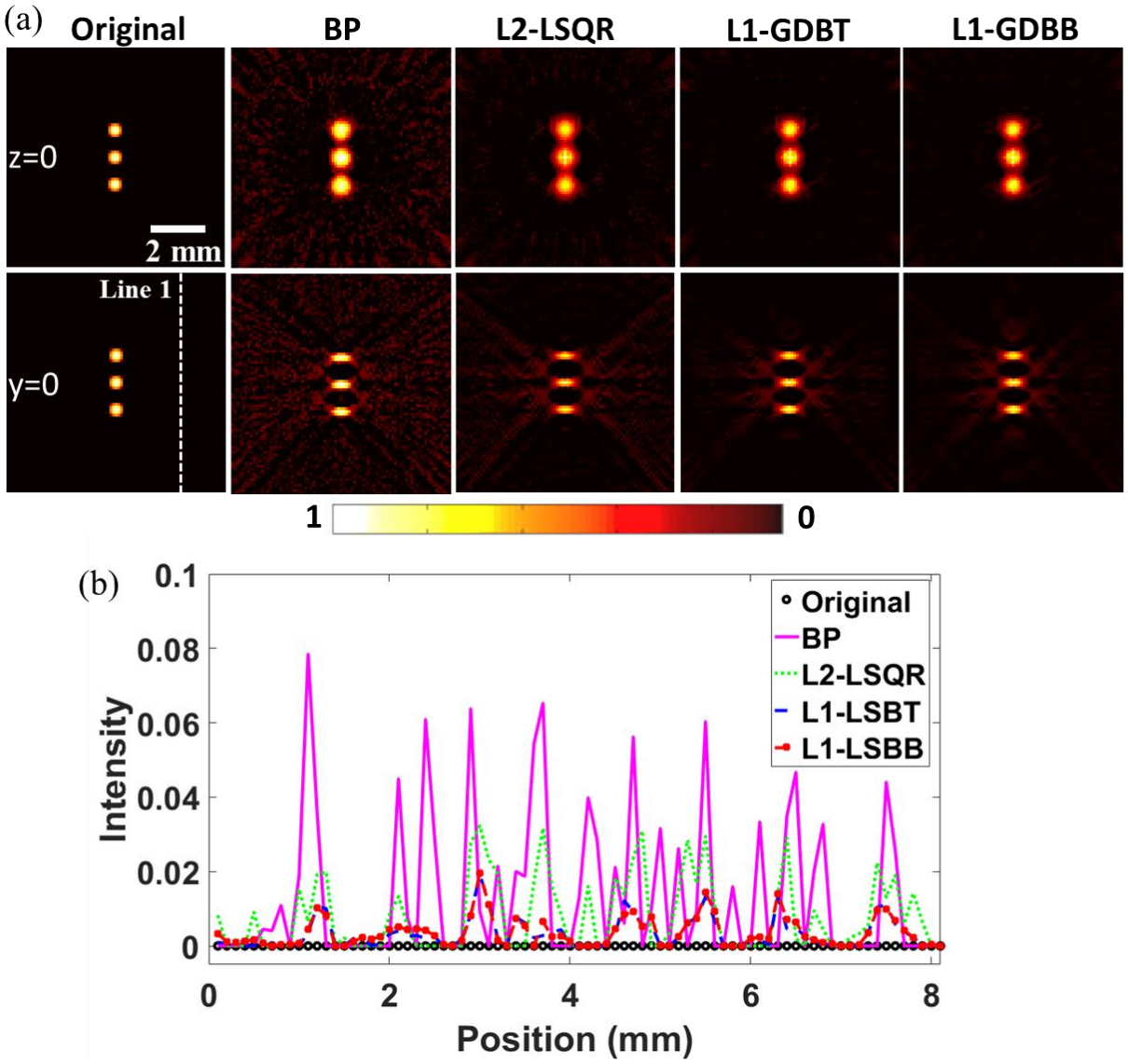

Figure 5.4 Single slices of original data and reconstructions generated using BP, L2-LSQR, L1-GDBT or L1-GDBB at a noise level of 0 dB. (a) z=0 plane (top row) and y=0 plane (bottom row). (b) Line profiles of the original data and four reconstructions along Line 1 in (a). (taken from [83])

5.5 Experiments

To verify and extend these simulations, we compared the performance of BP, L2-LSQR, L1-GDBT and L1-GDBB when the setup [78] described above was used to image the superficial palmar arch vessels of a healthy volunteer at a wavelength of 820 nm. The reconstruction region was 10×10×6.7 mm^3 with a voxel grid of 150×150×100. The acoustic signal was sampled at 251 time points for subsequent reconstructions. Figure 5.5(a-b) show MIP results from the side and top views; the regions enclosed by dashed lines in Figure 5.5(b) are shown as zoomed-in views in Figure 5.5(c). Comparison of the three reconstructions clearly indicates that both L1-GDBT and L1-GDBB generate fewer artifacts and higher CNR than BP and L2-LSQR. To assess this quantitatively, we calculated the SNR and CNR for the target region in dashed boxes labeled "T" and the respective background region in solid-line boxes labeled "B" in Figure 5.5(a-b). SNR was calculated as the ratio of root-mean-square amplitude values of the target region and background region (in dB). CNR was calculated as the mean value difference between target region and background region, divided by the standard deviation of the background region. The SNR values were 10.7, 20.8, 22.2 and 25.6 for BP, L2-LSQR, L1-GBDT and L1-GDBB, respectively. The corresponding CNR values were 3.2, 12.2, 16.7 and 20.9. These ratios confirm that sparsity-based reconstructions methods are superior to L2-LSQR. The reconstruction times (in seconds) were 10, 158, 980, and 245 for BP, L2-LSQR, L1-GBDT and L1-GDBB, respectively.

5.6 Discussion and conclusion

Previous work has used the Barzilai-Borwein scheme in optoacoustic imaging, but only in 2D geometries [84], [85]. In one study [85], the Barzilai-Borwein scheme was used along with augmented Lagrangian-type minimization, while in another study [84], the Barzilai-Borwein scheme was implemented in reconstruction based on a block-sparse discrete cosine transform model. Here we perform 3D sparsity-based reconstruction using a gradient descent with Barzilai-Borwein approach. Sparsity-based image reconstruction performs better in 3D geometries than in 2D geometries because the 3D reconstructed image is more compressible. More advanced reconstruction approaches are necessary in 3D geometries, particularly in cardiovascular and

neurological imaging, which may help reduce the artifacts arising from insufficient data (as shown in Figure 5.2, Figure 5.4 and Figure 5.5).

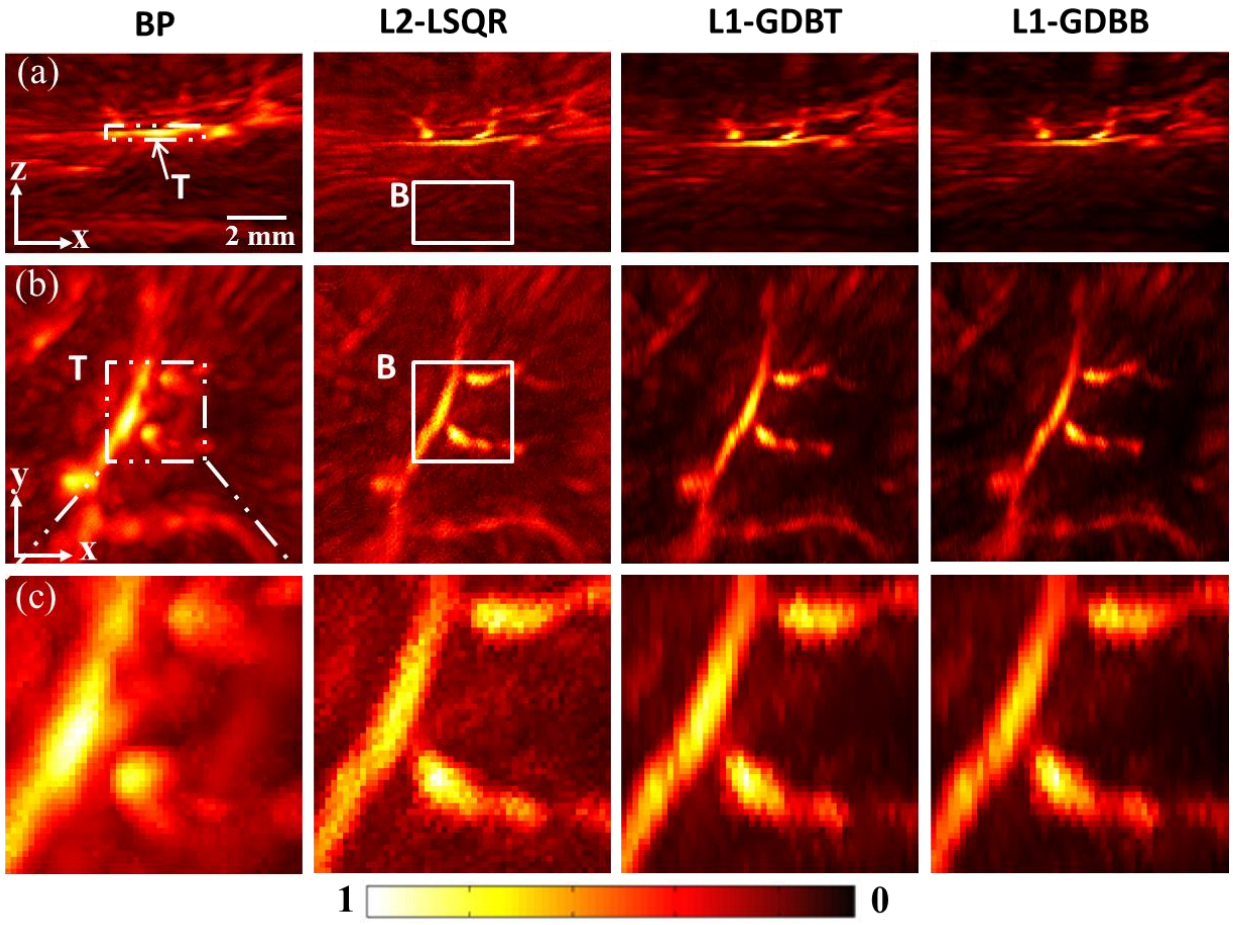

Figure 5.5 Reconstructions of experimental data using BP, L2-LSQR, L1-GDBT and L1-GDBB. (a-b) MIP results (side and top views) of reconstructions of experimental data using BP, L2-LSQR, L1-GDBT and L1-GDBB. (c) Zoomed-in images of the top-view MIP region enclosed in the dot-dashed box in (b). The corresponding region for each reconstruction is shown, even though the box is drawn only for BP. The regions labeled "T" and "B" served as target and background regions, respectively, for calculating SNR and CNR. (taken from [83])

Taken together, our results indicate that the two sparsity-based methods perform well and generate far fewer artifacts and higher CNR than BP reconstruction and commonly-used iterative reconstruction approaches based on L2-norm regularization. Specifically, both L1- GDBT and L1-GDBB performed better than BP and L2-LSQR in simulation and experiments, and L1-GDBB showed a 4-fold faster computational time than L1-GDBT. The computational complexity at each iteration of the L1-GDBT and

L1-GDBB algorithms are $O(N_{it} \times N^2)$ and $O(N)$, where N represents the size of image and N_{it} is the number of backtracking line search iterations. This substantial gain in reconstruction quality with L1-GDBB with respect to L2-LSQR comes with only a moderate 55% increase in CPU time. Short reconstruction time is essential in practical applications, particularly when processing large datasets, such as in biomedical research. Image reconstruction can be further accelerated through parallel implementations of the algorithms in a graphics processing unit (GPU). For example, efficient GPU implementation of the matrix-vector multiplications in iterative inversions can significantly accelerate L2-LSQR-based reconstruction, even allowing real-time reconstruction with a 2D model [86]. Thereby, similar implementations for a 3D optoacoustic model combined with the L1-GDBB method described here may lead to a highly practical and accurate approach in the future.

The L1-GDBB method can become especially beneficial in the case of incomplete tomographic data. Reasons for this incompleteness may be the restricted accessibility to surrounding positions of the sample or technological constraints limiting the number of channels that can be acquired per laser pulse, e.g. in dynamic imaging applications. A particularly important example of insufficient data is limited-view acquisition, when acoustic signals are collected only over a limited angle. Limited-view acquisition is particularly important for optoacoustic clinical translation as hand-held or endoscopic probes cannot fully enclose the imaged tissue. In this case, proper regularization can also enhance the CNR of the images [74] and reduce sharp artifacts corresponding to the edges of the detection arc [87]. Even with good regularization, structures in certain orientations may not be visualized well in limited-view acquisitions, which can be corrected using other approaches [88]–[90].

In conclusion, the reconstruction approach suggested here can greatly impact the resolution, contrast and overall quality of the optoacoustic images rendered with currently-used 3D tomographic systems. The proposed method may become the method of choice in many practical cases.

6 Data optimization in frequency domain optoacoustic tomography

6.1 Motivation

Frequency domain optoacoustic tomography (FD-OAT), in which the sample is illuminated with an intensity-modulated CW laser, can be used instead of time domain optoacoustic tomography (TD-OAT), in which the object is illuminated with a pulsed laser [16], [91]–[93]. FD-OAT has several advantages over TD-OAT. First, the use of CW lasers makes FD-OAT systems more cost-effective and compact than TD-OAT systems. Second, FD-OAT achieves adequate SNR using much lower laser energies and coherent processing with high duty cycles. TD-OAT and FD-OAT have been compared in terms of SNR [98] and maximum depth [17].

Theoretical advances in FD-OAT [94], [95] have led to the implementation of several FD-OAT systems in the last decade [16], [91], [93], [96], [97]. For example, FD-OAT systems have been successful in phantom and animal experiments utilizing a frequency-swept (chirped), intensity-modulated CW laser and coherent frequency domain signal processing technology.

The reconstruction of FD-OAT images can be performed using an analytical solution such as back-projection [99] or using model-based reconstruction [37]. Usually, model-based reconstruction is superior; for example, it generates fewer negative values and can take into account impulse responses. However, the specific impacts of various system parameters on FD-OAT reconstructions have not been studied yet [37]; these parameters include the total number of projections or modulation frequencies required to avoid aliasing artifacts. Exploring how these parameters influence FD-OAT systems is important for optimizing the geometry of these systems, and it may also be useful for TD-OAT.

In this chapter, model-based FD-OAT reconstruction is explored using measured optoacoustic amplitude and phase at multiple discrete frequencies. The Nyquist-Shannon theorem is used to identify a linear relationship linking the number of projections, reconstruction dimensions/field of view, the number of modulation frequencies and the speed of sound for FD-OAT reconstruction. This formula is validated in numerical simulations. Another formula is derived indicating the minimum number of frequencies needed for adequate reconstruction. Finally condition number of the forward model matrix is studied to reveal the influence of the parameters in FD-OAT.

6.2 Method

Model-based reconstruction in FD-OAT is based on the equation [36], [37]

$$\mathbf{p}(\omega) = \mathbf{M}(\omega)\mathbf{z} \ , \tag{6.1}$$

where $\mathbf{p}(\omega)$ is the vector of the measured complex signals and $\mathbf{z}$ is the vector denoting the object. $\mathbf{M}(\omega)$ is the forward model matrix, which is given as

$$\mathbf{M}(\omega)_{(m,n)(p,q)} = \omega_n \frac{e^{i\left((\omega_n/c)\left|r_m - r_{p,q}\right|\right)}}{\left|r_m - r_{p,q}\right|} \tag{6.2}$$

where $i = \sqrt{-1}$, ω_n is the angular frequency, c is the speed of sound, $r_{p,q}$ is the Cartesian coordinates, and r_m is the transducer position.

The complex forward model matrix $\mathbf{M}(\omega)$ and measurements $\mathbf{p}(\omega)$ can be re-expressed in real number format for the following inversion:

$$\overline{\mathbf{p}(\omega)} = \overline{\mathbf{M}(\omega)}\mathbf{z} \ , \tag{6.3}$$

where $\overline{\mathbf{p}(\omega)} = \left(\mathbf{Re}\left(\mathbf{p}(\omega)\right); \mathbf{Im}\left(\mathbf{p}(\omega)\right)\right)$, $\overline{\mathbf{M}(\omega)} = \left(\mathbf{Re}\left(\mathbf{M}(\omega)\right); \mathbf{Im}\left(\mathbf{M}(\omega)\right)\right)$, $\mathbf{Re}(\ )$ and $\mathbf{Im}(\ )$ are the real and imaginary parts of the matrix.

The inversion of Eq. (6.3) can be achieved by traditional Tikhonov regularization using

$$\arg\min_{\mathbf{z}} \left(\left\| \overline{\mathbf{M}(\omega)}\mathbf{z} - \overline{\mathbf{p}(\omega)} \right\|_2^2 + \alpha \left\| \mathbf{z} \right\|_2^2 \right), \tag{6.4}$$

where α is the regularization parameter.

6.3 Total number of projections needed to avoid aliasing artifacts

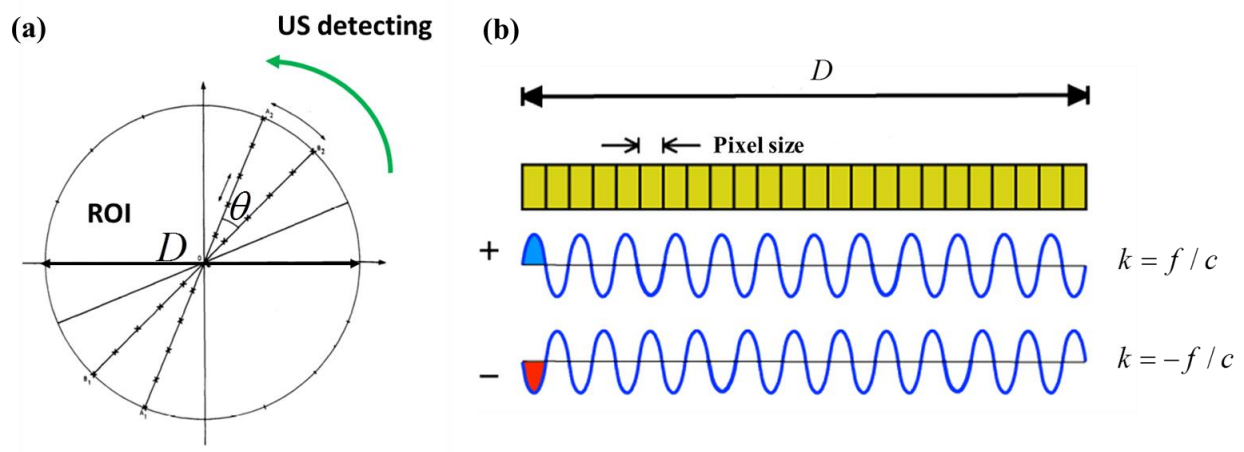

Figure 6.1 Projection parameters that influence FD-OAT reconstruction. (a) Detection geometry. (b) One full phase cycle is needed to uniquely differentiate each pixel.

The CW laser at a modulated frequency of f can extract an object of size c/f, where c is the speed of sound of the object in the medium. Because signal with a modulation frequency f is bipolar, one full phase cycle is needed to within an object of size $c/2f$ (Figure 6.1). Based on the Nyquist-Shannon theorem, the maximum interval between two neighboring projections at the edge of the reconstruction dimension (D) should not be greater than $c/2f$:

$$\theta \bullet \frac{D}{2} \le \frac{c}{2f} \tag{6.5}$$

where θ is the detection angle interval. Then the maximum detection angle interval $\theta_{\max}$ needed for a unique reconstruction is given by

$$\theta_{\max} = c / Df \tag{6.6}$$

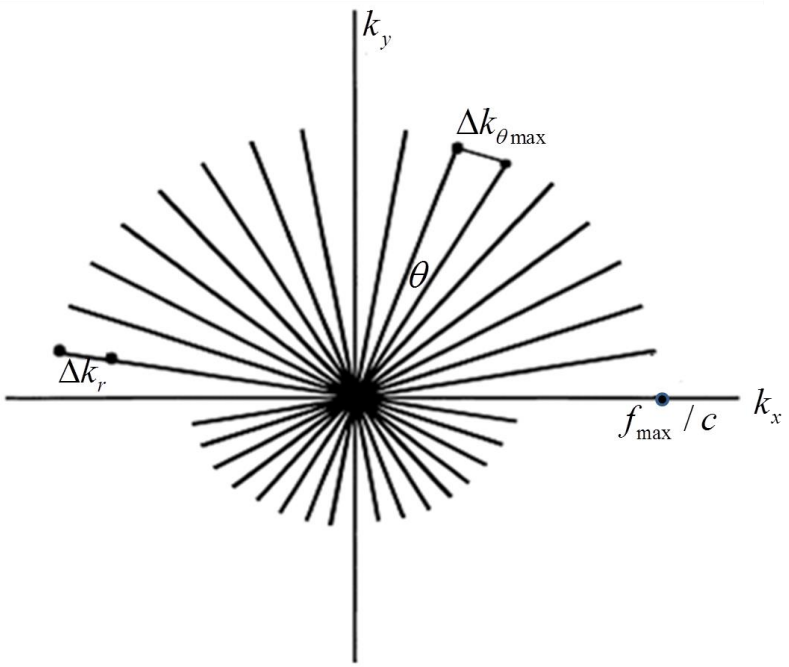

Figure 6.2. FD-OAT geometry in the frequency domain. $\Delta k_{\theta\max}$ is the largest angular spacing between two neighboring projections, Δk_r is the radial sampling interval, $f_{\max}$ is the maximum frequency and c is the speed of sound.

As a result, the minimum total number of projections $N_{P\_\min}$ for 360° detection geometry in FD-OAT shows the following linear relationship with reconstruction dimension D, modulation frequency f and speed of sound c:

$$N_{P\_\min} = 2\pi / \theta_{\max} = 2\pi Df / c \ . \tag{6.7}$$

The maximum detection angle interval $\theta_{\max}$ to avoid aliasing artifacts can also be explained in the frequency domain [100]–[102]. If the radial sampling interval Δk_r is sufficient to reconstruct S pixels along the reconstruction dimension D, then the largest angular spacing $\Delta k_{\theta\max}$

between two neighboring projections should not be greater than the radial k-space sampling interval Δk_r:

$$\Delta k_{\theta\max} = \theta_{\max} \bullet \frac{f_{\max}}{c} = \Delta k_r = \frac{1}{D} \tag{6.8}$$

Thus the maximum detection angle interval $\theta_{\max}$ is

$$\theta_{\max} = \frac{c}{D \bullet f_{\max}} \ . \tag{6.9}$$

Applying Eq. (6.9) to the individual modulation frequency in FD-OAT yields Eq. (6.6).

6.4 Validation of the total number of projections needed at a particular modulation frequency

The prediction in Eq. (6.7) was validated using the following simulation. A sphere of diameter 400 μm is positioned at the edge of the FOV with a diameter of 12 mm [Figure 6.3(a)]. The edge is the most difficult part of the image to reconstruct. We investigate the minimum number of projections needed to obtain a reconstruction without aliasing over 360º at a single modulation frequency f =2.6 MHz. Reconstructions are performed using projections corresponding to 20%, 50% and 100% of $N_{P\_\min}$ based on Eq. (6.7) [Figure 6.3 (b-d)]. We also use the following criterion to get $P_{\min}$:

$$\left\| \mathrm{Recon}_p - \mathrm{Recon}_{p-1} \right\|_2^2 / \left\| \mathrm{Recon}_{p-1} \right\|_2^2 \le \eta \ , \tag{6.10}$$

where Recon_i is the reconstruction with total number of projections i, and η is set to 2×10^{-3}.

Figure 6.3(e) shows the criterion as a function of projection number, and Figure 6.3(f) shows the maximum intensity of the reconstructed image as a function of projection number.

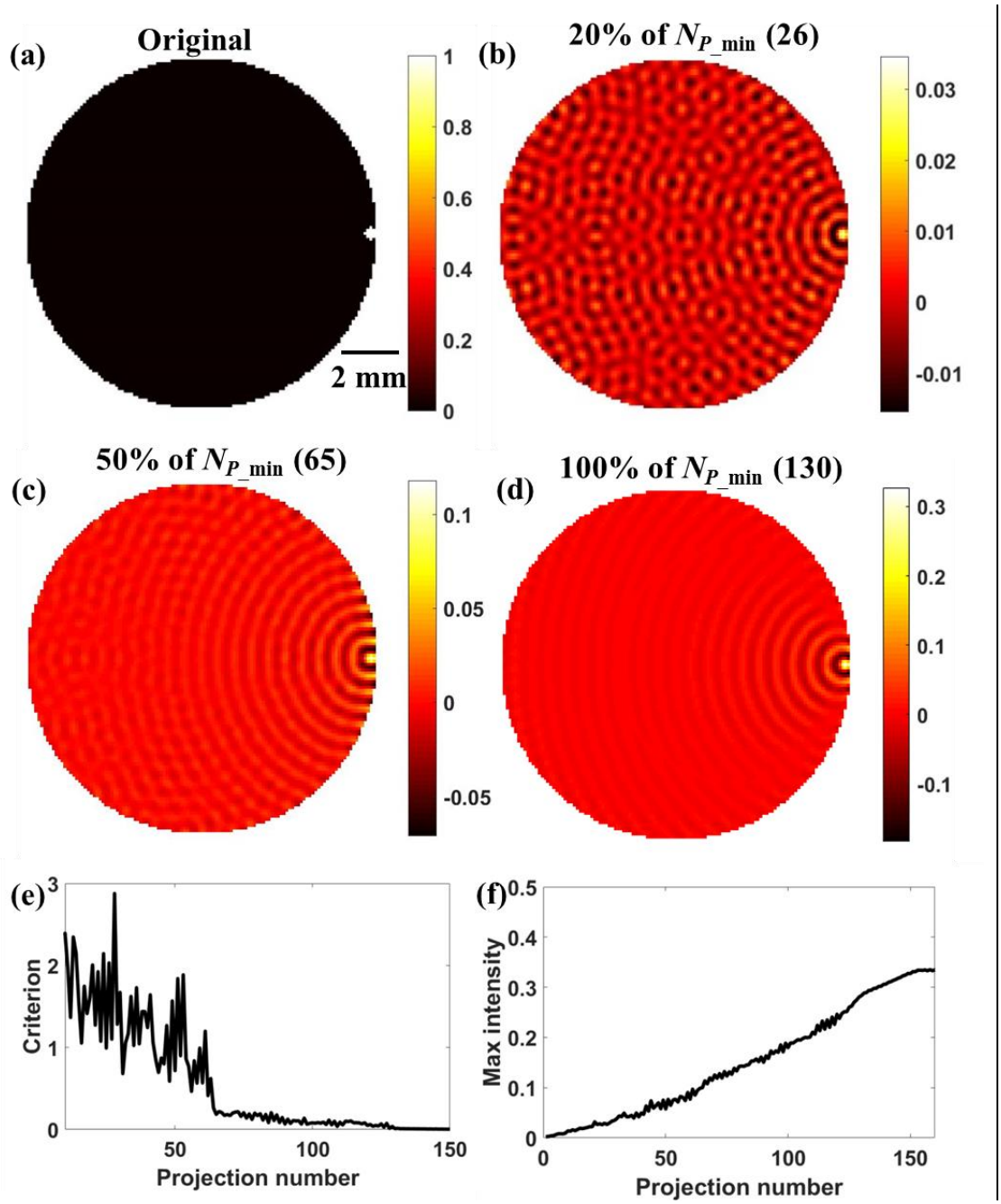

Figure 6.3 Validation of the predicted minimum number of projections needed to avoid aliasing artifacts during FD-OAT reconstruction. (a) Original image. (b-d) Reconstructions with projection numbers equal to 20%, 50% or 100% of the required projections at the modulation frequency of 2.6 MHz and reconstruction dimension of 12 mm. (e) Criterion as a function of projection number. (f) Maximum intensity of the reconstruction as a function of projection number.

6.5 Total number of modulation frequencies needed for even sampling

A total number of modulation frequencies N_F is generated with an even sampling (ES) pattern over the bandwidth $(0, f_{\max}]$. The individual modulation frequency f_{ES}^{i} is given as [37]

$$f_{\mathrm{ES}}^{i} = i \bullet f_{\max} / N_F \ . \tag{6.11}$$

To ensure a unique reconstruction, the total number of independent measurements should not more than twice of the total number of pixels. The sum of projections $[P_1,...,P_F]$ at the N_F modulation frequencies can be described as

$$P_1 + P_2 + ... + P_F = \frac{2\pi D}{c}\left(f_1 + ... + f_F\right) = \frac{2\pi D}{c} \bullet \frac{f_{\max} N_F}{2} \geq 2 * \frac{\pi}{4}\left(\frac{D}{f_{\max} / 2c}\right)^2 . \tag{6.12}$$

In this case, the minimum total number of modulation frequencies $N_{F\_\min}$ for the reconstruction dimension (D) with the highest frequency $f_{\max}$ should be

$$N_{F\_\min} = 2D \bullet f_{\max} / c \ . \tag{6.13}$$

6.6 Analysis the measurements optimization with condition number of forward matrix

The condition number of the forward model matrix in FD-OAT indicates the ability of how good the original image can be reconstructed [37]. Using simulations, we investigate how reconstruction quality changes when N_F and N_P fall below the respective $N_{F\_\min}$ and $N_{P\_\min}$ thresholds derived using the Eq. (6.13) and Eq. (6.7). This validates our mathematical approach, and it also provides a rational basis for assessing reconstruction quality when the numbers of projections and/or modulation frequencies are too few. Simulations were performed using the following parameters: detection angle, 180°; reconstruction grid, 60 × 60; reconstruction resolution, 200 μm; and speed of sound, 1500 m/s. In this case, $N_{F\_\min}$ is 60, and $N_{P\_\min}$ for

individual modulation frequencies is chosen based on Eq. (6.7). Modulation frequencies evenly span the interval [$\frac{3.75}{N_F}$-3.75] MHz based on the speed of sound and reconstruction resolution. The total number of frequencies N_F and total number of projections N_P are systematically reduced to assess the effects on condition number. Among projections [$P_1,...,P_F$], all projections for individual frequencies $P_i > N_P$ are reduced to N_P. Figure 6.4(a) shows the logarithm of condition number as a function of the ratios of frequency or projection number to their respective minimum thresholds. (The logarithm is taken because of the large range in condition numbers.) Figure 6.4(b) shows how the ratio of the total number of measurements $N_{measurements}$ to total number of pixels N_{pixels} varies with the ratios of frequency or projection number to their respective minimum thresholds.

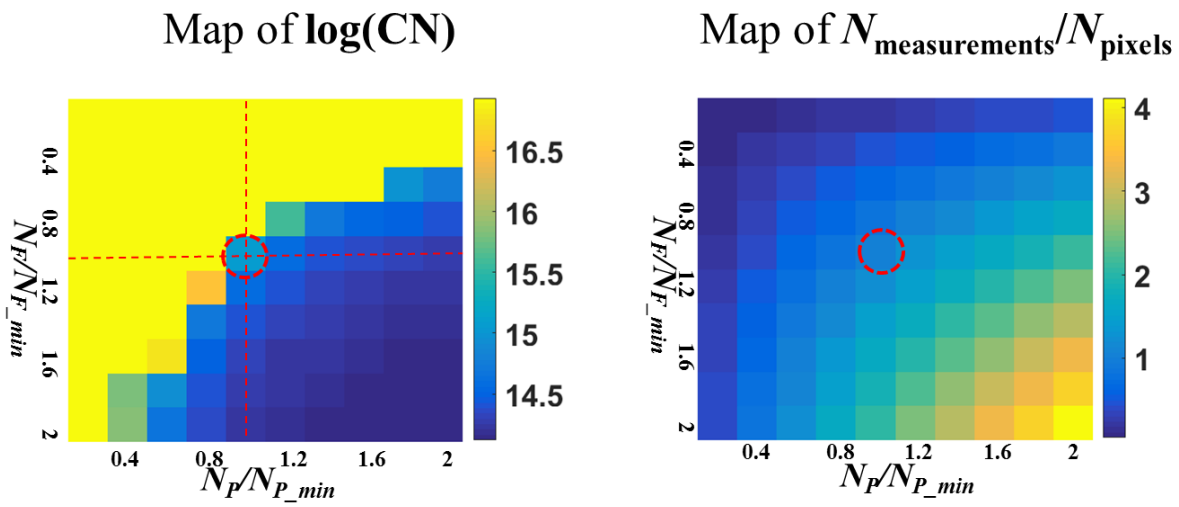

Figure 6.4 (a) Map of the logarithm of condition number (CN) as a function of different numbers of projections and modulation frequencies. (b) Map of the ratio of total measurements to total pixels as a function of different numbers of projections and modulation frequencies.

6.7 Discussion and conclusion

In this chapter we explore the use of frequency domain model-based reconstruction to guide the setting of geometry parameters for FD-OAT systems. This approach may also be useful for time domain optoacoustic imaging.

Previous frequency domain optoacoustic imaging approaches defined a “global” projection number that was the same for all modulation frequencies within the frequency band. The approach proposed here, based on the Nyquist theorem, uses an equation that determines the minimum projection number separately for *each* frequency in the band, in order to ensure a unique reconstruction. This equation is validated with a numerical simulation for different frequencies and different reconstruction image sizes. This equation is validated in the case of noiseless data. In the presence of noise, the number of required projections may be greater than what the equation indicates.

We also analyzed the influence of the number of frequencies sampled within a bandwidth on the resulting reconstruction. The minimum number of frequencies needed to achieve a unique reconstruction in FD-OAT can be calculated analytically. This approach is validated by computing the condition number of the frequency domain model matrix for different numbers of modulation frequencies within the bandwidth.

The condition number of the frequency domain model matrix correlates with the robustness of the reconstruction to input error or noise. Figure 6.4(a) shows that when the modulation frequency number and projection number are both insufficient, the condition number is too high, indicating that it is impossible to get a unique reconstruction for the general case. Conversely, when the modulation frequency number and projection number are both sufficient, a unique reconstruction is possible in all cases. In situations when one or the other number is insufficient, the other parameter can be manipulated to compensate. Thus it may be useful to perform condition number analysis for FD-OAT in order to optimize the procedure when data limitations are likely. Such analysis may be useful even when sufficient frequencies and projections are available, since it can define the minimum dataset needed for adequate reconstruction, allowing data elimination for quality control reasons without jeopardizing the reconstruction.

7 Conclusion and outlook

7.1 Conclusive remarks

Reconstruction is an essential process for optoacoustic tomography. Accurate reconstruction permits visualization of complex anatomical structures, and it facilitates subsequent multispectral analysis. The present work introduced model-based acoustic inversion methods for various optoacoustic tomography systems.

First, a method for accelerating optoacoustic reconstruction and performing system analysis using a wavelet-packet framework is proposed and tested with an optoacoustic system involving a single-element transducer. The spatial impulse response of the transducer is incorporated into the optoacoustic system model matrix for subsequent inversion. Transferring the model matrix and the optoacoustic signal into the wavelet domain significantly accelerates the reconstruction, which enables parallel TSVD inversion on a much smaller scale. In the event that the optoacoustic model matrix is too big for SVD analysis, the condition number can be calculated for smaller submatrices generated after wavelet packet decomposition.

Next, a sparsity-based reconstruction is developed for a cross-sectional optoacoustic system with a focused transducer array. A cost function is used that includes the L1 norm of the image in sparse representation and a total variation term. The minimization process is implemented with gradient descent with backtracking line search. Model-based sparsity-based inversion performs better than conventional Tikhonov regularization and back-projection reconstruction for reconstructing numerical and experimental datasets involving full-view and limited-view geometries, giving sharper images and weaker streak artifacts.

Sparsity-based reconstruction is then adapted to 3D geometries, since ultrasound waves in optoacoustics propagate in all directions and reconstructed images are more compressible in 3D. To accelerate reconstruction, Barzilai-Borwein line search is used to determine analytically the step size for each iteration of gradient descent. The proposed method offers 4-fold faster reconstruction than the previously reported L1-norm regularized reconstruction based on gradient descent with backtracking line search. Moreover, the new algorithm provides higher-quality images with fewer artifacts than the L2-norm regularized reconstruction and the back-projection reconstruction.

Finally, optoacoustic reconstruction is studied in the frequency domain. The Nyquist-Shannon theorem is applied to uncover a linear relationship among projection number, reconstruction dimensions, modulation frequency and speed of sound to obtain a unique reconstruction. .We also get a formula to get the minimum demand of the frequencies needed. Analysis of forward model matrix characteristics, e.g. condition number, which is typical in time domain optoacoustic tomography, is extended here to the frequency domain to reveal inherent reconstruction properties.

7.2 Outlook and future directions

One direction is to accelerate the reconstruction with the wavelet packet framework utilizing model matrix sparsity. Extending the 2D algorithm presented here to 3D will require overcoming several challenges. One is to reduce the memory of the large model matrix in 3D as much as possible before wavelet packet decomposition. Another is to deal with the expected complexity of inverting with wavelet packets in the case of limited-view geometry.

Sparsity-based optoacoustic reconstructions are shown here to provide superior image quality over existing reconstruction algorithms. However, sparsity-based reconstructions in this thesis are implemented on a CPU and require a certain amount of computational time. Short reconstruction time is essential in practical applications, particularly for large datasets. Image reconstruction can be further accelerated through parallel implementations of the algorithms in a graphics processing unit (GPU). For example, efficient GPU implementation of the matrix-vector multiplications in iterative inversions can significantly accelerate L2-norm based reconstruction, even allowing real-time reconstruction with a 2D model [86]. Therefore, similar

implementations for a 3D optoacoustic model combined with the sparsity-based method described here may lead to a tool that is both accurate and practical. Another direction is to study the random selection on projections under the sparsity-based reconstruction framework to reduce the measurements and reconstruction time.

Finally, frequency domain optoacoustic tomography is analyzed here as an alternative to the same technique in the time domain. Frequency domain optoacoustic tomography offers the freedom of selectively exciting the object with a certain frequency band or even single frequencies, depending on absorber size (reconstruction image resolution). Sampling pattern is an interesting topic in frequency domain optoacoustic tomography reconstruction. In addition, frequency domain model-based reconstruction can be used to study sparsity-based reconstruction methods involving single modulation frequencies, which may be useful for understanding and improving time domain sparsity-based optoacoustic reconstruction. It may be possible to further improve frequency domain model-based reconstruction algorithms using fast Fourier transformation.

Publications list

1. Yiyong Han, Lu Ding, Xosé Luis Deán Ben, Daniel Razansky, Jaya Prakash, Vasilis Ntziachristos. Three-dimensional optoacoustic reconstruction using fast sparse representation. *Optics Letters* 42(5), 979-982 (2017)
2. Yiyong Han, Vasilis Ntziachristos, Amir Rosenthal. Optoacoustic image reconstruction and system analysis for finite-aperture detectors under the wavelet-packet framework. *Journal of Biomedical Optics* 21(1), 016002 (2016)
3. Yiyong Han, Stratis Tzoumas, Antonio Nunes, Vasilis Ntziachristos, Amir Rosenthal. Sparsity-based acoustic inversion in cross-sectional multi-scale optoacoustic imaging. *Medical Physics* 42(9), 5444-5452 (2015)

Bibliography

[1] V. Ntziachristos, “Going deeper than microscopy: the optical imaging frontier in biology.,” *Nat. Methods*, vol. 7, no. 8, pp. 603–614, 2010.

[2] L. V. Wang and S. Hu, “Photoacoustic Tomography: In Vivo Imaging from Organelles to Organs,” *Science*, vol. 335, no. 6075, pp. 1458–1462, Mar. 2012.

[3] C. Li and L. V Wang, “Photoacoustic tomography and sensing in biomedicine,” *Phys. Med. Biol.*, vol. 54, no. 19, pp. R59–R97, 2009.

[4] P. Beard, “Biomedical photoacoustic imaging.,” *Interface Focus*, vol. 1, no. 4, pp. 602–31, 2011.

[5] M. Xu and L. V. Wang, “Photoacoustic imaging in biomedicine,” *Rev. Sci. Instrum.*, vol. 77, no. 4, pp. 1–22, 2006.

[6] D. Razansky, A. Buehler, and V. Ntziachristos, “Volumetric real-time multispectral optoacoustic tomography of biomarkers.,” *Nat. Protoc.*, vol. 6, no. 8, pp. 1121–29, 2011.

[7] G. J. Diebold, T. Sun, and M. I. Khan, “Photoacoustic monopole radiation in one, two, and three dimensions,” *Phys. Rev. Lett.*, vol. 67, no. 24, pp. 3384–3387, 1991.

[8] Lihong V. Wang, *Photoacoustic Imaging and Spectroscopy*. Boca Raton, Florida: CRC Press, 2009.

[9] Lihong V. Wang and Hsin i Wu, *Biomedical Optics*. Hoboken, New Jersey: John Wiley & Sons, 2007.

[10] A. Rosenthal, V. Ntziachristos, and D. Razansky, “Acoustic Inversion in Optoacoustic Tomography: A Review,” *Curr. Med. Imaging Rev.*, vol. 9, no. 4, pp. 318–336, 2013.

[11] J. Yao and L. V. Wang, “Photoacoustic microscopy,” *Laser Photon. Rev.*, vol. 7, no. 5, pp. 758–778, 2013.

[12] J. Yao and L. V. Wang, “Sensitivity of photoacoustic microscopy,” *Photoacoustics*, vol. 2, no. 2, pp. 87–101, 2014.

[13] V. Ntziachristos and D. Razansky, “Molecular imaging by means of multispectral optoacoustic tomography (MSOT),” *Chem. Rev.*, vol. 110, no. 5, pp. 2783–2794, 2010.

[14] D. Razansky, M. Distel, C. Vinegoni, R. Ma, N. Perrimon, R. W. Koster, and V. Ntziachristos, “Multispectral opto-acoustic tomography of deep-seated fluorescent proteins in vivo,” *Nat. Photonics*, vol. 3, no. 7, pp. 412–417, 2009.

[15] X. Wang, Y. Pang, G. Ku, X. Xie, G. Stoica, and L. V Wang, “Noninvasive laser-induced photoacoustic tomography for structural and functional in vivo imaging of the brain.,” *Nat. Biotechnol.*, vol. 21, no. 7, pp. 803–806, 2003.

[16] S. Telenkov, A. Mandelis, B. Lashkari, and M. Forcht, “Frequency-domain photothermoacoustics: Alternative imaging modality of biological tissues,” *J. Appl. Phys.*, vol. 105, no. 10, 2009.

[17] S. a Telenkov and A. Mandelis, “Photothermoacoustic imaging of biological tissues: maximum depth characterization comparison of time and frequency-domain measurements.,” *J. Biomed. Opt.*, vol. 14, no. 4, p. 44025, 2009.

[18] R. A. Kruger, “Photoacoustic ultrasound (PAUS)—Reconstruction tomography,” *Med. Phys.*, vol. 22, no. 10, p. 1605, 1995.

[19] M. Xu and L. V. Wang, “Universal back-projection algorithm for photoacoustic computed tomography,” *Phys. Rev. E - Stat. Nonlinear, Soft Matter Phys.*, vol. 71, no. 1, pp. 1–7, 2005.

[20] K. P. Koestli, M. Frenz, H. Bebie, H. P. Weber, and K. P. Köstli, “Temporal backward projection of optoacoustic pressure transients using fourier transform methods,” *Phys. Med. Biol.*, vol. 46, no. 7, pp. 1863–72, 2001.

[21] Y. Xu and L. V Wang, “Time reversal and its application to tomography with diffracting sources.,” *Phys. Rev. Lett.*, vol. 92, no. 3, p. 33902, 2004.

[22] P. Burgholzer, G. J. Matt, M. Haltmeier, and G. Paltauf, “Exact and approximative imaging methods for photoacoustic tomography using an arbitrary detection surface,” *Phys. Rev. E - Stat. Nonlinear, Soft Matter Phys.*, vol. 75, no. 4, pp. 1–10, 2007.

[23] B. E. Treeby, E. Z. Zhang, and B. T. Cox, "Photoacoustic tomography in absorbing acoustic media using time reversal," *Inverse Probl.*, vol. 26, no. 11, p. 115003, 2010.

[24] A. Rosenthal, D. Razansky, and V. Ntziachristos, "Fast semi-analytical model-based acoustic inversion for quantitative optoacoustic tomography," *IEEE Trans. Med. Imaging*, vol. 29, no. 6, pp. 1275–1285, 2010.

[25] C. G. Hoelen and F. F. de Mul, "Image reconstruction for photoacoustic scanning of tissue structures.," *Appl. Opt.*, vol. 39, no. 31, pp. 5872–5883, 2000.

[26] Y. Han, V. Ntziachristos, and A. Rosenthal, "Optoacoustic image reconstruction and system analysis for finite-aperture detectors under the wavelet-packet framework," *J. Biomed. Opt.*, vol. 21, no. 1, p. 16002, Jan. 2016.

[27] A. Rosenthal, V. Ntziachristos, and D. Razansky, "Model-based optoacoustic inversion with arbitrary-shape detectors.," *Med. Phys.*, vol. 38, no. 7, pp. 4285–4295, 2011.

[28] D. Queirós, X. L. Déan-Ben, A. Buehler, D. Razansky, A. Rosenthal, and V. Ntziachristos, "Modeling the shape of cylindrically focused transducers in three-dimensional optoacoustic tomography.," *J. Biomed. Opt.*, vol. 18, p. 76014, 2013.

[29] K. Wang, S. A. Ermilov, R. Su, H. P. Brecht, A. A. Oraevsky, and M. A. Anastasio, "An imaging model incorporating ultrasonic transducer properties for three-dimensional optoacoustic tomography," *IEEE Trans. Med. Imaging*, vol. 30, no. 2, pp. 203–214, 2011.

[30] A. Buehler, A. Rosenthal, T. Jetzfellner, A. Dima, D. Razansky, and V. Ntziachristos, "Model-based optoacoustic inversions with incomplete projection data," *Med Phys*, vol. 38, no. 3, pp. 1694–1704, 2011.

[31] Y. Xu, L. V Wang, G. Ambartsoumian, and P. Kuchment, "Reconstructions in limited-view thermoacoustic tomography.," *Med. Phys.*, vol. 31, no. 4, pp. 724–733, 2004.

[32] X. L. Deán-Ben, R. Ma, A. Rosenthal, V. Ntziachristos, and D. Razansky, "Weighted model-based optoacoustic reconstruction in acoustic scattering media.," *Phys. Med. Biol.*, vol. 58, no. 16, pp. 5555–66, 2013.

[33] X. L. Deán-Ben, V. Ntziachristos, and D. Razansky, "Effects of small variations of speed of sound in optoacoustic tomographic imaging.," *Med. Phys.*, vol. 41, no. 7, p. 73301, 2014.

[34] X. L. Dean-Ben, A. Buehler, V. Ntziachristos, and D. Razansky, "Accurate model-based reconstruction algorithm for three-dimensional optoacoustic tomography," *IEEE Trans. Med. Imaging*, vol. 31, no. 10, pp. 1922–1928, 2012.

[35] X. L. Deán-Ben, V. Ntziachristos, and D. Razansky, "Acceleration of optoacoustic model-based reconstruction using angular image discretization," *IEEE Trans. Med. Imaging*, vol. 31, no. 5, pp. 1154–1162, 2012.

[36] J. Provost and F. Lesage, "The application of compressed sensing for photo-acoustic tomography," *IEEE Trans. Med. Imaging*, vol. 28, no. 4, pp. 585–594, 2009.

[37] P. Mohajerani, S. Kellnberger, and V. Ntziachristos, "Frequency domain optoacoustic tomography using amplitude and phase," *Photoacoustics*, vol. 2, no. 3, pp. 111–118, 2014.

[38] K. Wang, R. Su, A. a Oraevsky, and M. a Anastasio, "Investigation of iterative image reconstruction in three-dimensional optoacoustic tomography," *Phys. Med. Biol.*, vol. 57, no. 17, pp. 5399–5423, 2012.

[39] F. A. Duck, *Physical Properties of Tissue: A Comprehensive Reference Book*. London: Academic Press, 1990.

[40] P. Laugier and G. Haïat, *Bone Quantitative Ultrasound*. Dordrecht: Springer Netherlands, 2011.

[41] B. T. Cox, S. Kara, S. R. Arridge, and P. C. Beard, "K-Space Propagation Models for Acoustically Heterogeneous Media: Application To Biomedical Photoacoustics.," *J. Acoust. Soc. Am.*, vol. 121, no. 6, pp. 3453–3464, 2007.

[42] L. V Wang and X. Yang, "Boundary conditions in photoacoustic tomography and image reconstruction," *J. Biomed. Opt.*, vol. 12, no. 1, p. 14027, 2007.

[43] K. P. Köstli and P. C. Beard, "Two-dimensional photoacoustic imaging by use of Fourier-transform image reconstruction and a detector with an anisotropic response.," *Appl. Opt.*, vol. 42, no. 10, pp. 1899–908, 2003.

[44] P. C. Hansen, "The L-Curve and its Use in the Numerical Treatment of Inverse Problems," *Comput. Inverse Probl. Electrocardiology, ed. P. Johnston, Adv. Comput. Bioeng.*, vol. 4, pp. 119–142, 2000.

[45] K. Wang, R. W. Schoonover, R. Su, A. Oraevsky, and M. A. Anastasio, "Discrete imaging models for three-dimensional optoacoustic tomography using radially symmetric expansion functions," *IEEE Trans. Med. Imaging*, vol. 33, no. 5, pp. 1180–1193, 2014.

[46] T. Jetzfellner, A. Rosenthal, K. H. Englmeier, A. Dima, M. N. A. Caballero, D. Razansky, and V. Ntziachristos, "Interpolated model-matrix optoacoustic tomography of the mouse brain," *Appl. Phys. Lett.*, vol. 98, no. 16, pp. 1–4, 2011.

[47] C. Lutzweiler, X. L. Deán-Ben, and D. Razansky, "Expediting model-based optoacoustic reconstructions with tomographic symmetries.," *Med. Phys.*, vol. 41, p. 13302, 2014.

[48] A. Taruttis, S. Morscher, N. C. Burton, D. Razansky, and V. Ntziachristos, "Fast multispectral optoacoustic tomography (MSOT) for dynamic imaging of pharmacokinetics and biodistribution in multiple organs," *PLoS One*, vol. 7, no. 1, p. e30491, 2012.

[49] E. Herzog, A. Taruttis, N. Beziere, A. a Lutich, and D. Razansky, "Optical imaging of cancer heterogeneity with Multispectral," *Radiology*, vol. 263, no. 2, pp. 461–468, 2012.

[50] A. Buehler, M. Kacprowicz, A. Taruttis, and V. Ntziachristos, "Real-time handheld multispectral optoacoustic imaging.," *Opt. Lett.*, vol. 38, no. 9, pp. 1404–6, 2013.

[51] J. Gateau, M. A. A. Caballero, A. Dima, and V. Ntziachristos, "Three-dimensional optoacoustic tomography using a conventional ultrasound linear detector array: whole-body tomographic system for small animals.," *Med. Phys.*, vol. 40, no. 1, p. 13302, 2013.

[52] A. Rosenthal, T. Jetzfellner, D. Razansky, and V. Ntziachristos, "Efficient framework for model-based tomographic image reconstruction using wavelet packets," *IEEE Trans. Med. Imaging*, vol. 31, no. 7, pp. 1346–1357, 2012.

[53] R. Ma, A. Taruttis, V. Ntziachristos, and D. Razansky, "Multispectral optoacoustic tomography (MSOT) scanner for whole-body small animal imaging," *Opt. Express*, vol. 17, no. 24, p. 21414, Nov. 2009.

[54] M. Roumeliotis, P. Ephrat, J. Patrick, and J. J. L. Carson, "Development and characterization of an omnidirectional photoacoustic point source for calibration of a staring 3D photoacoustic imaging system.," *Opt. Express*, vol. 17, no. 17, pp. 15228–15238, 2009.

[55] S. A. Mallat, *A Wavelet Tour of Signal Processing*. San Diego, California: Acadmic, 1998.

[56] P. C. Hansen, “The truncated SVD as a method for regularization,” *Bit*, vol. 27, no. 4, pp. 534–553, 1987.

[57] W. W. Hager, “Condition Estimates,” *SIAM J. Sci. Stat. Comput.*, vol. 5, no. 2, pp. 311–316, 1984.

[58] Z. Wang, A. C. Bovik, H. R. Sheikh, and E. P. Simoncelli, “Image Quality Assessment: From Error Visibility to Structural Similarity,” *IEEE Trans. Image Process.*, vol. 13, no. 4, pp. 600–612, Apr. 2004.

[59] D. Calvetti, S. Morigi, L. Reichel, and F. Sgallari, “Tikhonov regularization and the L-curve for large discrete ill-posed problems,” *J. Comput. Appl. Math.*, vol. 123, no. 1–2, pp. 423–446, 2000.

[60] M. Xu and L. V Wang, “Analytic explanation of spatial resolution related to bandwidth and detector aperture size in thermoacoustic or photoacoustic reconstruction.,” *Phys. Rev. E. Stat. Nonlin. Soft Matter Phys.*, vol. 67, no. 5 Pt 2, p. 56605, 2003.

[61] P. Burgholzer, J. Bauer-Marschallinger, H. Grun, M. Haltmeier, and G. Paltauf, “Temporal back-projection algorithms for photoacoustic tomography with integrating line detectors,” *Inverse Probl.*, vol. 23, no. 6, pp. S65–S80, 2007.

[62] V. G. Andreev, A. A. Karabutov, S. V. Solomatin, E. V. Savateeva, V. Aleynikov, Y. V Zhulina, R. D. Fleming, and A. A. Oraevsky, “Opto-acoustic tomography of breast cancer with arc-array-transducer,” *Proc. SPIE*, vol. 3916, pp. 36–47, 2000.

[63] S. Morscher, W. H. P. Driessen, J. Claussen, and N. C. Burton, “Semi-quantitative multispectral optoacoustic tomography (MSOT) for volumetric PK imaging of gastric emptying,” *Photoacoustics*, vol. 2, no. 3, pp. 103–110, 2014.

[64] Y. Han, S. Tzoumas, A. Nunes, V. Ntziachristos, and A. Rosenthal, “Sparsity-based acoustic inversion in cross-sectional multiscale optoacoustic imaging,” *Med. Phys.*, vol. 42, no. 9, pp. 5444–5452, 2015.

[65] D. Liang, H. F. Zhang, and L. Ying, “Compressed-sensing Photoacoustic Imaging based on random optical illumination,” *Int. J. Funct. Inform. Personal. Med.*, vol. 2, no. 4, p. 394, 2009.

[66] X. Liu, D. Peng, W. Guo, X. Ma, X. Yang, and J. Tian, “Compressed sensing

photoacoustic imaging based on fast alternating direction algorithm," *Int. J. Biomed. Imaging*, vol. 2012, p. 206214, 2012.

[67] Z. Guo, C. Li, L. Song, and L. V Wang, "Compressed sensing in photoacoustic tomography in vivo.," *J. Biomed. Opt.*, vol. 15, no. 2, p. 21311, 2010.

[68] M. Sun, N. Feng, Y. Shen, X. Shen, L. Ma, J. Li, and Z. Wu, "Photoacoustic imaging method based on arc-direction compressed sensing and multi-angle observation," *Opt. Express*, vol. 19, no. 16, p. 14801, 2011.

[69] M. Lustig, D. Donoho, and J. M. Pauly, "Sparse MRI: The application of compressed sensing for rapid MR imaging," *Magn. Reson. Med.*, vol. 58, no. 6, pp. 1182–1195, 2007.

[70] L. Rudin S. Osher and E. Fatemi, "Nonlinear total variation based noise removal algorithms," *Phys. D*, vol. 60, no. 1–4, pp. 259–268, 1992.

[71] Y. Dong, T. Görner, and S. Kunis, "An iterative reconstruction scheme for photoacoustic imaging," *Preprint*, pp. 1–15, 2011.

[72] A. A. Oraevsky, K. Wang, E. Y. Sidky, M. A. Anastasio, A. A. Oraevsky, X. Pan, and L. V Wang, "Limited data image reconstruction in optoacoustic tomography by constrained total variation minimization," *Photons Plus Ultrasound Imaging Sens. 2011*, vol. 7899, p. 78993U–6, 2011.

[73] L. Yao and H. B. Jiang, "Enhancing finite element-based photoacoustic tomography using total variation minimization," *Appl. Opt.*, vol. 50, no. 25, pp. 5031–5041, 2011.

[74] L. Yao and H. Jiang, "Photoacoustic image reconstruction from few-detector and limited-angle data," *Biomed. Opt. Express*, vol. 2, no. 9, p. 2649, 2011.

[75] S. Boyd and L. Vandenberghe, *Convex optimization theory*, vol. 25, no. 3. New York: Cambridge University Press, 2010.

[76] E. Y. Sidky, C.-M. Kao, and X. Pan, "Accurate image reconstruction from few-views and limited-angle data in divergent-beam CT," *J. Xray. Sci. Technol.*, vol. 14, pp. 119–139, 2009.

[77] J. Meng, L. H. V Wang, L. L. Ying, D. Liang, and L. Song, "Compressed-sensing photoacoustic computed tomography in vivo with partially known support," *Opt. Express*,

vol. 20, no. 15, pp. 16510–16523, 2012.

[78] X. L. Deán-Ben and D. Razansky, "Functional optoacoustic human angiography with handheld video rate three dimensional scanner," *Photoacoustics*, vol. 1, no. 3–4, pp. 68–73, 2013.

[79] X. L. Dean-Ben, A. Ozbek, and D. Razansky, "Volumetric Real-Time Tracking of Peripheral Human Vasculature With GPU-Accelerated Three-Dimensional Optoacoustic Tomography," *IEEE Trans. Med. Imaging*, vol. 32, no. 11, pp. 2050–2055, Nov. 2013.

[80] S. Tzoumas, A. Nunes, I. Olefir, S. Stangl, P. Symvoulidis, S. Glasl, C. Bayer, G. Multhoff, and V. Ntziachristos, "Eigenspectra optoacoustic tomography achieves quantitative blood oxygenation imaging deep in tissues," *Nat. Commun.*, vol. 7, no. May, p. 12121, 2016.

[81] J. Barzilai and J. M. Borwein, "Two-point step size gradient methods," *IMA J. Numer. Anal.*, vol. 8, no. 1, pp. 141–148, 1988.

[82] C. C. Paige and M. a. Saunders, "LSQR: An Algorithm for Sparse Linear Equations and Sparse Least Squares," *ACM Trans. Math. Softw.*, vol. 8, no. 1, pp. 43–71, 1982.

[83] Y. Han, L. Ding, X. L. D. Ben, D. Razansky, J. Prakash, and V. Ntziachristos, "Three-dimensional optoacoustic reconstruction using fast sparse representation," *Opt. Lett.*, vol. 42, no. 5, p. 979, Mar. 2017.

[84] C. Zhang, Y. Wang, and J. Wang, "Efficient block-sparse model-based algorithm for photoacoustic image reconstruction," *Biomed. Signal Process. Control*, vol. 26, pp. 11–22, 2016.

[85] C. Zhang, Y. Zhang, and Y. Wang, "A photoacoustic image reconstruction method using total variation and nonconvex optimization.," *Biomed. Eng. Online*, vol. 13, no. 1, p. 117, 2014.

[86] L. Ding, X. L. De??n-Ben, and D. Razansky, "Real-Time Model-Based Inversion in Cross-Sectional Optoacoustic Tomography," *IEEE Trans. Med. Imaging*, vol. 35, no. 8, pp. 1883–1891, 2016.

[87] J. Frikel and E. T. Quinto, "Artifacts in Incomplete Data Tomography with Applications to Photoacoustic Tomography and Sonar," *SIAM J. Appl. Math.*, vol. 75, no. 2, pp. 703–

725, Jan. 2015.

[88] J. Gateau, T. Chaigne, O. Katz, S. Gigan, and E. Bossy, "Improving visibility in photoacoustic imaging using dynamic speckle illumination.," *Opt. Lett.*, vol. 38, no. 23, pp. 5188–91, 2013.

[89] L. L. V. L. L. V. Wang, G. Li, J. Xia, and L. L. V. L. L. V. Wang, "Ultrasonic-heating-encoded photoacoustic tomography with virtually augmented detection view," *Optica*, vol. 2, no. 4, p. 307, 2015.

[90] X. L. Dean-Ben, L. Ding, and D. Razansky, "Dynamic particle enhancement in limited-view optoacoustic tomography," pp. 1–5, 2015.

[91] S. Kellnberger, N. C. Deliolanis, D. Queirós, G. Sergiadis, and V. Ntziachristos, "In vivo frequency domain optoacoustic tomography," *Opt. Lett.*, vol. 37, no. 16, p. 3423, 2012.

[92] S. Telenkov and A. Mandelis, "Signal-to-noise analysis of biomedical photoacoustic measurements in time and frequency domains," *Rev. Sci. Instrum.*, vol. 81, no. 12, p. 124901, 2010.

[93] S. a Telenkov and A. Mandelis, "Fourier-domain biophotoacoustic subsurface depth selective amplitude and phase imaging of turbid phantoms and biological tissue.," *J. Biomed. Opt.*, vol. 11, no. 4, p. 44006, 2006.

[94] A. Mandelis and C. Feng, "Frequency-domain theory of laser infrared photothermal radiometric detection of thermal waves generated by diffuse-photon-density wave fields in turbid media," *Phys. Rev. E - Stat. Nonlinear, Soft Matter Phys.*, vol. 65, no. 2, pp. 2002–2003, 2002.

[95] N. Baddour, "Theory and analysis of frequency-domain photoacoustic tomography.," *J. Acoust. Soc. Am.*, vol. 123, no. 5, pp. 2577–2590, 2008.

[96] Y. Fan, A. Mandelis, G. Spirou, and I. A. Vitkin, "Development of a laser photothermoacoustic frequency-swept system for subsurface imaging: theory and experiment.," *J. Acoust. Soc. Am.*, vol. 116, no. 6, pp. 3523–3533, 2004.

[97] L. V Wang and K. Maslov, "Photoacoustic imaging of biological tissue with intensity-modulated continuous-wave laser.," *J. Biomed. Opt.*, vol. 13, no. 2, p. 24006, 2005.

[98] A. Petschke and P. J. La Rivière, "Comparison of intensity-modulated continuous-wave lasers with a chirped modulation frequency to pulsed lasers for photoacoustic imaging applications," *Biomed. Opt. Express*, vol. 1, no. 4, p. 1188, 2010.

[99] P. Mohajerani, S. Kellnberger, and V. Ntziachristos, "Fast Fourier backprojection for frequency-domain optoacoustic tomography," *Opt. Lett.*, vol. 39, no. 18, p. 5455, 2014.

[100] P. M. Joseph, "Sampling errors in projection reconstruction MRI.," *Magn. Reson. Med.*, vol. 40, pp. 460–466, 1998.

[101] V. Rasche, D. Holz, and W. Schepper, "Radial turbo spin echo imaging," *Magn. Reson. Med.*, vol. 32, no. 5, pp. 629–638, 1994.

[102] D. C. Peters, F. R. Korosec, T. M. Grist, W. F. Block, J. E. Holden, K. K. Vigen, and C. A. Mistretta, "Undersampled projection reconstruction applied to MR angiography," *Magn. Reson. Med.*, vol. 43, no. 1, pp. 91–101, 2000.